NNT : 2015SACLS180

THÈSE DE DOCTORAT
DE
L'UNIVERSITÉ PARIS-SACLAY
PRÉPARÉE À
L`UNIVERSITE PARIS-SUD ET UNIVERSITA DI PISA

ECOLE DOCTORALE N° 572
Ondes et matières

Spécialité de doctorat : Physique quantique

Par

M. Riccardo Faoro

Few-body interactions in cold Rydberg atoms

Thèse présentée et soutenue à à Orsay (LAC, Salle Balmer), le 3 décembre 2015 :

Composition du Jury :

Pr Browaeys Antoine	Directeur de recherche, CNRS	Président
Pr Adams Charles	Professeur, Durham University	Rapporteur
Pr Gallagher Tom	Professeur, University of Virginia	Rapporteur
Pr Ciampini Donatella	Professeur, Università di Pisa	Examinatrice
Pr Pillet Pierre	Directeur de recherche, CNRS	Directeur de thèse
Pr Fuso Francesco	Professeur, Università di Pisa	Co-directeur de thèse
Pr Arimondo Ennio	Professeur, Università di Pisa	Invité
Dr Cheinet Patrick	Chargé de recherche, CNRS	Invité

Commisione Università di Pisa :

Prof Arimondo Ennio	Professore, Università di Pisa	Presidente
Prof Adams Charles	Professore, Durham University	Esaminatore
Prof Gallagher Tom	Professore, University of Virginia	Esaminatore
Prof Pillet Pierre	Directeur de recherche, CNRS	Relatore
Prof Fuso Francesco	Professore, Università di Pisa	Co-relatore

université PARIS-SACLAY | ÉCOLE DOCTORALE Ondes et Matière (EDOM)

Titre : Interaction à quelques corps entre atomes de Rydberg

Mots clés : gas de Rydberg gelé, FRET à trois corps, interaction dipole-dipole, résonance de Förster, excitation laser hors résonance, repulsion van der Waals

Résumé : L'objectif de cette thèse est l'étude des différents aspects de l'interaction à quelques corps entre des atomes de Rydberg froids. Cette thèse a été réalisée dans le cadre d'une cotutelle entre l'Université Paris-Saclay et l'Université de Pise en travaillant sur deux différents montages expérimentaux sur des atomes de Rydberg froids : respectivement sur le Cs au Laboratoire Aimé Cotton et sur le Rb au département de Physique de l'Université de Pise. Au Laboratoire Aimé Cotton nous avons démontré l'existence des nouvelles interactions à quelques corps dans un gas gelé d'atomes de Rydberg. Ces nouvelles résonances sont la généralisation des résonances de Förster bien connues dans le domaine des atomes de Rydberg. Ces résonances agissent sur les degrés de liberté interne des atomes de Rydberg et ont l'effet d'un transfert résonant d'énergie et de population comme dans le cas des FRET (Fluorescence Resonance Energy Transfer). En analogies avec la résonance de Förster, les résonances FRET à trois corps sont accordées avec un champ électrique externe et peuvent être observées pour différents nombres quantique principaux. Les effets à trois corps sont observés en absence de tout effet à deux corps et sont qualifiés de Borroméens. La présence d'un champ externe peut générer d'autres résonances entre atomes de Rydberg qui sont interdites en absence de champ électrique. Ces résonances, qu'on peut qualifier des résonances quasi-interdites, sont dues à un couplage dipole-dipole de type Förster. Nous avons identifié toutes ces résonances liées au couplage entre les multiplicités de différents n.
Dans le montage expérimental à Pise on a étudié les effets mécaniques d'une répulsion van der Waals entre atomes de Rydberg. Nous avons étudié l'expansion due à l'interaction van der Waals dans une chaîne 1D des atomes de Rydberg de Rb qui ont étés excités avec une excitation laser hors résonance. La comparaison entre les différents désaccords de l'excitation laser montre le rôle central de l'interaction van der Waals.

Title : Few-body interactions in cold Rydberg atoms

Keywords : frozen Rydberg gas, three-body FRET, dipole-dipole interaction, Förster resonance, off-resonant laser excitation, van der Waals repulsion

The aim of this thesis is to investigate different aspects of few-body interactions in cold Rydberg atoms. It has been realized in a co-tutelle program between the University of Paris-Saclay and the University of Pisa working on two different experimental set up: one at Laboratoire Aimé Cotton on cold Cs Rydberg atoms and a second at Physics Department of Pisa on cold Rb Rydberg atoms. In Laboratoire Aimé Cotton we demonstrated the existence of new few-body interactions we observed in a frozen Rydberg gas of Cs atoms. These new resonances are a generalization of already known two-body Förster resonances. They act on the internal degrees of freedom of the Rydberg atoms leading to a resonant energy transfer analogous to the one in FRET (Fluorescence Resonance Energy Transfer). In analogy with Förster resonance, three-body FRETs are tuned with an external electric field and can be observed for different principal quantum number. The three-body interaction appeared in the absence of any two-body ones and for this reasons it has a Borromean character. The presence of this external electric field leads to additional resonances between Rydberg atoms supposedly forbidden. These resonances, we call quasi-forbidden Förster resonances, are due to dipole-dipole interaction as in the case of Förster resonance. We investigated these resonances finding a large number close to the allowed two-body and three-body FRET. A precise study was necessary in order to identify and discriminate these resonances from the allowed ones. In the experiment in Pisa we focus our attention on the mechanical effect of van der Waals repulsion between Rydberg atoms. We studied the spatial expansion due to a van der Waals interaction in a 1D chain of Rb Rydberg atoms excited with an off-resonant laser excitation. The comparison of the excitation reveals the central role of the van der Waals interaction whose strength is equal to the spatial expansion for different detuning of the laser excitation.

Contents

List of Figures

List of Tables

1 Introduction

The pioneering proposition of directly simulating physical phenomena with a quantum system proposed by Richard Feynman [Feynman, 1982] has known a great development in the last years. Many different quantum systems have been proposed for the implementation of a quantum simulation experiment [Buluta and Nori, 2009, Georgescu et al., 2014]: atoms, ions , nuclear and electronic spins, superconducting circuits, photons, etc... In this context experiments with ultracold atoms are considered the most advanced platform for the implementation of quantum simulation experiments [Bloch et al., 2012]. Important results have been obtained in the simulation of many-body Hamiltonians which has lead to the first observation of a Superfluid to Mott insulator transition [Greiner et al., 2002] or the BEC-BCS crossover [Bourdel et al., 2004] or the "fermionization" of a Bose gas, the so-called TonksGirardeau gas [Kinoshita et al., 2004, Paredes et al., 2004]. In most of these experiments the phase transition is obtained by adjusting the interaction between neutral atoms. An external control of the interactions between atoms is thus fundamental for the realization of a quantum simulator. In this frame highly excited atoms, also known as Rydberg atoms, characterized by strongly tunable dipole-dipole or van der Waals interactions, have been proposed for quantum simulation [Weimer et al., 2010]. A recent work [Schauß et al., 2015] has shown the potentiality of Rydberg atoms in realizing a so called "Rydberg crystal" that can be used for probing the quantum phase transition in a quantum magnet.
The strong interaction of the Rydberg atoms not only attract interest for quantum simulation but also for quantum computation [Monroe, 2002]. The dipole blockade effect as well as the Förster resonance have been proposed for the implementation of quantum gates and quantum entanglement experiment [Saffman et al., 2010]. The dipole blockade [Comparat and Pillet, 2010] is a well known phenomenon in Rydberg atoms. It consists in the inhibition of a Rydberg excitation when an already excited Rydberg atom is close enough. The inhibition is related to the strong interaction (dipole-dipole or van der Waals) between the atoms which shifts the Rydberg energy level and makes the laser excitation no more resonant for the excitation of a second Rydberg atom. This phenomenon has been exploited for the implementation of an entangled state between a Rydberg and a ground state atoms [Urban et al., 2009,

Gaëtan et al., 2009, Wilk et al., 2010]. Successively the dipole blockade has been used for the implementation of a C-NOT quantum gate [Isenhower et al., 2010] that represents the first demonstration of quantum gates and entanglement between a single pair of trapped neutral atoms.
A second aspect of Rydberg atoms that seems to be promising in quantum computation is Förster resonance [Mourachko et al., 2004, Anderson et al., 1998]. Förster resonance is a two-body process due to a resonant dipole-dipole coupling between two two-atom states [Walker and Saffman, 2005]. The name of "Förster resonance" has been given by Thad Walker and Mark Saffman [Walker and Saffman, 2005] in analogy with FRET (Fluorescence Resonant Energy Transfer)[Förster, 1948, Perrin, 1932]. The significant analogies between Förster resonance in Rydberg atoms and FRET resonance in biology, which seems to be the leading process in light-harvesting [Oar et al., 2006, Collini et al., 2010, Ajayaghosh et al., 2007], has inspired interesting experiment focused on the simulation of quantum energy transport induced by two-body FRET in a frozen Rydberg gas [Günter et al., 2013] and in a chain of three Rydberg atoms [Barredo et al., 2015].
One of the more interesting aspects of Förster resonance is the possibility to tune the dipole-dipole interaction which couples the two two-atom state with an external parameter: an external electric field [Safinya et al., 1981]. Förster resonance has been observed in different atomic species (Na, K, Rb, Cs). In cold Cs atoms a series of Stark tuned Förster resonance described by the transfer equation:

$$2 \times np_{3/2} \leftrightarrow (n+1)s + ns$$

have been observed for n ranging between 25 and 41 [Viteau et al., 2008]. The Stark effect due to an external electric field shifts the Rydberg states $np_{3/2}$, ns and $(n+1)s$ in different ways. It is thus possible to tune the energy of the np state to the average energy of ns and $(n+1)s$. The resonant dipole-dipole coupling removes the degeneracy of the two-atom states $|np_{3/2}, np_{3/2}\rangle$ and $1/\sqrt{2}(|(n+1)s, ns\rangle + |ns, (n+1)s\rangle)$ and the new eigenstates of the system are a superposition of these two latter states.
The tunability of a Förster resonance with a relatively small static electric field seems thus to be a promising tool for the implementation of two-body quantum gates [Ryabtsev et al., 2010, Ravets et al., 2014]. In this direction the generalization of a two-body FRET to a n-body process can open the possibility for the implementation of multi qu-bits gates. In this sense a pioneering work on a direct observation of a Stark-tuned four-body FRET [Gurian et al., 2012] shows that is possible to realize a FRET resonance with more than two atoms. In this work Gurian et al. observed in a cold Cs Rydberg gas a resonant energy transfer due to a four-body interaction

described by the transfer equation:

$$4 \times 23p_{3/2} \rightarrow 2 \times 23s + 23p_{1/2} + 23d_{5/2}$$

However this four-body FRET is not a general process because it appear only for this particular Rydberg state $23p_{3/2}$. It thus seems hard to apply it for the implementation of multi qu-bits quantum gate. The implementation of a four-body quantum gate thus requires a more general process.
The initial purpose of this thesis was the observation of two general Stark-tuned four-body resonances described by the following equations:

$$3 \times |np_{3/2}, |m_j| = 1/2\rangle + |np_{3/2}, |m_j| = 3/2\rangle \leftrightarrow 2 \times |ns_{1/2}\rangle + 2 \times |(n+1)s_{1/2}\rangle$$
$$|np_{3/2}, |m_j| = 3/2\rangle + 3 \times |np_{3/2}, |m_j| = 1/2\rangle \leftrightarrow 2 \times |ns_{1/2}\rangle + 2 \times |(n+1)s_{1/2}\rangle$$

for a principal quantum number n ranging between 28 and 35 in cold Cs Rydberg atoms. These four-body resonances were predicted in the proximity of a Förster resonance. However the first preliminary measurements we realized revealed the presence of a large number of quasi forbidden Förster resonances. Quasi-forbidden Förster resonances have been observed in Na and K [Kachru et al., 1983, Renn et al., 1994]. These resonances exist in presence of an external static electric field leading to some coupling between Rydberg states in the transition dipole matrix. In the presence of an external electric field the eigenstates of the dipole-dipole Hamiltonian are no longer a pure eigenstates of the system. Then the dipole-dipole selection rules apply only partially, allowing the presence of several quasi forbidden two-body Förster resonances in addition to the dipole allowed two-body Förster resonance once a dipole allowed Förster resonance exists in a specific atom. The presence of these quasi-forbidden resonances makes difficult the observation of the four-body interaction because they occur at the same electric field at which we would expect the four-body resonances.
In the characterization of these quasi-forbidden resonances we discover a new three-body process in the proximity to a Förster resonance and strictly related to it. The three-body FRETs we discover it is even more general than the one proposed four a four-body interaction. They are described by the following transfer equations:

$$3 \times |np_{3/2}, |m_j| = 1/2\rangle \leftrightarrow |ns_{1/2}\rangle + |(n+1)s_{1/2}\rangle + |np_{3/2}, |m_j| = 3/2\rangle$$
$$3 \times |np_{3/2}, |m_j| = 3/2\rangle \leftrightarrow |ns_{1/2}\rangle + |(n+1)s_{1/2}\rangle + |np_{3/2}, |m_j| = 1/2\rangle$$

They appeared in the absence of any two-body ones and for this reasons it has a Borromean character in analogies with the proposed Borromean interaction in Rydberg atoms for the realization of three-atom bound state [Kiffner et al., 2013].

The study of the two-body and three-body FRET I have participated in Laboratoire Aimé Cotton was focused more on the dipole-dipole interaction effect on the internal degree of freedom of the Rydberg atoms. We start from the hypothesis of a "frozen Rydberg gas" [Mourachko et al., 1998] where the mechanical effect due to the Rydberg-Rydberg interaction can be neglected. However for longer evolution times or even an out of resonance Rydberg excitation [Amthor et al., 2007] the mechanical effect of Rydberg-atom Rydberg-atom interaction becomes evident. The mechanical effect of a van der Waals repulsion between two Rydberg atoms excited with an off-resonant Rydberg excitation has been exploited for measuring the C_6 coefficient [Béguin et al., 2013, Thaicharoen et al., 2015]. Moreover the expansion of dense Rydberg gas has been observed with a microwave spectroscopy of a dense Rydberg gas revealing the potentiality of an off-resonant excitation in the study of mechanical effect of a van der Waals interaction [Teixeira et al., 2015].

In chapter 2 we first introduce the scaling, characteristic for the Rydberg atoms, of the physical quantities (atomic radius, radiative lifetime, polarizability, etc...) as a power of the principal quantum number n. We then briefly describe the Stark effect due to an external electric field which has a crucial importance in the study of FRET resonance. We finally conclude by describing the interaction (dipole-dipole or van der Waals) between two Rydberg atoms.
In chapter 3 we describe the experimental set up in Laboratoiré Aimé Cotton we use for the excitation of the cloud of cold Cs Rydberg atoms that then interact via the tuned dipole-dipole interaction. We describe in detail the three-photon excitation technique we use to excite the $|np_{3/2}, |m_j| = 1/2\rangle$ and $|np_{3/2}, |m_j| = 3/2\rangle$ Rydberg states. We describe the time-of-flight detection technique we use for the observation of a transfer of population from the initial $np_{3/2}$ to the resonant ones ns and $(n+1)s$. A paragraph is devoted to explain the analysis technique that has been developed at Laboratoire Aimé Cotton for extracting the correct number of atoms in different Rydberg states involved in the interaction.
In chapter 4 we describe the experimental study we have done of all the possible quasi-forbidden resonances in the proximity of a two-body FRET for Cs Rydberg atoms with a principal quantum number ranging between $n = 28 - 35$. This range was first choose for the observation of original project on the four-body FRET but once we realized it was not possible we decided to systematically study all the quasi-forbidden resonances. These additional resonances could be of interest to increase the number of addressable resonances for possible quantum gates, for the creation of molecules from Rydberg atoms or for all applications based on few-body interactions. In addition, these resonances could introduce addressable resonances whenever no dipole allowed

resonance exists, for instance in Cs for $n > 42$ [Viteau et al., 2008] or when starting from an initial ns state. The classification of quasi-forbidden resonances is also necessary when we want to study dipole-quadrupole interactions as the one observed in [Deiglmayr et al., 2014] in the proximity of a Förster resonance for Cs atoms because they can couple the same Rydberg states.
In chapter 5 we describe the main result achieved during my PhD: the characterization of a three-body Borromean interaction. We will better explain the analogy with the trimer Efimov state [Kraemer et al., 2006, Pollack et al., 2009] and predicted the Borromean interaction in Rydberg atoms [Kiffner et al., 2013]. We will also see that this kind of interaction can be generalized to a N-body process due to a so called Brunnian interaction [Yamashita et al., 2010]. Three-body Borromean FRET resonances seem also to be a promising tool for the implementation of entanglement experiment and of a three-body quantum gate. In this chapter we finally propose some possible applications of a three-body interaction in quantum information.
In the final chapter I describe the work I have participated in the BEC Group of Pisa under the supervision of Prof. Ennio Arimondo, Dr. Oliver Morsch and Dr. Donatella Ciampini. I have participated to the study of a mechanical effect due to a van der Waals repulsion explosion of a 1 D chain of Rb Rydberg atoms excited with an off-resonant Rydberg excitation. I will first describe the experimental set up in Pisa used for the excitation of a 1 D chain of Rydberg atoms with the so called "seed" technique. This technique, that has been developed in Pisa, allows the creation of cluster of Rydberg atoms with an off-resonant excitation detuned up to 80 MHz. For the observation of a spatial expansion we have realized a calibration of the ion arrival time on the channeltron detector in order to extrapolate the amount of the spatial expansion of the cluster of Rydberg atoms from a time-of-flight signal. We finally present the experimental results on the observation of van der Waals interaction in Rydberg cluster that demonstrate the intrinsic mechanical instability of off-resonantly excited Rydberg aggregates.

2 Rydberg atoms: general properties and Rydberg-Rydberg interactions

2.1 General Properties

2.1.1 Quantum defect theory

Rydberg atoms are atoms in a highly excited state [Gallagher, 1994]. They are characterized by exaggerated properties (large atomic radius, huge dipole moment, etc) scaling with powers of the principal quantum number n. The easiest example of a Rydberg state is a highly excited state of the H atom. It is well known that for a H atom the Schrödinger equation can be analytically solved [Konishi and Paffuti, 2009, Bethe and Salpeter, 1957] leading to the well known Balmer's formula describing the energy levels:

$$E_n = -\frac{R_y}{n^2}. \tag{2.1}$$

where R_y is the Rydberg constant defined as:

$$R_y = \frac{m_e e^4}{2(4\pi\epsilon_0\hbar)^2} = \frac{1}{2} m_e \alpha^2 c^2 \tag{2.2}$$

equal to 13.60569253(30) eV calculated from the experimental value of R_∞ defined as $R_y = hcR_\infty$ [Pohl et al., 2010]. When we write equation 2.1 we are neglecting the small correction due to the finite proton mass m_p equal to $1/(1 + m_e/m_p)$. This approximation corresponds to consider the ionic core, in this case composed by a proton, with an infinity mass compared to the electron. If we instead consider the finite mass of the ionic core we can define a "corrected" Rydberg constant:

$$R_M = \frac{R_\infty}{1 + m_e/M}. \tag{2.3}$$

where M is the mass of the ionic core. The "corrected" Rydberg constant is a first correction of the general Balmer formula of equation 2.1 considering the mass of the

ionic core.
However when we want to calculate the Rydberg levels of an alkaline metal (Li, Na, K ...)the mass of the ionic core is not the only important modification to take into account. We have to take into account the effects due to interaction of the ionic core with the valence electron i.e. the Rydberg electron. In a semiclassical interpretation when the Rydberg electron is far enough from the ionic core it is only sensitive to a net charge ~ 1 because the remaining charges of the nucleus are perfectly screened by the inner shell electrons. This situation corresponds to Rydberg state with high angular momentum l that are characterized by circular Bohr orbits. In this case the electron wavefunction is not perturbed by the core and it is similar to the Rydberg function obtained for H.
On the other hand when the Rydberg electron comes close enough to the ionic core the charge distribution due to the finite size of the core does play a role. The inner electrons do not totally screen the nucleus charge so the Rydberg electron feels a net charge bigger than one. It can both polarize and penetrate the ionic core. The Rydberg electron wave-function is thus perturbed by the interaction with the ionic core. The Rydberg electron is more bounded to the ionic core with a consequently lowering of the of the corresponding Rydberg levels. This is the case of Rydberg state with low angular momentum that has an elliptical orbit which penetrates the ionic core. The binding effect of the ionic core can be taken into account introducing a parameter called the quantum defect δ_{nlj}. We can thus introduce the Rydberg formula's describing the energy scaling of Rydberg levels:

$$E_{n\ell} = -\frac{Z^2 R_y}{(n-\delta_{nlj})^2}. \tag{2.4}$$

where Z is the ionic core charge. In the case of alkaline metal Z=1. The quantum defect is an empirical parameter characteristic of each elements. It depends principally on the angular momentum l and only slightly on the total angular momentum j and the principal quantum number n. The n dependence can be expressed by the Ritz formula n [Drake and Swainson, 1991]:

$$\delta_{nlj} = \delta_0(lj) + \frac{\delta_2(lj)}{(n-\delta_0(lj))^2} + \frac{\delta_4(lj)}{(n-\delta_0(lj))^4} + ... \tag{2.5}$$

but only δ_0 and δ_2 are measured experimentally then used as a parameter fit for 2.5. For Caesium [Goy et al., 1982, Weber and Sansonetti, 1987] and Rubidium [Farley et al., 1977, Li et al., 2003, Mack et al., 2011] atoms an accurate measure of the Rydberg levels and the consequent evaluation of the quantum defect has been

Series	δ_0	δ_2
ns	4.049325	0.2462
$np_{1/2}$	3.591556	0.3714
$np_{3/2}$	3.559058	0.3740
$nd_{3/2}$	2.475365	0.5554
$nd_{5/2}$	2.466210	0.0670
$nf_{5/2}$	0.033392	-0.191
$nf_{7/2}$	0.033537	-0.191

Table 2.1: List of quantum defect δ_0 and δ_2 for different Rydberg states of Cs. This values has been taken from [Goy et al., 1982].

realized.

2.1.2 Scaling Properties

Atomic radius

The most interesting aspect of Rydberg atoms stems on their size. Some simple consideration can lead to estimate the expectation values of r^σ. Since the Rydberg electron is supposed to spend most of its time near its outer classical turning point $r_o = 2n^2$, a good estimate for the expectation value of r^σ with $\sigma > 0$, is in atomic units:

$$\langle n, l, j | r^\sigma | n, l, j \rangle \sim n^{2\sigma} \tag{2.6}$$

where we introduce the spherical basis $|n, l, j\rangle$. We can immediately remark that for Rydberg levels with $n = 30 - 100$ we have an atomic radius $10^3 - 10^4$ times bigger than the ones of a ground state atom, that corresponds for alkaline atoms to an atomic radius of $0.1 - 1$ μm. In fig.2.1 we report a schematic comparison of the atomic radius of ground state atom of H with a Rydberg state of $n = 10$. We can see that the atomic radius dramatically increase as we increase the principal quantum number n.

Energy separation

Another easy consideration on the scaling can be done looking at equation 2.4. We can immediately observe that the difference in energy between two adjacent Rydberg

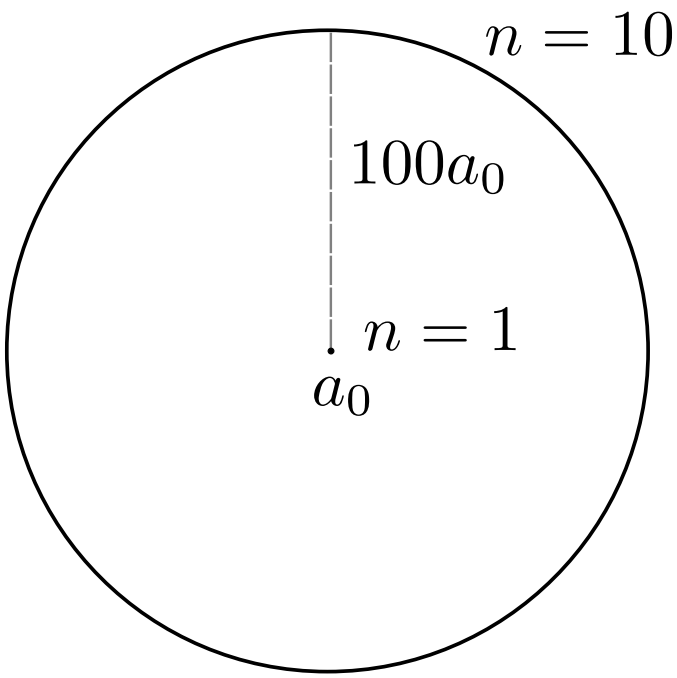

Figure 2.1: Comparison of Rydberg radius for two different Rydberg states of H atoms. Respectively for $n = 1$ and $n = 10$. Figure taken from [Gallagher, 1994]

levels n and $n + 1$ scales as:

$$\Delta E \propto \frac{1}{n^3} \tag{2.7}$$

As n increase the Rydberg levels get closer and closer as shown in fig.2.2.

Dipole moment

We can now derive, using a combination of radial matrix elements and energy separation, the n scaling of many properties of Rydberg atoms. A direct one is the scaling of the electric dipole matrix element between neighbouring levels that is proportional to the atomic radius. We thus obtain:

$$\langle n, l, j|er|n, l', j'\rangle \propto n^2 \tag{2.8}$$

As previously discussed for the atomic radius we can see that Rydberg atoms are characterized by strong dipole moment transition several orders bigger than the ones between lower levels. Consequently, as we will see in the next section, dipole-dipole

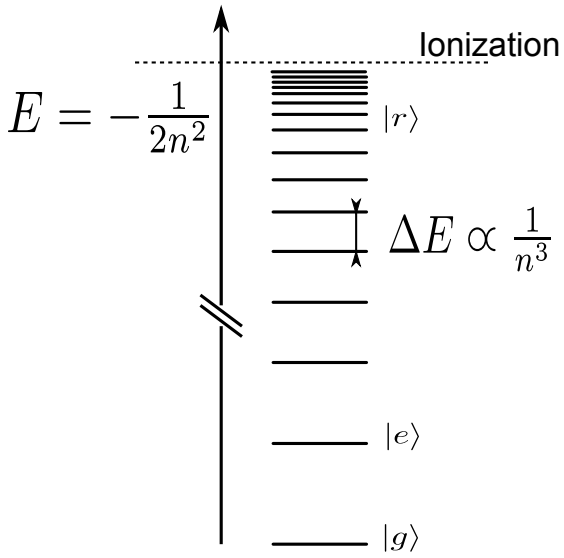

Figure 2.2: Scheme of a Rydberg serie for an H atom.

interactions as well as van der Waals interactions are strongly enhanced.
An other interesting quantity is the polarizability which is proportional to the sum of the electric dipole matrix elements squared divided by energy denominators, yielding polarizabilities $\alpha \propto n^7$. Since the induced dipole moment $p = \alpha E_{ext}$ where E_{ext} is an external electric field, it is possible to induce a non negligible dipole moment with small electric field [Hogan and Merkt, 2008].

Radiative lifetime

Rydberg atoms are characterized by long radiative lifetimes. One way to calculate the scaling of the radiative lifetime as a power of n is by calculating the Einstein coefficient. We know that the Einstein A coefficient, $A_{n'l'j',nlj}$, defines the spontaneous decay rate of the $|nlj\rangle$ state to the lower state $|n'l'j'\rangle$:

$$A_{n'l'j',nlj} = \frac{4e^2\omega^3_{nlj,n'l'j'}}{3\hbar c^3}\frac{max(l,l')}{2l+1}|\langle n,l,j|er|n,l',j'\rangle|^2. \tag{2.9}$$

The radiative lifetime, τ_{nlj} of the $|nlj\rangle$ state is the inverse of the total radiative decay rate which is obtained summing the Einstein coefficient A for all the lower lying $|n'l'j'\rangle$

states:

$$\tau_{nlj} = \Big(\sum_{n'l'j'} A_{n'l'j',nlj} \Big)^{-1} \tag{2.10}$$

This series is dominated by the highest frequency term that corresponds to the transition from a $|n, l\rangle$ state to the lowest lying $l - 1$ state (except for s state which has the highest frequency transition with a p state). For high values of n, the transition frequency approaches a constant so the Einstein coefficient depends only on the radial matrix elements. Only the part of the Rydberg state wavefunction which spatially overlap the wavefunction of the lowest lying state contributes to the matrix elements of equation 2.9. This term exhibits an n^{-3} scaling as stated in [Gallagher, 1994]. We finally obtain:

$$\tau_{nlj} \propto n^3 \tag{2.11}$$

Radiative decay is not the only source of de-excitation of Rydberg atoms. Black body radiation can induce dipole transitions between neighbouring Rydberg level [Gallagher and Cooke, 1979]. The black body photons can produce a stimulated emission or be absorbed leading to the excitation of a higher lying Rydberg level. This redistribution of the population finally increase the total radiative decay rate that can be written in the following way:

$$\Gamma_{tot} = \Gamma_R + \Gamma_{BBR} \tag{2.12}$$

where we have introduced $\Gamma_R = \tau_{nlj}^{-1}$ and Γ_{BBR} is the radiative decay rate due to black body radiation which is the sum of all the black body transition rates plus the black body photo-ionization rate [Fano and Rau, 1986]. That finally leads to the following expression:

$$\Gamma_{BBR} = \frac{4\alpha^3 k_B T}{3n^2} \tag{2.13}$$

where α is the fine structure constant, k_B the Boltzmann constant and T the temperature. Comparing equations (2.13) and (2.11) we can see that at high n the black body radiation rate exceeds the spontaneous emission rate leading to a diffusion to other energetically nearby Rydberg states characteristic of the black-body de-excitation. As we can see from equation 2.13 the decay rate due to the black body radiation linearly increase as the temperature. Working with cold atoms in a thermal bath at cryostat temperature [Teixeira et al., 2015] can strongly reduce the de-excitation due to black-body radiation.

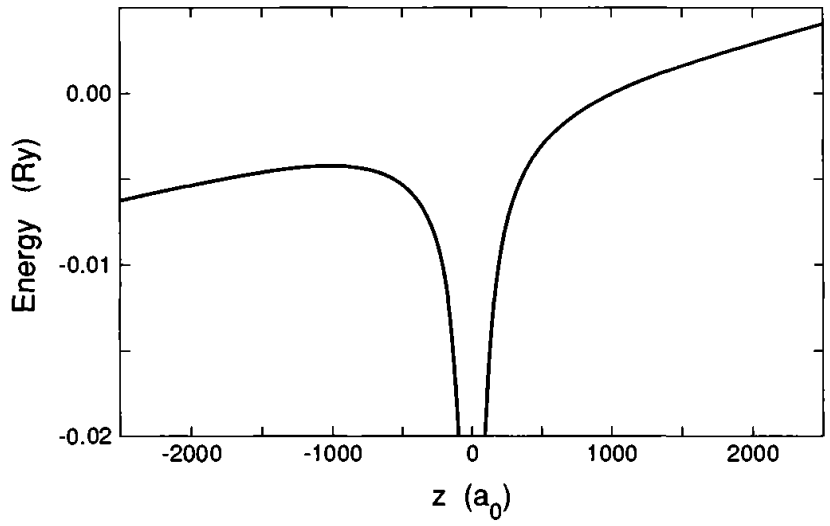

Figure 2.3: Combined Coulomb-Stark potential along the z-axis for a field of 5.14 kV/cm along the z direction. This figure has been taken from [Gallagher, 1994].

Field ionization

We can easily deduce from the Balmer's formula of equation 2.1 the scaling of the binding energy $B \propto n^{-2}$. We immediately deduce that as we increase the principal quantum number n we need less and less energy to ionize the Rydberg state. By applying a relative small electric field it thus is possible to ionize Rydberg atoms.
In order to calculate the so called classical ionization limit we consider the Rydberg electron subjected to a combination of a Coulomb potential and a uniform electric field along z-direction. The potential has the following form:

$$V = -\frac{1}{4\pi\epsilon_0 r} + Fz. \tag{2.14}$$

In Fig. 2.3 we plot V along the z-direction. The potential presents a local maximum at $z_0 = -1000\ a_0$, that corresponds to a saddle point in three dimension. This local maximum represents the ionization limit, above this limit the electrons are no longer bounded to ionic core. At the saddle point the potential is $V(z_0) = -2\sqrt{4\pi\epsilon_0 F_I}$. If we now equate this value of the potential to the Balmer' formula $-R_y/n^2$ we obtain:

$$F_I = \frac{4\pi\epsilon_0 R_y^2}{4n^4} \tag{2.15}$$

Quantities	Scaling	40 p Cs
Binding energy	n^{-2}	82.638 cm^{-1}
Energy between adjacent n state	n^{-3}	4.5 cm^{-1}
Atomic Radius	n^2	127 nm
Geometric cross section	n^4	10^2 Å^2
Electric dipole moment	n^2	-971 Debye
Radiative Lifetime (low l)	n^3	47μs
Polarizability	n^7	10 MHz cm^2/V^2

Table 2.2: Scaling of the physics quantities in Rydberg atoms and numerical values for 40 $p_{3/2}$ Cs atom [Viteau, 2008].

Eq. 2.15 tells us that each Rydberg state have a characteristic ionization limit that decrease as n^4 for increasing n. This correspondence is the basis of the so called selective field ionization technique, which is one of the most used detection technique for Rydberg atoms. It consists in applying a external electric field that increase in time in order to ionize different Rydberg levels at different times. We will discuss more in detail this technique in the next chapter. In table 2.2 we report a brief resume of the scaling of physical quantities in Rydberg atoms.

2.1.3 Stark effect

H atoms

The strong polarizability of Rydberg atoms makes them strongly sensitive to external electric fields. For that reason Rydberg atoms undergoes strong Stark effect. To compute the Stark effect, one has to consider the energy of each state which is different for alkaline atoms from H atoms. Let us first consider the H atom. We begin by considering the behaviour of the H atom in a static electric field F, ignoring the spin of the electron. The Hamiltonian describing the system in atomic units ($e = h = m_e = 1$) is:

$$\hat{H}_{tot} = -\frac{\nabla}{2} - \frac{1}{r} - Fz \tag{2.16}$$

In Fig. 2.4 we report the Stark map of an H atom for different principal quantum numbers $n = 8-14$ [Luc-Koenig and Bachelier, 1980]. The static electric field removes the degeneracy of the Rydberg n^{th} multiplicity. At first order H atom presents a linear Stark effect. This is mostly due to the characteristic selection rule of Stark effect: $\Delta l = \pm 1$ and $\Delta m = 0$ where only the matrix elements $\langle n, l, m|Fz|n', l \pm 1, m\rangle$ are

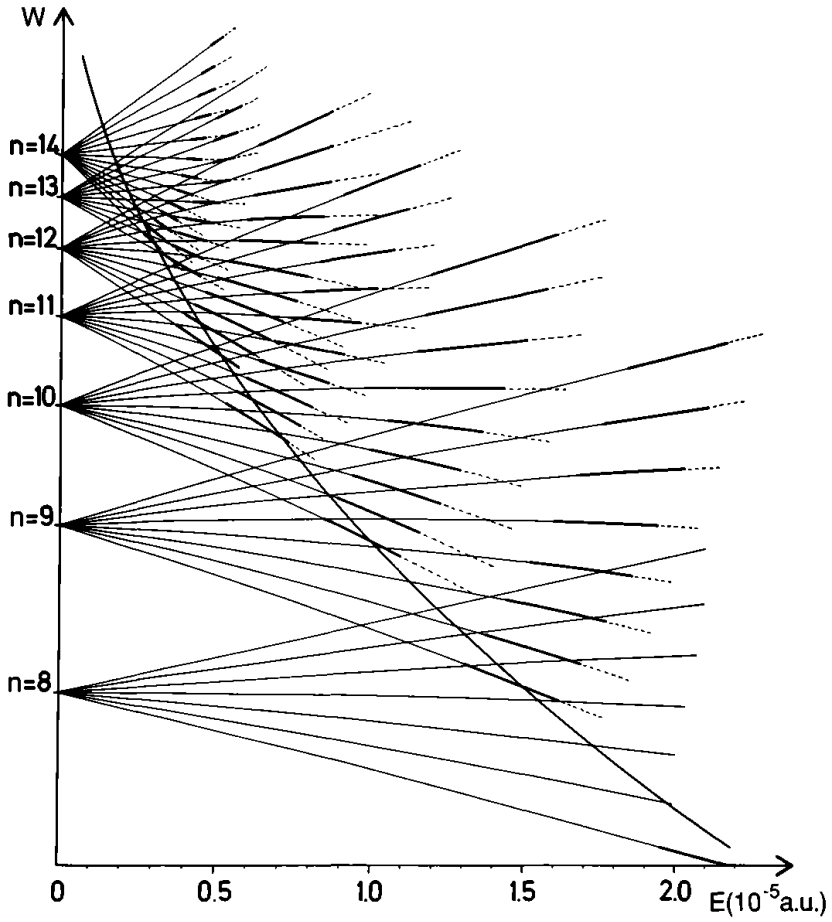

Figure 2.4: Stark structure of the $|m| = 1$ states of the H atom for n varies from 8 to 14. The dashed lines represent the field ionized state. The classical ionization limit described by $E = -2\sqrt{F}$ is also plotted. This figure has been taken from [Luc-Koenig and Bachelier, 1980]

different from zero. Since F is a static uniform field we can bring it out from the integral $\langle n, l, m|Fz|n', l \pm 1, m\rangle = \langle n, l, m|z|n', l \pm 1, m\rangle F$ and, using the properties of spherical harmonics [Bethe and Salpeter, 1957] we obtain that at first approximation the Stark field is proportional to F. Since the electric field couples only states with the same m, it is a good quantum number and the Stark map of each m are independent of the others.
For a more precise calculation of the Stark effect a more formal approach is required. The more common way is to solve equation 2.16 in parabolic coordinate because in this system of coordinates the equation remains separable [Bethe and Salpeter, 1957]. The external electric field is treated in a perturbative way. Here we report the second order solution of eq.2.16 in parabolic coordinates:

$$E_{n,n_1,n_2,m} = -\frac{1}{2n^2} + \frac{3Fn}{2}(n_1 - n_2) - \frac{F^2}{16}n^4[17n^2 - 3(n_1 - n_2)^2 - 9m^2 + 19] \quad (2.17)$$

where we have introduced the parabolic quantum numbers n_1 and n_2 satisfying $n = n_1 + n_2 + |m| + 1$. These new quantum numbers allow us to introduce the so called " red" and "blue" states. "Red states" are characterized by $(n_1 - n_2) < 0$ and they present a negative shift of the energy level while "blue states" have a positive shift i.e. $(n_1 - n_2) > 0$. As we can see from 2.4 blue states of a lower manifold n cross the red states of an upper manifold.
In paragraph 2.1.2 when we have calculated the classical ionization limit we have ignored the Stark shift but Cooke et al. [Cooke and Gallagher, 1978] has shown with a simple classical model the variation of field-ionization thresholds due to the m values. For the case of $m = 0$ the classical ionization field described by equation 2.15 is still valid but for a Rydberg state with $m \neq 0$ there is a centrifugal barrier proportional to $m^2/(x^2 + y^2)$ which raises the threshold field. In Fig. 2.4 the dashed line represent the ionized states. We can see that blue state as a higher ionization limit than the red one. The physical explanation of this behaviour is related to the spatial distribution of the Rydberg wavefunction. For the blue states the Rydberg electron is located on the side of the atom away from the saddle point, that corresponds to the positive range of z in Fig. 2.3. While for red states the Rydberg electron is located on the same side of the saddle point, that corresponds to the negative range of z in Fig. 2.3. For that reason the red states of the same manifold are easily ionized than the blue states.

Alkaline atoms

The Stark effect in alkaline atoms presents important differences compared to H case mostly due to the presence of ionic core of finite size. The Hamiltonian for an alkaline

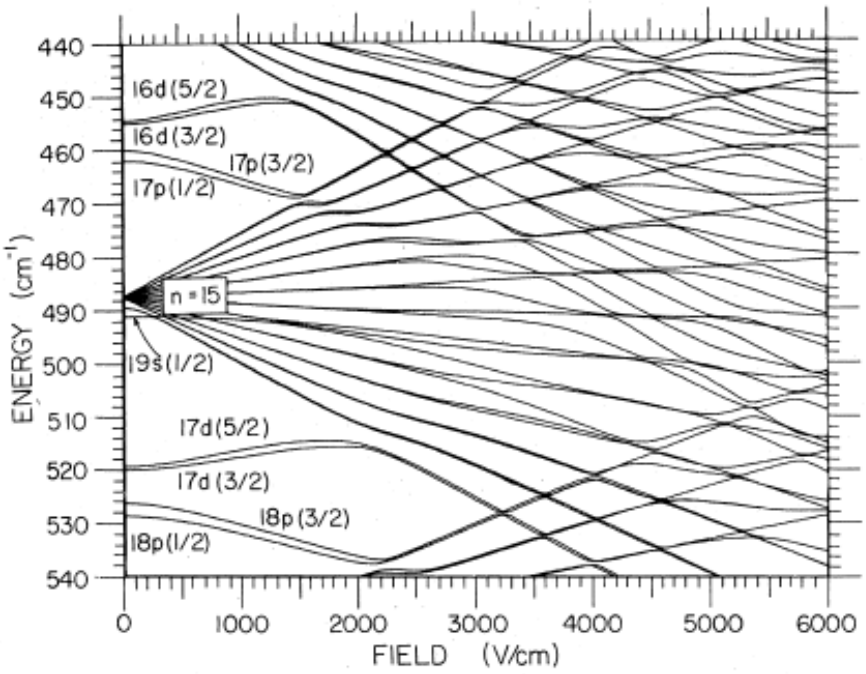

Figure 2.5: Stark map for a Cs atom for $|m_j| = 1/2$ around the $n = 15$ manifold. This figure has been taken from [Zimmerman et al., 1979]

can be written in the following way:

$$\hat{H}_{tot} = -\frac{\nabla}{2} - V_{eff}(r) - Fz \tag{2.18}$$

where compared to equation 2.16 we have replaced the Coulomb potential with $V_{eff}(r)$ which takes into account the ionic core potential. $V_{eff}(r)$ is not precisely known: far from the ionic core it can be well approximated with a Coulomb potential $-1/r$ but near the core it deviates from this latter. The Hamiltonian of equation 2.18 is no more separable in parabolic coordinates as in the case of H and numerical solutions are required. In [Zimmerman et al., 1979] Zimmerman et al. propose a numerical solution using spherical coordinates. The matrix element of the Stark interaction can be written:

$$\langle n, l, m|Fz|n', l', m'\rangle = \delta_{mm'}\delta_{l,l'=l\pm1}F\langle n, l, m|\cos(\theta)|n', l', m'\rangle\langle n, l, m|r|n', l', m'\rangle \tag{2.19}$$

The first integral of the right-hand side of eq. (2.19) can be easily calculated using the properties of spherical harmonics while the radial matrix element requires a numerical solution that can be done with a Numerov method [Numerov, 1924].
Since n_1 and n_2 are no longer good quantum numbers, blue and red state are no longer eigenstates of the system. They slightly overlap at the core and that overlap determines the coupling which is responsible of the avoided crossing. In Fig.(2.5) we report a Stark map calculated in [Zimmerman et al., 1979] for a Cs atom with $|m_j| = 1/2$. We can see the several avoided crossings when the red and blue states of different manifolds superpose. The coupling between red and blue state is also responsible for a second kind of ionization analogous to a phenomenon of auto-ionization [Littman et al., 1978]. It consists in the coupling of a blue states, which would be stable in the case of H, with degenerate unbounded red state. This coupling implies that, unlike in H atoms, blue states of small $|m|$ ionize at the classical ionisation limit. This is not the only way that an alkaline atom can be field ionized. Alkaline atoms can be field ionized with the same mechanism described for H, when the Rydberg electron surmount the potential barrier at the saddle point.

2.2 Rydberg-atom Rydberg-atom interaction

2.2.1 Dipole-dipole interaction: Classical interpretation

A good starting point for describing the interaction between two Rydberg atoms is to consider separately the ionic core and the Rydberg electron in analogy with a H atom. The Rydberg electron is bounded to the ionic core by a Coulomb potential $\sim$ -1/r, where r is the electron distance to the core. When we write the interaction between two Rydberg atoms separated by a distance $\vec{R} = R\vec{n}$ we have to consider four terms that respectively corresponds to the electrostatic repulsion between the two ionic core, the electrostatic attraction between one ionic core and the Rydberg electron of the other atoms and finally the repulsion between the two Rydberg electron. We obtain the following interaction term:

$$H = \frac{1}{4\pi\epsilon_0}\Big[\frac{e^2}{R} - \frac{e^2}{r_{A2}} - \frac{e^2}{r_{B1}} + \frac{e^2}{r_{12}}\Big]. \tag{2.20}$$

where the distances $R,\ r_{A2},\ r_{B1}$ and r_{12} refers to the ones of Fig. 2.6 where a sketch of the interaction is presented. A and B represent the two ionic core while 1 and 2 are the respective Rydberg electrons. With simple geometrical consideration and using

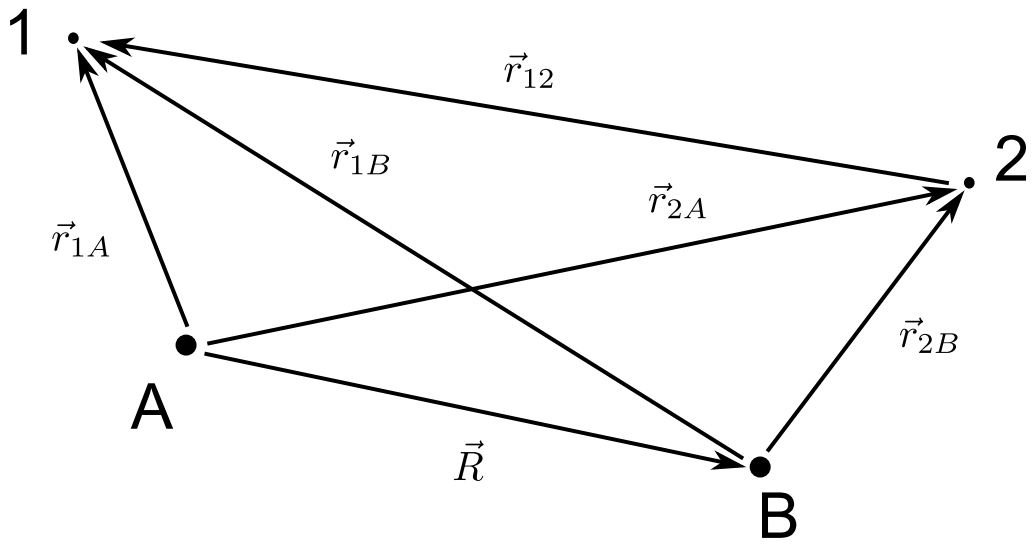

Figure 2.6: Two Rydberg atoms scheme. A and B represents respectively the ionic cores of the two atoms while 1 and 2 are the respective Rydberg electron.

the expansion for $R \gg r$:

$$\frac{1}{||\vec{R}+\vec{r}||} = \frac{1}{R}\left(1 - \frac{\vec{n}\cdot\vec{r}}{R} + \frac{3(\vec{n}\cdot\vec{r})^2 - r^2}{2R^2} + \cdots\right) \tag{2.21}$$

we obtain that the first non vanishing term, the so called dipole dipole interaction, has the following form:

$$H_{dd} = \frac{e^2}{4\pi\epsilon_0 R^3}\big(\vec{r}_{A1}\cdot\vec{r}_{B2} - 3(\vec{r}_{A1}\cdot\vec{n})(\vec{r}_{B2}\cdot\vec{n})\big). \tag{2.22}$$

When we consider the interaction between Rydberg atoms this term plays a predominant role, but occasionally quadrupole-quadrupole interactions have been found to be relevant as in the case of [Stanojevic et al., 2008] where in an ultracold Rydberg gas of Rb atoms the excitation of a $(n-1)d + ns$ two-body state has been theoretically predicted and experimentally observed. In this experiment the Rydberg atoms are directly excited from the ground level $5s$ to the Rydberg state with a one-photon excitation. In one-photon transitions from the $5s$ ground state, dipole transitions to nd and ns states are not allowed while for quadrupole-quadrupole interaction these transitions are allowed.

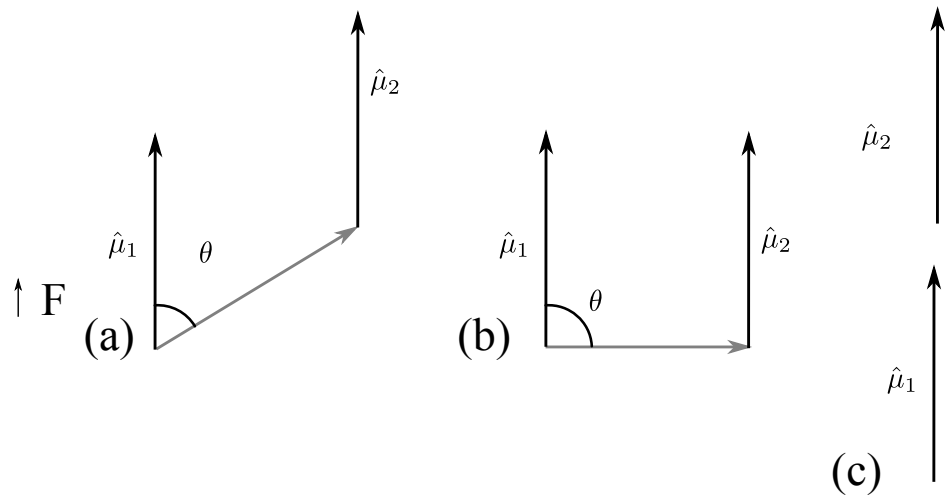

Figure 2.7: Sketch of three possible configurations for a dipole-dipole interaction between two permanent dipole momenta aligned along an external electric field $\vec{F}$. (a) Case for a general angle θ. (b) Side-by-side configuration corresponding to the maximum repulsive interaction. (c) head-to-tail configuration for a maximum attractive interaction.

Dipole-dipole interaction: permanent dipole

The term we have obtained in eq. 2.22 find an analogy with the case of an interaction between two permanent electric dipoles. We know from classical electrodynamics [Jackson, 1962] that an electric permanent dipole $\vec{\mu}$ generates an electric field at a distance $R\vec{n}$:

$$\vec{E} = \frac{1}{4\pi\epsilon_0 R^3}\big(3(\vec{n}\cdot\vec{\mu})\vec{n} - \vec{\mu}\big). \tag{2.23}$$

If we now consider the second permanent electric dipole $\vec{\mu}_2$ at a distance $R\vec{n}$ we obtain that the total energy of the system is:

$$E_{dd} = -\vec{E}_1\cdot\vec{\mu}_2 = -\vec{E}_2\cdot\vec{\mu}_1 = \frac{\vec{\mu}_1\cdot\vec{\mu}_2 - 3(\vec{\mu}_1\cdot\vec{n})(\vec{\mu}_2\cdot\vec{n})}{4\pi\epsilon_0 R^3} \tag{2.24}$$

where $\vec{\mu}_1 = e\vec{r}_{A1}$ and $\vec{\mu}_2 = e\vec{r}_{B2}$. In presence of an external electric field $\vec{F}$, stronger than the sum of the fields generate by the dipoles, those latter are aligned along the direction of $\vec{F}$. We thus obtain for the energy the following dependence on the angle θ defined as $\cos\theta = \vec{n}\cdot\vec{F}/F$:

$$E_{dd} = \frac{\mu_1\mu_2}{4\pi\epsilon_0 R^3}(1 - 3\cos^2\theta). \tag{2.25}$$

In Fig.2.7 (a) we report a scheme of the dipole-dipole interaction between two permanent dipole momenta. We immediately see that the dipole-dipole interaction can change from repulsive to attractive depending on the orientation of the dipole. We have in fact a maximum repulsive interaction for $\theta = \pi/2$: that corresponds to the side-by-side configuration as sketched in Fig. 2.7(b). For $\theta = 0$ we have the maximum attractive interaction that corresponds to the head-to-tail configuration which we report in the scheme of Fig. 2.7(c). We finally observe that for a special angle $\theta = 55^\circ\ 47'$ the interaction drop to zero.

Dipole-dipole interaction: oscillating dipole

Before introducing the quantum interpretation of dipole-dipole interaction a useful example is to study the case of an oscillating dipole. We consider the dipole made by two charges $+e$ and $-e$, one at rest and the other oscillating. If d is the distance between the charges we can write the oscillating dipole momentum $\vec{\mu}(t) = \vec{\mu}\exp(-i\omega t)$ where $\vec{\mu} = e\vec{d}$. The formalism used for the calculation of the electric field for an oscillating dipole is the one of the retarded potential [Feynman and Leighton, 1964]. The electromagnetic field irradiated by an oscillating dipole $\vec{\mu}_1(t) = \vec{\mu}_1 \exp(-i\omega_1 t)$ at a vectorial distance $R\vec{n}$ is $\vec{E_1}(t, \vec{R}) = \vec{E_1}(\vec{R})\exp(-i\omega t)$ where the spatial part has the following form:

$$\vec{E}(R) = \frac{\exp(ik_1R)}{4\pi\epsilon_0}\left\{\Big[3(\vec{n}\cdot\vec{\mu}_1)\vec{n} - \vec{\mu}_1\Big]\left(\frac{1}{R^3} - \frac{ik_1}{R^2}\right) + \Big[k_1^2(\vec{n}\times\vec{\mu}_1)\times\vec{n}\Big]\frac{1}{R}\right\} \quad (2.26)$$

where $k_1 = \omega_1/c$ is the wave number of the radiation emitted by the oscillating dipole. We immediately recognize two different contributions. The first addendum is the electric field of a static dipole while the last addendum scaling as $1/R$ is the one characteristic of a travelling radiation. If we now consider a second oscillating dipole $\vec{\mu}_2(t) = \vec{\mu}_2\exp(-i\omega_2 t)$. The interaction between the electric field irradiated by the first dipole and the second oscillating dipole is described by the scalar product $-\vec{E}_1(t)\cdot\vec{\mu}_2(t) = -\vec{E}_1(\vec{R})\cdot\vec{\mu}_2\exp(-i(\omega_1+\omega_2)t)$. The energy is given by $H_{12} = Re\big[-\vec{E}_1(\vec{R})\cdot\vec{\mu}_2\big]$.We obtain:

$$H_{12} = \frac{1}{4\pi\epsilon_0}\left\{\vec{\mu}_1\cdot\vec{\mu}_2 - 3(\vec{\mu}_1\cdot\vec{n})(\vec{\mu}_2\cdot\vec{n})\left(\frac{\cos(k_1R)}{R^3} + \frac{k_1\sin(k_1R)}{R^2}\right) + [\vec{\mu}_1\cdot\vec{\mu}_2 - 3(\vec{\mu}_1\cdot\vec{n})]\frac{k_1^2\cos(k_1R)}{R}\right\}. \quad (2.27)$$

For $k_1 R \ll 1$ the Hamiltonian corresponds to the one of an electrostatic interaction (see eq. 2.24). For $k_1 R \gg 1$ the dominant term is the one scaling as $1/R$ characteristic of a radiated electromagnetic field.
At the same time the dipole momentum $\vec{\mu}_2$ irradiates and the interaction of the radiation with the first dipole momentum can be computed in an analogous way. We obtain the same result as equation 2.27, we only need to replace k_1 by $k_2 = \omega_2/c$.

2.2.2 Resonant dipole-dipole Interaction

We now want to use the model of the retarded potential to describe a two body transition in Rydberg atoms. We consider the general two-body $r_1 + r_2 \rightarrow r_1' + r_2''$ where we have introduced the zero-field Rydberg state basis $|r\rangle = |n, l, j, m_j\rangle$. The label 1 and 2 is used to distinguish the two atoms. The single transition $r_1 \rightarrow r_1'$ and $r_2 \rightarrow r_2''$ can be described with oscillating dipoles as we have done in paragraph 2.2.1 with respective transition energies $\hbar\omega_{r_1 r_1'} = E_{r_1'} - E_{r_1}$ and $\hbar\omega_{r_2 r_2''} = E_{r_2''} - E_{r_2}$ and radiation wavenumber $k_1 = \omega_{r_1 r_1'}/c$ and $k_2 = \omega_{r_2 r_2''}/c$. An exchange of energy between the two Rydberg atoms, a two-body transition, is possible when the energy is conserved between the initial and final states. This corresponds to $\omega_{r_1 r_1'} + \omega_{r_2 r_2''} = 0$ or $k_1 = -k_2 = k$. We have that only resonant terms contribute to the two-body transition.
We are now interested in discussing the limit $kR \ll 1$ or $R \ll \lambda/2\pi$ where as we have seen in the previous paragraph the dipole-dipole term is dominant. Here $\lambda = 2\pi/|k|$ is the wavelength of the transition. In Rydberg atoms λ typically is of the order of mm to cm while the mean distance in a diluted cold Rydberg gas is of the order of tens of μm, we immediately see that in this case the dipole-dipole term is dominant. In this approximation we can thus consider for the dipole-dipole interaction the following form:

$$H_{dd} = \frac{\hat{\mu}_1 \cdot \hat{\mu}_2 - 3(\hat{\mu}_1 \cdot \vec{n})(\hat{\mu}_2 \cdot \vec{n})}{4\pi\epsilon_0 R^3} \tag{2.28}$$

where the dipole moment operator is defined as $\hat{\mu}_i = e\hat{r}_i$ where $\hat{r}_i$ is the position operator of the Rydberg electron for the $i-th$ atom. We have also replaced the vector by an operator in order to write the interaction term with the formalism of quantum mechanics.
We can calculate the dipole-dipole coupling energy $V_{dd} = \langle r_1, r_2 | H_{dd} | r_1' r_2'' \rangle$. It is important to remind that the dipole operators $\hat{\mu}_1$ and $\hat{\mu}_2$ act respectively on atom 1 and on atom 2. We quickly remind the dipole transition selection rules which impose for a dipole-dipole transition $\Delta l = \pm 1$ and $\Delta m_j = 0, \pm 1$. Using the scaling of the dipole momentum of eq. 2.8 we obtain that the dipole dipole coupling V_{dd} scales as the power

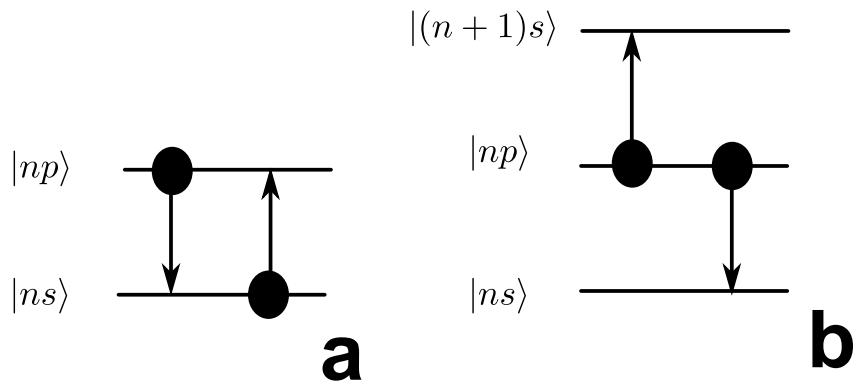

Figure 2.8: Scheme of a migration reaction (**a**) $ns + np \rightarrow np + ns$ and of a Förster resonance (**b**) $2 \times np \leftrightarrow ns + (n+1)s$ in caesium atoms.

n^4. We can rewrite the dipole-dipole coupling in the following form:

$$V_{dd} = \frac{C_3}{R^3} \propto \frac{n^4}{R^3} \tag{2.29}$$

where we have introduced the coefficient C_3 commonly used for describing dipole-dipole interaction.
A precise method for the calculation of C_3 is presented in [Walker and Saffman, 2008]. There the authors show that C_3 coefficient is the product of radial matrix dipole elements for the single dipole transition $r_1 \rightarrow r_1'$, $r_2 \rightarrow r_2''$ and a coefficient called $\sqrt{D}$ that takes into account the angular part of the Rydberg wavefunction.
Two examples of two-body transition due to a resonant dipole-dipole coupling between two Rydberg atoms are migration reaction and Förster resonance.

Migration reaction

Migration reaction consists in an exchange of excitation between two Rydberg states. One example of this kind of reaction is $np+ns \leftrightarrow ns+np$, which is an exactly resonant transition since the two dipole transitions involved are the same. The presence of an np excitation surrounded by ns atoms leads to the diffusion of the np excitation [Mourachko et al., 2004] when the atom in np exchanges its excitation with a closer atoms in ns state. This phenomenon called migration reaction finds interesting analogy

with excitation diffusion of excitons [Tokihiro et al., 1995, Mülken et al., 2007] or spin glasses theory [Castellani and Cavagna, 2005]. It could be also a way to implement experimentally a quantum random walk [Côté et al., 2006].

Förster resonance

The second kind of resonant dipole-dipole interaction is Förster resonance. That process consists in an internal energy exchange mediated by a dipole-dipole interaction where the two dipole transitions involved are not the same. Since the two dipole transitions involved in a Förster resonance have a priori two different transition frequencies (ω_1, ω_2) at zero field we would not expect any kind of interaction. If we then apply an external electric field the different Rydberg levels will be shifted of a different amount depending on their momentum angular state as we have seen in paragraph 2.1.3. It is thus possible to obtain the resonant condition $\omega_1 = -\omega_2$ for a precise external electric field.

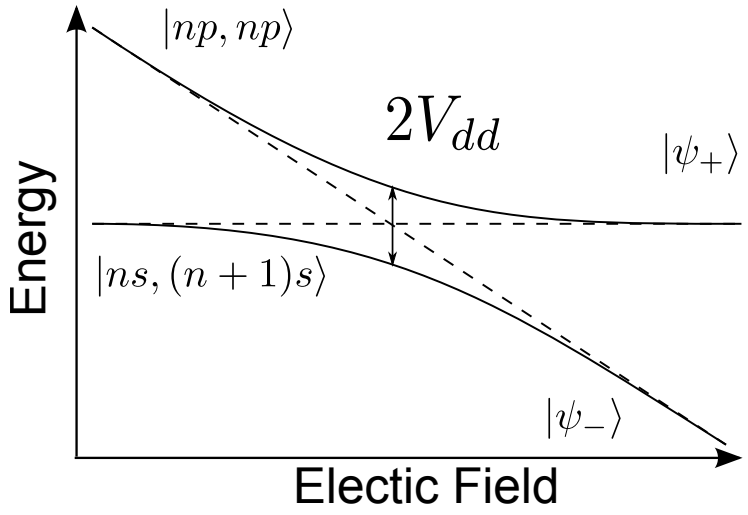

Figure 2.9: Scheme of an avoided crossing for a two-body Stark tuned Förster resonance $2 \times np \leftrightarrow ns + (n+1)s$. Dashed lines represent the energy of the two-atom states without dipole-dipole coupling. The solid lines are the energy considering the dipole-dipole coupling.

As an illustrative example we consider the general case of a Stark-tuned Förster resonance in Caesium atoms [Vogt et al., 2006] described by the following reaction:

$$2 \times np \leftrightarrow ns + (n+1)s. \tag{2.30}$$

The np Rydberg level can be tuned to the middle energy between ns and $(n+1)s$ exploiting the different Stark shift for the different Rydberg levels. For a precise value of the external electric field we obtain the following condition for the two two-atom states energy: $2E_{np} = E_{ns} + E_{(n+1)s} = E_R(\infty)$ where $E_R(\infty)$ is the total energy for two atoms placed at an infinite distance from each other. In the two-atom state basis $|np, np\rangle$, $|ns, (n+1)s\rangle$ we can write the total hamiltonian H_{tot} as the sum of the atomic contribution and dipole-dipole interaction term (see eq. 2.28). We obtain in a matrix representation:

$$H_{tot} = \begin{pmatrix} E_R(\infty) & V_{dd} \\ V_{dd}^{\dagger} & E_R(\infty) \end{pmatrix} \tag{2.31}$$

where $V_{dd} = \langle np, np|H_{dd}|ns, (n+1)s\rangle$. The eigenvalues of H_{tot} are $E_{\pm} = E_R(\infty) \pm V_{dd}$. The dipole-dipole interaction thus removes the degeneracy of two two-atom states because of an avoided crossing as sketched in fig. 2.9. The new eigenstates of the system are now a coherent superposition of the two two-atom states $|np, np\rangle$, $|ns, (n+1)s\rangle$:

$$|\psi_{\pm}\rangle = \frac{1}{\sqrt{2}}\big[|np, np\rangle \pm \frac{1}{\sqrt{2}}(|ns, (n+1)s\rangle + |(n+1)s, ns\rangle\big]. \tag{2.32}$$

In eq. 2.32 since we are not able to discern which one of the two atoms starting in np state will move to ns or $(n+1)s$ so we have to consider the entangled state $1/\sqrt{2}(|ns, (n+1)s\rangle \pm |(n+1)s, ns\rangle)$. Since the atoms np are indistinguishable, the coupling with the antisymmetric state $1/\sqrt{2}(|ns, (n+1)s\rangle - |(n+1)s, ns\rangle)$ is null. The dipole-dipole coupling entangled the two-atom state $|np, np\rangle$, $\frac{1}{\sqrt{2}}(|ns, (n+1)s\rangle + |(n+1)s, ns\rangle)$.

Since the dipole-dipole coupling produces a coherent superposition of two two-atom state we can expect that dipole dipole coupling drives a coherent evolution of the system. We first consider the laser excitation of the first two atoms in np state characterized by a Rabi frequency Ω_L.

If the dipole-dipole coupling is bigger than the laser excitation Rabi frequency, $\Omega \ll V_{dd}$, it is possible to excite only one of the two state of eq.2.32. In this case no coherent evolution is possible when the laser is turned off.

In the opposite case, $\Omega \gg V_{dd}$, the quantum state excited by the laser excitation at a resonant electric field is a coherent superposition of the two states of equation 2.32.

In this situation the dipole dipole coupling can drive a Rabi oscillation between the two states $|\psi_+\rangle$ and $|\psi_-\rangle$.

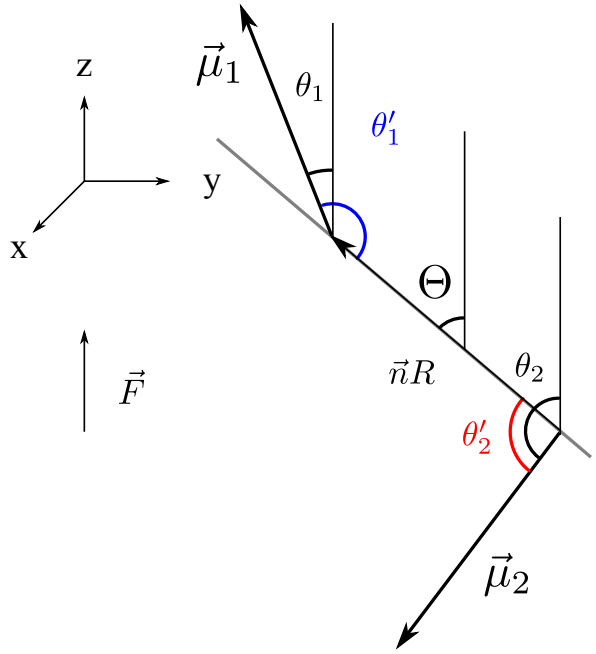

Figure 2.10: Scheme of the dipole-dipole interaction between two Rydberg atoms. $\vec{\mu}_1$ and $\vec{\mu}_2$ are the dipole momenta oriented in space. θ_1 and θ_2 are the angle respect the quantization axis z. We choose as quantization axis the direction of the electric field. θ_1' and θ_2' are the angle of the two dipole momenta respect to the direction $\vec{n}$ which corresponds to the direction identify by the two nucleus of the two Rydberg atoms. Θ is the angle of the molecular system composed by the two Rydberg atoms with respect to the quantization axis z. For the sake of simplicity in this scheme we impose $\varphi_1 = \varphi_2 = \Phi$.

2.2.3 Beyond dipole-dipole: multi-polar expansion

In paragraph 2.2.1 we have calculated the interaction between two Rydberg atoms considering the electrostatic interaction between the ionic cores and the Rydberg electrons of the two atoms. We report the interaction term $\hat{V}_{inter}$ already introduced in par. 2.2.1 (see also fig. 2.6):

$$\widehat{V}_{inter} = \Big[\frac{e^2}{R} - \frac{e^2}{r_{A2}} - \frac{e^2}{r_{B1}} + \frac{e^2}{r_{12}}\Big]$$

We have obtained that the first non-vanishing term of this interaction is the well known dipole-dipole interaction. If we consider now higher order of expansion we have that $\widehat{V}_{inter}$ can be written in a general form [Flannery et al., 2005], known as multi-pole expansion:

$$\widehat{V}_{inter} = \sum_{L_1,L_2=1}^{\infty} \sum_{M=-L_<}^{L_<} \frac{(-1)^{L_2} f_{L_1 L_2 M}}{R^{L_1+L_2+1}} \hat{Q}_{L_1 M}(\vec{r}_{1A}) \hat{Q}_{L_2 -M}(\vec{r}_{2B}) \tag{2.33}$$

where the multi-pole operator for each atom with composite electronic coordinates $\vec{r}$ relative to each ionic core is:

$$\widehat{Q}_{LM}(\vec{r}) = \Big\{\frac{4\pi}{2L+1}\Big\}^{1/2} r^L Y_{LM}(\hat{r}) \tag{2.34}$$

and where

$$f_{L_1 L_2 M} = \frac{(L_1+L_2)!}{[(L_1+M)!(L_1-M)!(L_2+M)!(L_2-M)!]^{1/2}}. \tag{2.35}$$

Y_{LM} are the well known spherical harmonics and $L_<$ is the smaller value of L_1 and L_2. The $\widehat{Q}_{LM}(\vec{r})$ corresponds to the L_i-th multi-pole moment of atom i. For example $L_1 = 1$ corresponds to the dipole moment of atom 1, $L_1 = 2$ is the quadrupole moment of atom 1 and so on.
The interaction term of eq. 2.33 is expressed in the frame of the non-rotating molecule considering the nuclei fixed in space and oriented along the quantization axis, the so called Born-Oppenheimer approximation. In this approximation only multi-pole interaction with even values of $L_1 + L_2$ conserve the electronic parity. This result can be obtained with consideration on the symmetry of the operator $\hat{V}_{inter}$. We start by considering a reflection σ_v respect to a plane containing the internuclear axis, that in the approximation of fixed nuclei corresponds to a parity transformation. Because of

their general properties [Hougen, 1970] the spherical harmonics transform as $(-1)^{L-\Omega}$ under σ_v, so the different terms of the sum of $\widehat{V}_{inter}$ transform under σ_v as $(-1)^{L_1+L_2}$, which implies that only even values of $L_1 + L_2$ conserve the electronic parity. This latter consideration can be expressed with the following condition:

$$(-1)^{l_{1,i}+l_{2,i}} = (-1)^{l_{1,f}+l_{2,f}} \tag{2.36}$$

where l represents the orbital angular momentum quantum number of the Rydberg electron, the indices i and f the initial and final states and 1 and 2 label the two Rydberg electron of Fig.2.6. The dipole-dipole interaction due to a Förster resonances (see eq. 2.30) obey the condition of parity expressed by eq.2.36.
However in a recent experiment [Deiglmayr et al., 2014] a dipole-quadrupole interaction between the pair states $ns\ n'f$ and $np\ np$ in an ultracold gas of Cs Rydberg atoms has been observed. This kind of interaction is supposed to be forbidden if we look at equation 2.36. In that work Deiglmayr et al. provide an empirical evidence of the inadequacy of the operator of eq.2.33 in describing a near resonance pair interaction. This result implicitly shows the limit of a Born-Oppenheimer approximation. Finally the authors proposed to incorporate the rotational-electronic interactions for odd values of $L_1 + L_2$ as an effective potential terms in 2.33.
This consideration on the limit of Born-Oppenheimer approximation can also be extended to the case of dipole-dipole interaction giving surprising results on the transition selection rules. We consider a Förster resonance in Cs atoms. We will examine two different cases:

$$np_{3/2}, m_j = \frac{3}{2} + np_{3/2}, m_j = -\frac{3}{2} \leftrightarrow ns_{1/2}, m_j = \frac{1}{2} + (n+1)s_{1/2}, m_j = -\frac{1}{2} \tag{2.37}$$

$$np_{3/2}, m_j = \frac{3}{2} + np_{3/2}, m_j = \frac{3}{2} \leftrightarrow ns_{1/2}, m_j = \frac{1}{2} + (n+1)s_{1/2}, m_j = \frac{1}{2} \tag{2.38}$$

In the first case $m_{j1} + m_{j2}$ is conserved, while in the second case not. This latter reaction would be forbidden if we maintain the Born Oppenheimer hypothesis. However if we remove the approximation which consider the nuclei oriented and fixed in space we will see that the latter reaction is allowed.
We start by calculating the matrix element for the first case eq. 2.37. For simplicity we will neglect the spin electron and we will restrict our consideration on the angular part of the Rydberg wave-function since the radial part does not play any role in determining the selection rules. Using the spherical harmonics, $Y_l^m(\theta_i, \varphi_i)$, we can write the angular part of the initial $|i\rangle$ and final $|f\rangle$ states in the following way:

$$\begin{aligned} |i\rangle =& |np, Y_1^1(\theta_1, \varphi_1)\rangle \otimes |np, Y_1^{-1}(\theta_2, \varphi_2)\rangle \\ |f\rangle =& |ns, Y_0^0(\theta_1, \varphi_1)\rangle \otimes |(n+1)s, Y_0^0(\theta_2, \varphi_2)\rangle \end{aligned}$$

In Fig.2.10 we report a scheme of this configuration where we define all the angles. $\vec{\mu}_1$ and $\vec{\mu}_2$ are the dipole momenta vector. The spatial orientation of the two dipole momenta is described by a couple of angles $(\theta_i,\ \varphi_i)$ for $1 = 1,\ 2$. We also introduce the molecular coordinates (Θ, Φ). In the scheme presented for the sake of clarity we sketch the particular case of $\varphi_1 = \varphi_2 = \Phi$. Once we define the coordinates of the system, we can write the dipole-dipole interaction operator:

$$\begin{aligned}\widehat{H}_{dd} =& \frac{\mu_1\mu_2}{4\pi\epsilon_0 R^3}(\cos\alpha - 3\cos\theta_1'\cos\theta_2') \\ =& \frac{\mu_1\mu_2}{4\pi\epsilon_0 R^3}(P_1(\cos\alpha) - 3P_1(\cos\theta_1')P_1(\cos\theta_2'))\end{aligned} \tag{2.39}$$

where α is the angle between the two direction (θ_1, φ_1) and (θ_2, φ_2) and $\cos\theta_i' = \vec{\mu}_i \cdot \vec{n}/\hat{\mu}_i$. We have also used the definition of the second Legendre polynomial $\cos\theta_i = P_1(\cos\theta_i)$. If we now want to calculate the matrix element $\langle f|\widehat{H}_{dd}|i\rangle$ we can write the Legendre polynomials as a sum of spherical harmonics functions [Messiah, 1961a]:

$$P_1(\cos\alpha) = \frac{4\pi}{3}\sum_{m=-1}^{1} Y_1^{m*}(\theta_1, \varphi_1)Y_1^m(\theta_2, \varphi_2) \tag{2.40}$$

$$P_1(\cos\theta_i') = \frac{4\pi}{3}\sum_{m=-1}^{1} Y_1^{m*}(\Theta, \Phi)Y_1^m(\theta_i, \varphi_i). \tag{2.41}$$

The matrix element is thus the product of two integrals in the solid angle $d\Omega_1$ and $d\Omega_2$:

$$\int Y_0^0(\theta_1,\varphi_1)Y_1^m(\theta_1,\varphi_1)Y_1^{+1}(\theta_1,\varphi_1)d\Omega_1 = \sqrt{\frac{9}{4\pi}}\begin{pmatrix}0 & 1 & 1\\ 0 & 0 & 0\end{pmatrix}\begin{pmatrix}0 & 1 & 1\\ 0 & m & 1\end{pmatrix}$$

$$\int Y_0^0(\theta_2,\varphi_2)Y_1^m(\theta_2,\varphi_2)Y_1^{-1}(\theta_2,\varphi_2)d\Omega_2 = \sqrt{\frac{9}{4\pi}}\begin{pmatrix}0 & 1 & 1\\ 0 & 0 & 0\end{pmatrix}\begin{pmatrix}0 & 1 & +1\\ 0 & m & -1\end{pmatrix}$$

where we use the properties of the Wigner 3j-symbols [Varshalovich et al., 1988, Messiah, 1961b]:

$$\int Y_{l_1}^{m_1}(\theta,\varphi)Y_{l_2}^{m_2}(\theta,\varphi)Y_{l_3}^{m_3}(\theta,\varphi)d\Omega = \sqrt{\frac{(2l_1+1)(2l_2+1)(2l_3+1)}{4\pi}}\begin{pmatrix}l_1 & l_2 & l_3\\ 0 & 0 & 0\end{pmatrix}\begin{pmatrix}l_1 & l_2 & l_3\\ m_1 & m_2 & m_3\end{pmatrix}$$

We finally obtain for the dipole-dipole matrix element:

$$\begin{aligned}\langle f|\widehat{H}_{dd}|i\rangle &= \frac{\mu_1\mu_2}{4\pi\epsilon_0 R^3}\left(-\frac{1}{3} - \frac{4\pi}{3}Y_1^{-1*}(\Theta,\Phi)Y_1^{+1*}(\Theta,\Phi)\right) \\ &= \frac{1}{6}\frac{\mu_1\mu_2}{4\pi\epsilon_0 R^3}(1-3\cos^2\Theta) \\ &= -\frac{1}{6}\frac{\mu_1\mu_2}{4\pi\epsilon_0 R^3}\sqrt{\frac{16\pi}{5}}Y_2^0(\Theta,\Phi)\end{aligned} \tag{2.42}$$

If we now consider the molecular system composed by the two ionic cores and the two Rydberg electrons, the dipole-dipole interaction matrix element can be rewritten:

$$\begin{aligned}\langle f,\Psi_f|\widehat{V}_{dd}|i,\Psi_i\rangle &= -\frac{1}{6}\frac{\mu_1\mu_2}{4\pi\epsilon_0 R^3}\sqrt{\frac{16\pi}{5}}\int Y_{L_f}^{M_f*}(\theta,\varphi)Y_2^0(\theta,\varphi)Y_{L_i}^{M_i}(\theta,\varphi)d\Omega \\ &= -\frac{1}{6}\frac{\mu_1\mu_2}{4\pi\epsilon_0 R^3}\sqrt{\frac{16\pi}{5}}\sqrt{\frac{5(2L_i+1)(2L_f+1)}{4\pi}}\begin{pmatrix} L_f & 2 & L_i \\ 0 & 0 & 0\end{pmatrix}\begin{pmatrix} L_f & 2 & L_i \\ -M_f & 0 & M_i\end{pmatrix}\end{aligned}$$

where L and M are the the orbital angular momentum and the magnetic quantum number of the molecular system. The non vanishing condition for the dipole-dipole matrix term impose the following selection rules:

$$\Delta L = 0, \pm 2 \tag{2.43}$$

$$\Delta M = 0 \tag{2.44}$$

$\Delta M = 0$ confirm what we have imposed at the begging, so that the conservation of M. It emerges that is possible to couple molecular state with higher orbital angular momentum L.
We now examine the reaction described by equation 2.38 which is in principle forbidden. In this case M is not conserved. The initial state can be written as:

$$|i\rangle = |np, Y_1^1(\theta_1,\varphi_1)\rangle \otimes |np, Y_1^1(\theta_2,\varphi_2)\rangle$$

In an analogous way, we have presented before, we can calculate the dipole-dipole matrix element:

$$\begin{aligned}\langle f|\widehat{H}_{dd}|i\rangle &= \frac{\mu_1\mu_2}{4\pi\epsilon_0 R^3}\left(-\frac{4\pi}{3}Y_1^{+1}(\theta,\varphi)Y_1^{+1}(\theta,\varphi)\right) \\ &= \frac{\mu_1\mu_2}{4\pi\epsilon_0 R^3}\left(-\frac{1}{2}\sin^2\theta e^{i2\varphi}\right) \\ &= -\frac{\mu_1\mu_2}{4\pi\epsilon_0 R^3}\sqrt{\frac{8\pi}{32}}Y_2^{+2}(\theta,\varphi)\end{aligned} \tag{2.45}$$

and considering the molecular system we obtain:

$$\begin{aligned}\langle f,\Psi_f|\widehat{H}_{dd}|i,\Psi_i\rangle &= -\frac{\mu_1\mu_2}{4\pi\epsilon_0 R^3}\sqrt{\frac{8\pi}{32}}\int Y_{L_f}^{M_f*}(\theta,\varphi)Y_2^{+2}(\theta,\varphi)Y_{L_i}^{M_i}(\theta,\varphi)d\Omega \\ &= -\frac{\mu_1\mu_2}{4\pi\epsilon_0 R^3}\sqrt{\frac{8\pi}{32}}\sqrt{\frac{5(2L_i+1)(2L_f+1)}{4\pi}}\begin{pmatrix} L_f & 2 & L_i \\ 0 & 0 & 0\end{pmatrix}\begin{pmatrix} L_f & 2 & L_i \\ -M_f & +2 & M_i\end{pmatrix}\end{aligned}$$

that now give the following selection rules:

$$\Delta L = 0, \pm 2 \tag{2.46}$$

$$\Delta M = +2 \tag{2.47}$$

We can see that contrary to what expect from the Born-Oppenheimer approximation, the dipole-dipole interaction between two Rydberg atoms can change the orientation of the nuclei, showing thus the limit of the Born-Oppenheimer approximation. It thus result that when we want to calculate the dipole-dipole interaction between a couple of Rydberg atoms we have also to take into account the internal degree of freedom of the ionic core.

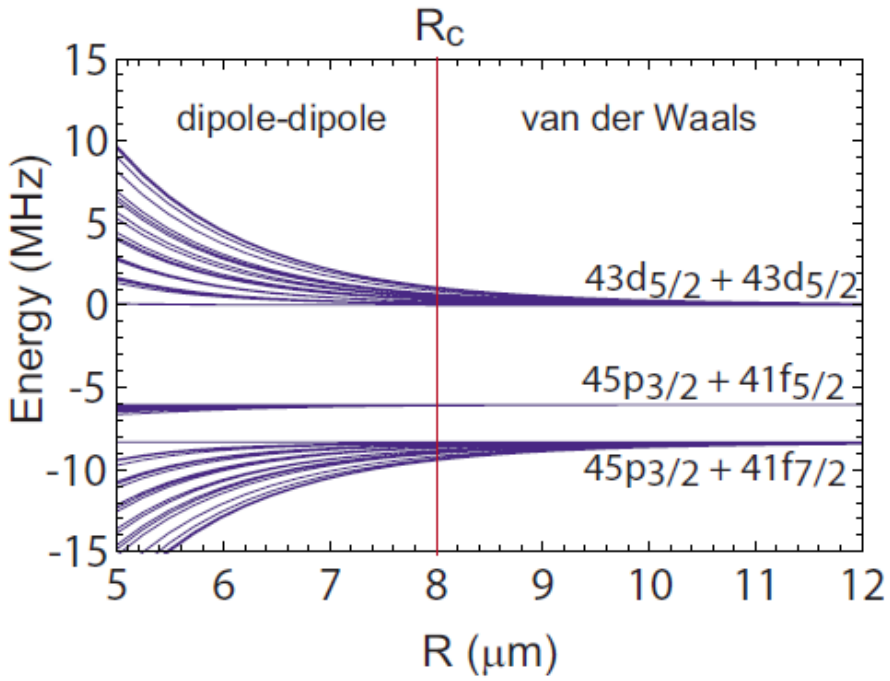

Figure 2.11: Potential energies for the interaction channel $43d_{5/2} + 43d_{5/2} \rightarrow 45p_{3/2} + 41f$ in Rubidium Rydberg atoms. The cut-off radius $R_c = R_{vdW}$ represents the distance scale for the transition from resonant dipole-dipole to van der Walls behaviour. This graphs has been taken from [Saffman et al., 2010].

2.2.4 Non-resonant interaction: van der Waals interaction

In paragraph 2.2.2 we have considered the resonant interaction between two Rydberg atoms. We have seen that in this condition the atoms interact basically with a dipole-dipole term which scales as C_3/R^3. We now want to study the case of a non resonant interaction between two Rydberg atoms. We consider two two-atom states $|r_1, r_2\rangle$ and $|r_1' r_2''\rangle$, close in energy, where the dipole transitions $r_1 \rightarrow r_1'$ and $r_2 \rightarrow r_2''$ are allowed and have different transition frequencies (i.e. $\omega_1 + \omega_2 \neq 0$). For simplicity we consider the case where r_1 and r_2 are the same Rydberg state. The proximity in energy of $|r_1, r_2\rangle$ and $|r_1' r_2''\rangle$ perturbs the energy because of the non negligible dipole-dipole interaction. The new interaction hamiltonian of the system written in the atomic basis

$|r_1' r_2''\rangle$ $|r_1 r_2\rangle$ has the following form:

$$H_{tot} = \begin{pmatrix} \hbar\Delta_F & V_{dd} \\ V_{dd}^\dagger & 0 \end{pmatrix} \tag{2.48}$$

where we have introduced the Förster defect Δ_F:

$$\hbar\Delta_F = (E_{r_1'} + E_{r_2''}) - (E_{r_1} + E_{r_2}) \tag{2.49}$$

and $V_{dd} = \langle r_1, r_2|\hat{H}_{dd}|r_1' r_2''\rangle = C_3/R^3$. Diagonalizing the matrix we obtain that the new eigenstate $|\widetilde{r_1, r_2}\rangle$ results shifted in energy respect to the initial state $|r_1, r_2\rangle$ by an amount:

$$\hbar\tilde{\Delta}_F(R) = \frac{\hbar\Delta_F}{2} - sign(\hbar\Delta_F)\sqrt{\frac{(\hbar\Delta_F)^2}{4} + \frac{C_3^2}{R^6}} \tag{2.50}$$

which plays the role of a potential between the atoms. In equation 2.50 we have used the relation $\frac{C_3^2}{R^6} = V_{dd}^\dagger V_{dd}$. The new eigenstate $|\widetilde{r_1, r_2}\rangle$ is a superposition of $\alpha|r_1, r_2\rangle + \beta|r_1', r_2''\rangle$ and the two components are in ratio $\alpha/\beta \approx V_{dd}/(\hbar\tilde{\Delta}_F - \hbar\Delta_F)$.
We immediately see that the ratio between the dipole-dipole coupling and the Förster energy mismatch play an important role. For $\hbar\Delta_F \ll V_{dd}$, the energy shift i.e. the potential curve is:

$$\hbar\tilde{\Delta}_F(R) \approx \frac{C_3}{R^3}. \tag{2.51}$$

We obtain again a dipole-dipole interaction as in the case of resonant interaction. While for $\hbar\Delta_F \gg V_{dd}$ the potential has the following form:

$$\hbar\tilde{\Delta}_F(R) \approx \frac{1}{\hbar\Delta_F}\frac{C_3^2}{R^6} = \frac{C_6}{R^6}. \tag{2.52}$$

that is known as a van der Waals potential. We can immediately find that the van der Waals coefficient C_6 has a rapid n^{11} scaling since we know $C_3 \propto n^4$ and $\hbar\Delta_F \propto n^{-3}$.
As an illustrative example taken from [Saffman et al., 2010] allows us to introduce a cut-off radius R_c which characterizes the distance scale for the transition from dipole-dipole to a van der Waals interaction. We consider the interaction between two Rubidium atoms in the same Rydberg state $43d_{5/2}$. We can see how the dipole-dipole coupling between $43d_{5/2} + 43d_{5/2}$ and $45p_{3/2} + 41f_{5/2(7/2)}$ strongly shifts the energy for interatomic distances smaller than a cut-off radius R_c, which we will call for the next part R_{vdW}. This parameter is defined as $\hbar\Delta = C_3/R_{vdW}^3$ and it is simply the value at which the dipole-dipole interaction is equal to the Förster defect. If we consider equation 2.52 for $R \ll R_{vdW}$ we recover the condition $\hbar\Delta \ll V_{dd}$: the interaction, as

for the resonant case, is a dipole-dipole interaction. In the opposite limit $R \gg R_{vdW}$ we recover again the condition $\hbar\Delta \gg V_{dd}$: in this latter case the atoms interact with van der Waals potential. In the case of a non-resonant interaction the inter-atomic distance play an essential role in determining the scaling of the interaction. It seems obvious that in the case of a resonant interaction $R_{vdW} \to \infty$; the there is no cut-off and the atoms interact only by a dipole-dipole interaction.

2.2.5 Principle of Rydberg blockade

The strong interactions (dipole-dipole or van der Waals interaction) can play an important role in the excitation of Rydberg atoms. If the dipole-dipole interaction is much bigger than the Rabi frequency of the laser excitation or much larger than the laser excitation linewidth it is possible to observe the inhibition of the Rydberg excitation. That phenomenon is the so called dipole blockade effect [Comparat and Pillet, 2010]. We consider an ensemble of atoms in the ground state $|g\rangle$ coupled to a Rydberg state $|r\rangle$ by a resonant laser transition (i.e. $\omega_{laser} = \omega_{gr}$). The laser transition is characterized by a Rabi frequency Ω_L and an effective linewidth Γ_L which takes into account the spectral linewidth of the laser excitation, the power broadening due to the laser intensity related to Ω_L, the Fourier broadening and the broadening due to the finite lifetime of the Rydberg state. $V(r)$ is the interaction (dipole-dipole or van der Waals) between two Rydberg atoms at a distance $\vec{r}$.
If $V(r) \gg \hbar\Gamma_L$ the energy shift due to the interaction makes the laser excitation no more resonant for the excitation of two Rydberg atoms while it continues to be resonant for a single excitation. The excitation of a Rydberg atoms can inhibit the excitation of a second one. This is what we call Rydberg blockade. In Fig.2.12 we report the energy level scheme for two atoms. We can see that the laser excitation is resonant for a single excitation so the transition $|g,g\rangle \to 1/\sqrt{2}[|g,r\rangle + |r,g\rangle]$ [Gaëtan et al., 2009, Urban et al., 2009] is allowed while the two-photon transition $|g,g\rangle \to |r,r\rangle$ is not allowed because of the shift due to the dipole-dipole interaction between the two Rydberg atoms. If the atoms are far enough that $V(r) \ll \Gamma_L$ the excitation of a second Rydberg atom is allowed. We can thus define a minimum distance r_b between two atoms in order to excite both to a Rydberg state. We call this distance the Rydberg blockade radius:

$$V(r_b) = \hbar\Gamma_L. \tag{2.53}$$

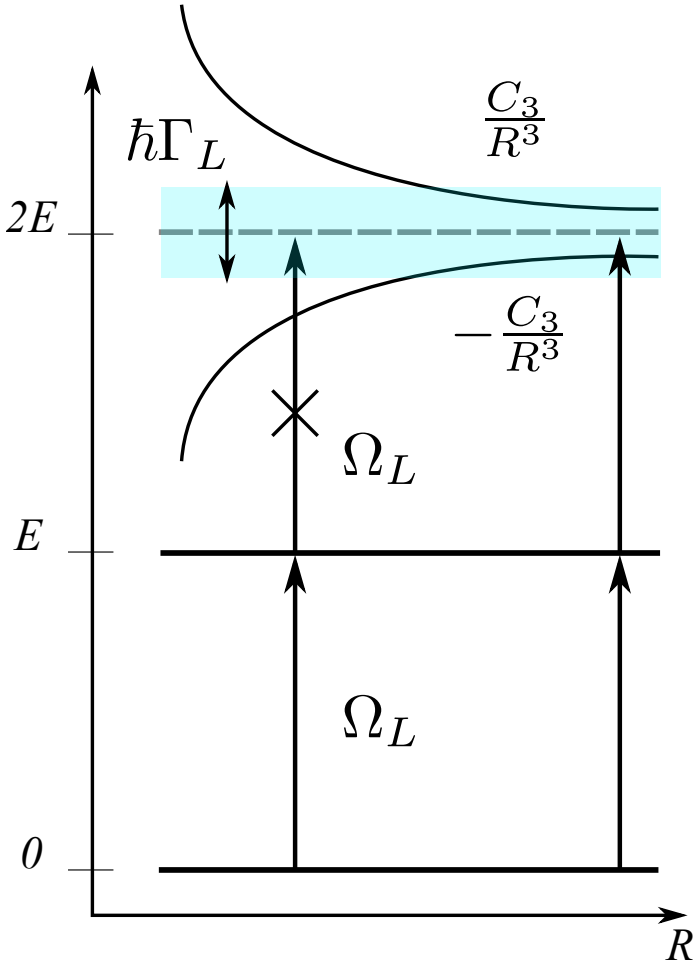

Figure 2.12: Principle of the dipole blockade between two atoms. Here we sketched the case of a dipole blockade where the interaction between atoms is a dipole-dipole interaction, but Rydberg blockade can be in general observed also in the case of a van der Walls interaction. R Represent the distance between two atoms, Ω_L is the Rabi frequency of the laser excitation. The light blue region represents the laser linewidth Γ_L. For smaller R the excitation of two Rydberg atoms is not allow while it is for larger R.

In the case of a van der Waals interaction we obtain the following equation for the blockade radius:

$$r_b \equiv \sqrt[6]{\frac{C_6}{\hbar\Gamma_L}} \tag{2.54}$$

The blockade radius identifies a volume inside which you can have only one Rydberg excitation.
The conditional excitation of Rydberg atoms has attracted the interest of the scientific community because of its potential application in quantum computing and quantum engineering. The exploitation of the dipole blockade [Saffman et al., 2010] has been proposed for the implementation of quantum gates and entanglement experiment. The entanglement of two ^{87}Rb atoms has been realized [Wilk et al., 2010] by the help of the blockade effect. In this experiment Wilk et al. use the dipole blockade effect in order to excite a two-atom entangled state between one atom in a ground state and one in a Rydberg state. The Rydberg blockade effect has been also used in the implementation of C-NOT quantum gate between two ^{87}Rb atoms [Isenhower et al., 2010].

3 Rydberg excitation & detection

The extreme sensitivity of Rydberg atoms to electric field plays a central role in many experiments with Rydberg atoms. The optimal control of external electric field to tune interaction or ionize Rydberg atoms have thus great importance in Rydberg atom experiment.
In this chapter we describe in detail the experimental set up used at Laboratoire Aimé Cotton for the investigation of few-body phenomena in a cold Cs Rydberg gas. The experimental set up is the one that has been used for the observation of a Stark-tuned four-body resonance [Gurian et al., 2012]. This experiment permits to excite a large number of Rydberg atoms (up to 10^5) in a defined state from a sample of cold Cs atoms. A good control of the electric field permits to tune the dipole-dipole interactions that lead to a Förster resonance. A state selective ionization technique permits to estimate the number of atoms detected in well precise Rydberg state.
Here we discuss in detail the specifics of this experiment starting from the excitation process of Rydberg atoms. After that we will describe how we apply the external electric field necessary for tuning the dipole-dipole interaction and finally we will discuss the complexity of ionization and detection of the Rydberg states.

3.1 Cold Cs atom source

3.1.1 Science chamber

The most common way to create a frozen Rydberg gas is to start from an already cooled sample of atoms. In [Metcalf and van der Straten, 1999, Letokhov, 2007] several techniques of atoms cooling and trapping are presented. In our experimental set up we use a standard Cs magneto-optical-trap. The Cs atoms are cooled and trapped in a common vacuum chamber where a pressure of 10^{-8} is maintained by a ionic pump (Varian 40 l/s). The Cs atom vapour continuously flow into the science chamber from an ampoule where Cs in solid state has been deposited. Because of the low melting temperature of Cs ($\sim 300°$ K) [Steck, 2003] there is no need of dispenser or oven to vaporize Cs. This peculiarity of Cs permits to obtain a high enough loading rate for

a 3D MOT even without a first step cooling with a Zeeman slower or 2D MOT. In addition in our acquisition sequence we do not switch the MOT so we do not need a high loading like the one used for Bose Einstein Condensate experiment with Cs [Kraemer et al., 2004]. The atoms are directly loaded from the ampoule to the science chamber where they are then cooled and trapped in a 3D MOT.

3.1.2 Trapping and repumping laser

We use a standard Cs MOT to cool down and trap the atoms. In Fig. 3.1 we highlight the two relevant transitions of the D2 line of Cs for cooling and trapping Cs atoms. The cooling transition is the $6S_{1/2}(F = 4) \rightarrow 6P_{3/2}(F' = 5)$ transition at $\lambda = 852$ nm. The cooling laser we use is an external cavity laser diode (Moglabs ECD-003). We stabilize the laser frequency with the well known saturated absorption technique [Letokhov, 2007, Preston, 1996]. In Fig.3.2 we report the saturated absorption profile of the D2 line. We can see the six saturated dips: three of them occur at the resonant frequency for the three optical transitions: $6S_{1/2}(F = 4) \rightarrow 6P_{3/2}(F' = 3)$, $6S_{1/2}(F = 4) \rightarrow 6P_{3/2}(F' = 4)$ and $6S_{1/2}(F = 4) \rightarrow 6P_{3/2}(F' = 5)$. These dips are labelled with the number 3, 4 and 5 which correspond to the value F'. The other three dips labelled respectively with co 4-3, co 3-5 and co 4-5 are the so called cross over dip that occur at the mean frequency of the two involved transitions. We stabilize the frequency locking the laser on the crossover 4-5. This cross-over is detuned a quantity of ≈ 125 MHz. We thus modulate the laser beam with an AOM with an operating frequency of 110 MHz. We modulate the AOM with a slightly different RF frequency of ≈ 112 MHz. Finally the first difracted order results shifted red detuned an amount of $\approx 12 - 13$ MHz respect to the $6P_{3/2}(F' = 5)$ that corresponds approximately to 2 and a half times the natural linewidth ($\Gamma = 2\pi \times 5.2227(66)$) MHz [Steck, 2003]) of the $6S_{1/2} \rightarrow 6P_{3/2}$ transition. We obtain a stabilized frequency up to 200 kHz.
The output power of the cooling laser is ≈ 40 mW. We resized the spot with a telescope and we obtain a collimated beam with a spot size diameter of ≈ 1 cm. In Fig. 3.3 (a) we present a sketch of our experimental set up. The 3 pink cylinder represent the 3 couple of counter-propagating laser beam tuned to the cooling frequency. They are obtained by splitting the output of the cooling laser in 5 beams. One of them, the beam along the vertical direction z (for the axis definition look at Fig. 3.3 (b)) is directly sent to science chamber and once transmitted is retro-reflected. The other four beams are superposed two by two in an counter-propagating configuration along the axis x and y. The three axis have been chosen in the way that x and y are parallel to the optic table while z is perpendicular. We balance the power in order to have ≈ 3 mW on each beam, except for the retro reflected beam where we directly send

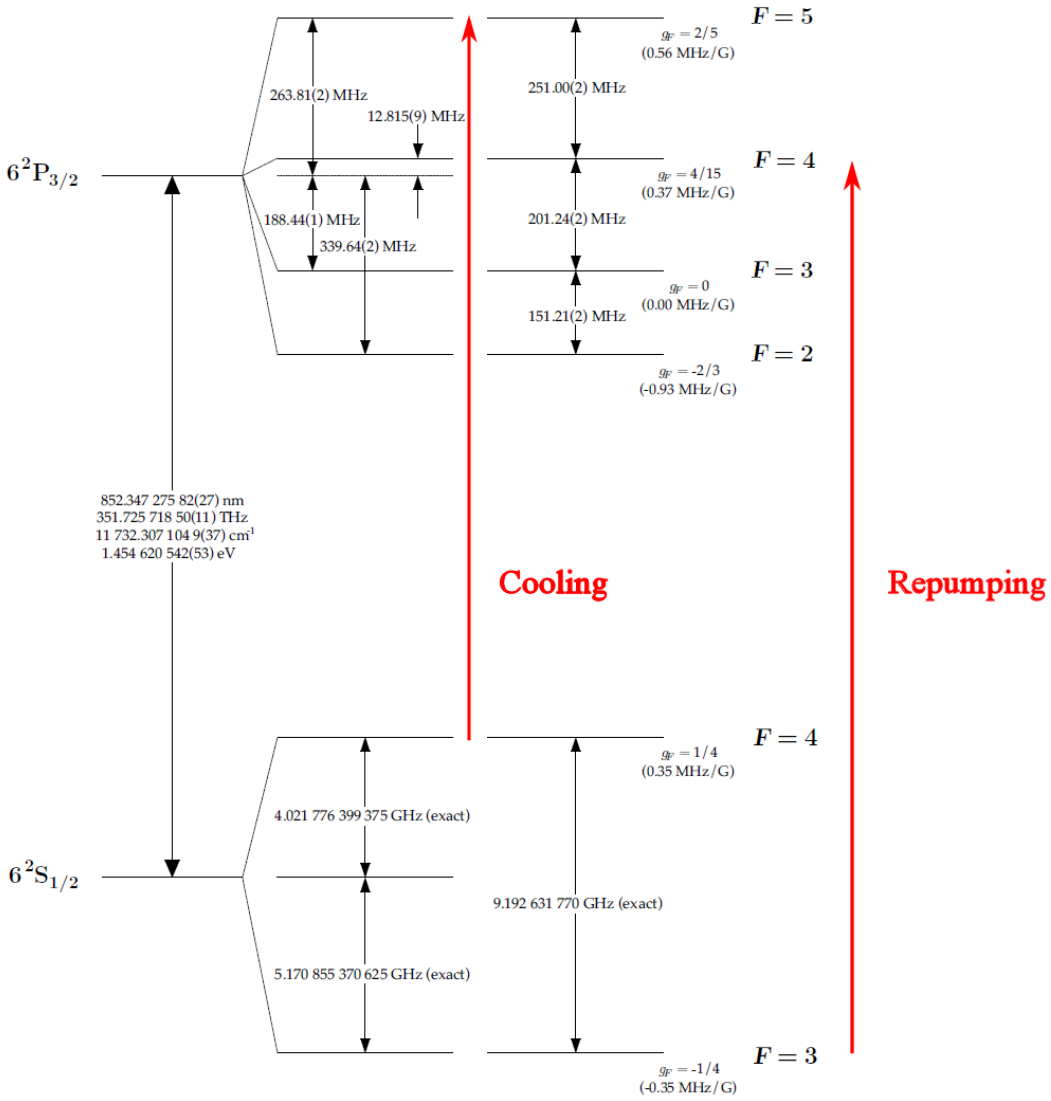

Figure 3.1: Relevant Cs level for cooling. The red arrow show the relevant transition for the cooling $6S_{1/2}(F = 4) \rightarrow 6P_{3/2}(F = 5)$ and the repumping $6S_{1/2}(F = 3) \rightarrow 6P_{3/2}(F = 4)$ processes.This figure has been taken from [Steck, 2003].

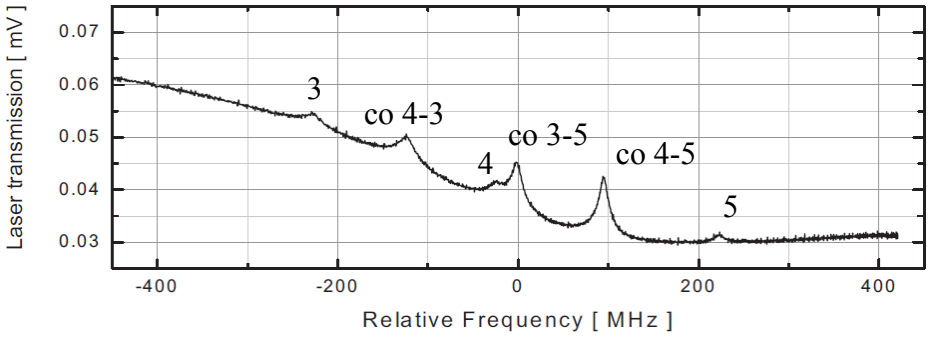

Figure 3.2: Saturated absorption dips for the D2 transition $6S_{1/2}(F = 4) \rightarrow 6P_{3/2}(F' = 3,\ 4,\ 5)$ of Cs. We label with 3, 4 and 5 the dips respectively due to the resonant transitions $6S_{1/2}(F = 4) \rightarrow 6P_{3/2}(F' = 3)$, $6S_{1/2}(F = 4) \rightarrow 6P_{3/2}(F' = 4)$ and $6S_{1/2}(F = 4) \rightarrow 6P_{3/2}(F' = 5)$. The dips labelled with co 4-3, co 3-5 and co 4-5 correspond to the saturated absorption dip at a cross over frequency. The numbers refer to the two transition involved in the cross-over.

≈ 6 mW on the z direction. These powers are large enough to saturate the transition ($I_{sat} = 1.1049(20)$ mW/cm^2 [Steck, 2003]).

The repumping laser, a distributed Bragg reflector (DBR) (SDL-5712-H1 by SDL Inc) with an output power of $\approx$ 50 mW, is locked to the transition $6S_{1/2}(F = 3) \rightarrow 6P_{3/2}(F = 4)$. The repumping is superposed only along one couple of counter-propagating cooling beams.
We finally obtain a Cs MOT with a typical density of several 10^{10} atoms/cm^3 and an estimated temperature of $\approx 100\mu$K slightly below the Doppler limit temperature fixed at $T_D = \hbar\Gamma/2k_B = 125.26\mu$K for the considered transition.The magnetic field necessary to trap the atoms is provided by two coils in an anti-Helmoltz configuration that produces a magnetic field gradient of 15 G/cm along the coils axis parallel to the z axis. The magnetic field gradient is two times smaller along the other direction. Three additional couples of coils have been mounted along the x, y and z direction to compensate the earth's magnetic field as well as spurious magnetic fields due to the ion pump. The magnetic field applied is of the order of 0.5 G. These three additional coils also allow to displace the zero of the magnetic field. They can be used to optimize the detected signal on the MCP moving the center of the MOT to better superposed

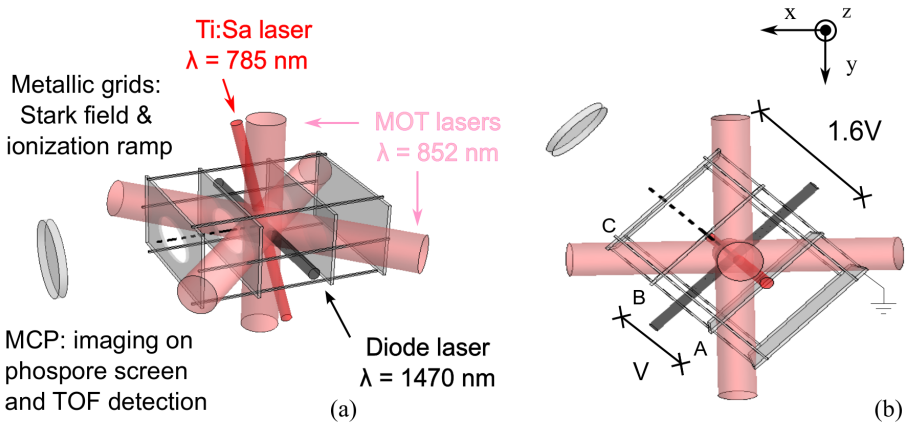

Figure 3.3: (a)Sketch of the experimental set up. The Rydberg atoms are excited at the crossing of the MOT beams $\lambda = 852$ nm (pink beams) and the the other two beams: laser diode $\lambda = 1470$ nm (black beam) and Ti:Sa $\lambda = 785$ nm (red beam). (b) Section from the top of the experiment. The outer metallic grid is ground connected. The other three grids are kept at a relative tension as denoted.

to the Rydberg excitation lasers.

3.2 Rydberg excitation

3.2.1 Three-photon excitation

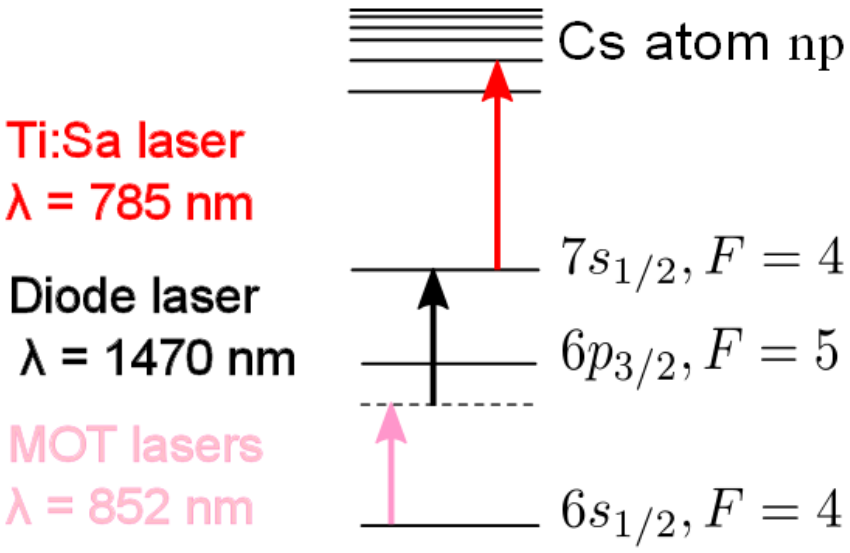

Figure 3.4: Scheme of the three photon excitation of Cs atoms in a Rydberg state np. The first step is the transition $6S_{1/2}, F = 4 \rightarrow 6P_{3/2}, F' = 5$ at $\lambda = 852$ nm provided by the laser used for the cooling transition of the MOT. The second step is the $6P_{3/2}, F = 5 \rightarrow 7S_{1/2}, F = 4$ transition at $\lambda = 1470$ nm. The last step is the $7S_{1/2}, F = 4 \rightarrow nP_{3/2}$ transition at $\lambda = 785$ nm.

In our experimental set up, as we will see in the next chapter, we are interested in exciting Rydberg atoms to a p level. Since the ground state of a Cs atom is a $6S_{1/2}$ level we need an odd number photon-transition. It is possible to directly excite a p Rydberg state with a one photon transition using an UV photon at $\lambda = 318$ nm [Saßmannshausen et al., 2013]. When using UV photon, particular attention must be paid to two-photon ionization. Two UV photons are energetically high enough to directly ionized a Cs atom. In addition the overlap between the wavefunctions of the ground state and the Rydberg state is small compared to the one we have for each

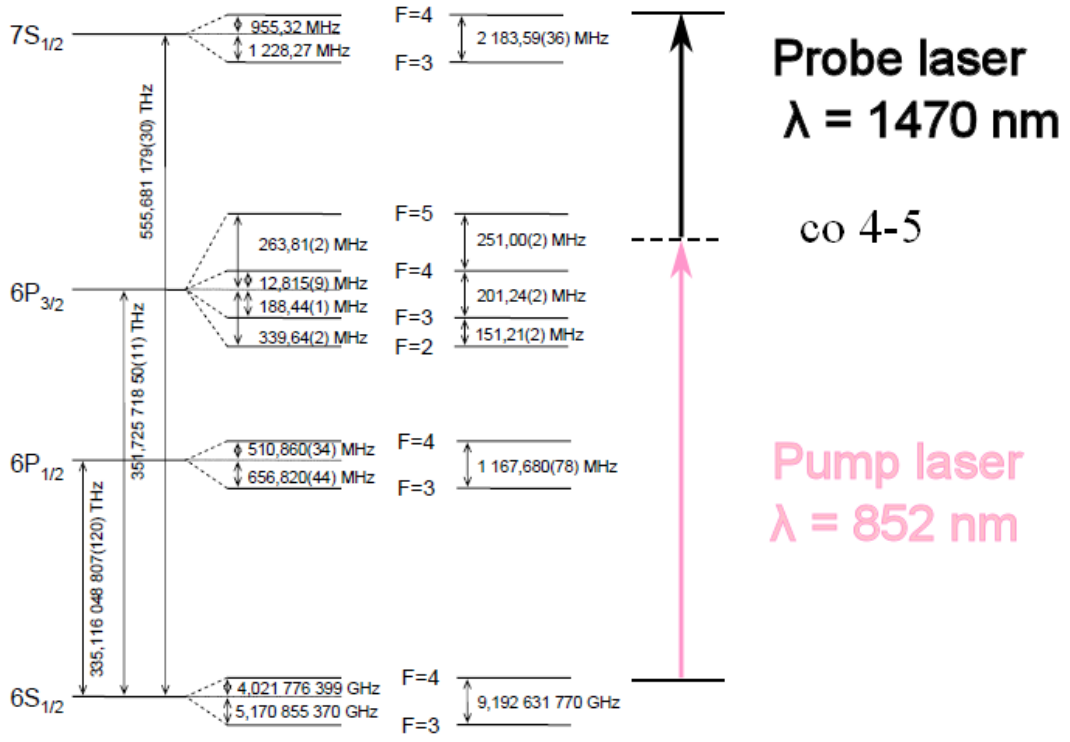

Figure 3.5: Excitation scheme used for the two color spectroscopy. A first laser lock at the cross over, the pump laser pumps the atoms in $6P_{3/2}, F' = 4$ and $6P_{3/2}, F' = 5$. The probe laser is tuned to the frequency resonant with $7S_{1/2}, F = 4$.

transition in a multi-step excitation. So a high power laser is necessary for a one-photon excitation. This aspect can limit the efficiency of the excitation because of the technical limitation (tunability and laser power) of the lasers working at this range of wavelength.

In our experimental set up we excite the p Rydberg state with a three-photon excitation as depicted in Fig. 3.4. The first step is the cooling transition of the MOT previously described. Since the cooling laser is used in a cw regime the Rydberg excitation cannot be a coherent excitation. In order to obtain a coherent excitation a solution would be to switch off the cooling laser during the Rydberg excitation and

using a second beam resonant to the cooling transition to provide the first photon. Since we want to observe dipole-dipole interaction between Rydberg atoms a coherent excitation of Rydberg state is not necessary and thus we can directly used the cooling beam without switching. This aspect highly increase the rate of measure acquisition. The second step is the transition $6P_{3/2}F = 5 \rightarrow 7S_{1/2}F' = 4$ at $\lambda = 1470$ nm. We use a laser diode with an external cavity (DL100 by Toptica) with an output power of 15 mW.
We stabilize the laser frequency with a so called two-color Doppler free spectroscopy. This technique requires a first laser, we call "pump" tuned to the cooling transition of Cs and a "probe" which is the laser we want to lock. In Fig. 3.5 we summarise the two laser transitions involved in the two color spectroscopy. The pump laser is first locked on the cross over 4-5 with a saturated absorption technique. The pump beam is then sent into a second Cs cell, sketched in Fig. 3.6, where it is superposed to 1470 nm laser, the "probe" laser. The pump laser excites atoms in $6P_{3/2}, F' = 5$ that moves at a positive velocity $v = \frac{(\omega_5-\omega_4)c}{(\omega_5+\omega_4)}$, where ω_5 and ω_4 are respectively the transition frequencies $6S_{1/2}(F = 4) \rightarrow 6P_{3/2}(F' = 4)$ and $6S_{1/2}(F = 4) \rightarrow 6P_{3/2}(F' = 5)$. It also excites atoms in $6P_{3/2}, F' = 4$ that moves at a negative velocity $v = \frac{(\omega_5-\omega_4)c}{(\omega_5+\omega_4)}$.
The second laser acts as a "probe" on the transition $6P_{3/2} \rightarrow 7S_{1/2}$. Because of the high power we send into the Cs cell, almost all the power of the $\lambda = 1470$ nm laser, we observe an Autler-Townes doublet. The Autler-Townes doublet has been estimated of the order of 46 MHz [Vogt, 2006]. The 1470 nm is then locked on one of the two absorption peak leading to a stabilized frequency up to 1 MHz. However the atoms we excite in the $7S_{1/2}$ in the Cs cell have a no null velocity. In order to excite atoms in the class velocity $v \approx 0$ for the transition $6P_{3/2}F = 5 \rightarrow 7S_{1/2}F' = 4$ we use an AOM with a carrier frequency 80 MHz. The diffracted order -1 is then sent to the MOT. This AOM is also used for switching the beam laser for a time of 1 μs. The combined effect of the Autler-Townes shift and the AOM modulation allows us to compensate the energy mismatch and finally excite atoms in the class velocity $v \approx 0$. This locking technique has evident limitation in term of stability since the Autler-Townes splitting we use for reducing the energy mismatch depends on the laser power and thus any fluctuation of the laser power has a direct effect on the stability of the frequency. However we are forced to use an Autler-Townes shift to tune the transition because of the limited frequency at which the AOM can operate. At this range of wavelength $\lambda = 1470$ nm we do not dispose of an adapt AOM.
The third step laser drives the transition $7S_{1/2} \rightarrow nP$. It is a Ti:sapphire ring laser from Sirah at $\lambda = 785$ nm working in cw mode with an output power of 1.6 W. The output beam is then collect in an optical fiber and then sent to the atoms. We are able

to couple until 600 mW of power that are entirely used for the Rydberg excitation. We use an external fiber coupled Fabry-Perot cavity (sold with the laser) to stabilize the laser frequency. This cavity is regulated in temperature but not locked on an atomic reference so the laser frequency drifts an amount of few MHz per minute. We are thus forced to continuously adjust the frequency. For that reason we are forced to collect the frequency of the Ti:Sa laser during our measurement in order to retrieve from the data collected only the one taken at resonance. More detail on the data treatment will be given in the final paragraph of this chapter. We monitor the frequency of Ti:Sa laser using a wavelength meter Angstrom WS-8 by High-Finesse and a software specially conceived for this laser. We switch the laser beam with an AOM and we obtain pulses of hundreds ns duration. The duration of this latter determine the duration of the Rydberg excitation.
In fig.3.3 (a) we present a sketch of the Rydberg excitation. The Rydberg atoms are excited at the at the crossing of the final two beams, which is set within the MOT. The beams of 1470 nm laser diode and of Ti:Sa are focused on the MOT in order to obtain an almost spherical volume excitation with a diameter of $\approx 300\mu$m. We finally obtained a linewidth of $\approx$ 10 MHz for the Rydberg excitation, mostly broadened by the finite lifetime of the intermediate level used for the excitation. A detuned excitation of the intermediate levels will reduce the Rydberg excitation linewidth. A so large linewidth prevents us to observe dipole-blockade effect unless in case of strong dipole-dipole coupling as in the case of Förster resonance, but at the same time allows us to obtain the possible largest Rydberg densities observed. We estimate to excite up to 10^5 atoms that roughly corresponds to half the atoms inside the excitation volume. We thus deduce that no blockade effect take place. In the next chapter we will discuss more in detail this aspect.

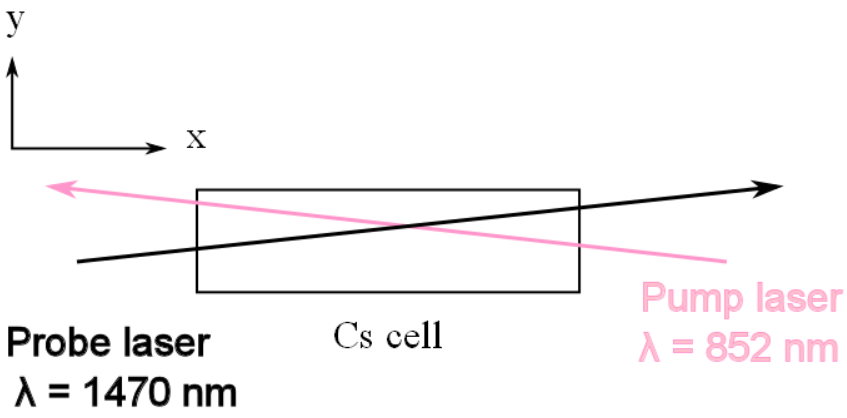

Figure 3.6: Scheme of the Cs cell used for the two color spectroscopy. The direction of the axis x define the positive direction for atoms velocity. In this sketch the angle between the two laser beams has been exaggerated for the sake of clarity.

3.2.2 Double excitation

In the presence of an external electric field the Rydberg state $nP_{3/2}$ is split in the two Zeeman sub-levels characterized by the magnetic quantum number $|m_j| = 1/2$ and $|m_j| = 3/2$. The splitting in frequency between these two Rydberg states can vary as a function of the external electric field and from a principal quantum number to another. We consider here the case of electric field range near a Förster resonance. This split in energy, we denote here with $\delta_{pp'} = (E_{np_{3/2},|m_j|=3/2} - E_{np_{3/2},|m_j|=1/2})/h$ can range between +200-235 MHz for $n = 31$ and +75-90 MHz for $n = 35$. We are thus able to resolve these two Rydberg states. The Stark energy levels $E_{np_{3/2},|m_j|=1/2}$ and $E_{np_{3/2},|m_j|=3/2}$ have been calculated using a C++ program developed here at Laboratoire Aimé Cotton. For more details see the reference [Huillery, 2013].
The possibility to resolve the two Zeeman sub-levels open the possibility to study the interaction between a mixture of two different Rydberg states. We briefly describe here the excitation technique we have implemented for the simultaneous excitation of $|np_{3/2}, |m_j| = 1/2\rangle$ and $|np_{3/2}, |m_j| = 3/2\rangle$. We used this technique for a short period of my thesis for an initial work studying a four-body interaction due to a mixture of $|np_{3/2}, |m_j| = 1/2\rangle$ and $|np_{3/2}, |m_j| = 3/2\rangle$. The Ti:Sa laser beam we use for the transition $7s_{1/2} \rightarrow nP_{3/2}$ is split in two beams: one can be tuned in frequency by passing through an AOM with a carrier frequency of 80 MHz in a double pass configuration.

The +1 order was retro reflected in order to double its frequency in the second passage through the AOM. This beam is then coupled to a fiber to the experiment. Changing the modulation frequency of the AOM we were able to span up to 180-190 MHz of modulation, with relatively small coupled power fluctuations (¡ 20 %).This beam was used to excite the Rydberg state $|np_{3/2}, |m_j| = 3/2\rangle$. For the second beam used for the excitation of the $|np_{3/2}, |m_j| = 1/2\rangle$ different solutions were possible depending on the value of $\delta_{pp'}$. In the case of $n = 31$, $\delta_{pp'} \approx 200 - 240$ MHz, the second beam was modulated with an AOM (carrier frequency 80 MHz) in a single pass configuration taking the -1 order in order to match the relative detuning $\delta_{pp'}$. For $n = 35$ $\delta_{pp'} \approx 75 - 90$ the second beam was still modulated with the same AOM taking now the +1 order of diffraction. The other cases between $n = 31$ and $n = 35$ have been obtained with different modulation of the two AOMs. This second beam is then superposed with the first one to be injected in the same fiber to ensure a perfect alignment of the two excitations. Varying the duration pulse of the two beams it was possible to control the relative density of the two Rydberg species. For lower value of the principal quantum number a large detuning between the two Rydberg excitation is necessary. An AOM with higher carrier frequency (200 MHz) is thus necessary to study $n = 28 - 29$ which require a relative detuning of 350-400 MHz.

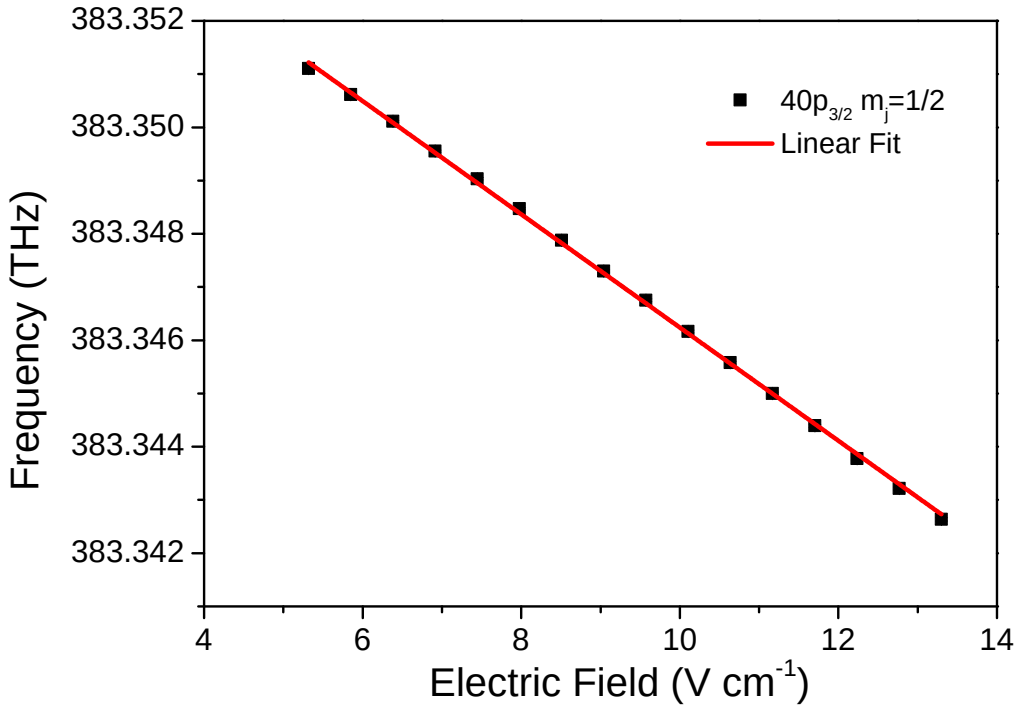

Figure 3.7: On the the y axis we plot the measured frequency of the Ti:Sa laser as a function of the external electric field. This plot corresponds to an experimental reproduction of a Stark map for the $|40p_{3/2}, |m_j| = 1/2\rangle$ Rydberg level. From a linear fit we obtain a slope of -1060 ± 7 MHz cm V^{-1}.

3.3 Rydberg detection

3.3.1 Electric field control

Since we want to study Stark-tuned Förster resonances we need an optimal control of the electric field applied to the Rydberg atoms. To this purpose 4 parallel 60 mm by 130 mm wire mesh grids of 80 μm thickness and 1 mm grid spacing have been placed inside the vacuum chamber in order to apply the necessary electric field for Stark tuning the Förster resonance. We estimate a net transparency of 90 % for the entire grids. The grids also provide the electric field for field ionization necessary for the

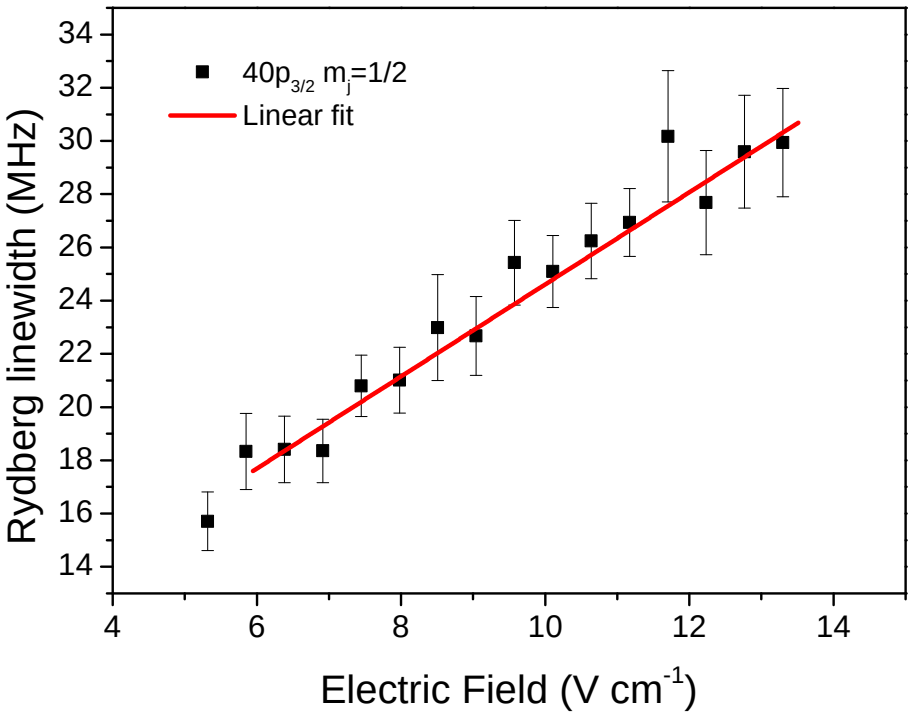

Figure 3.8: Plot of the Rydberg linewidth as a function of the electric field for the excitation of $|40p_{3/2}, |m_j| = 1/2\rangle$.

detection of Rydberg atoms. The center pair of grids is spaced by 1.88 ± 0.02 cm and the outer grids are 1.5 cm far from the inner grids. Voltage up to ± 5 kV can be applied arbitrarily to the four grids. In Fig.3.3(b) we report a sketch of the experimental set up: the four metallic grids are represented by the four rectangular grey panels. The outer grid is ground connected while the other three grids are connected to a voltage supplier. One of the grid is also connected to an high voltage supplier. In Fig.3.3(b) we indicate the voltage ratio kept between the three grids. The region with a voltage difference V is where Rydberg atoms are excited.
We keep the ratio fixed using an home-made voltage divider. This ratio has been chosen in order to minimize the inhomogeneities due to the holes the two grids on the left-side of the Rydberg excitation region. These two holes have been done in order to allow ions reach the MCP without loss acting as an electrostatic lens for ions

created with the field ionization. However they are at the same time the major cause of field inhomogeneity. Six additional small electrodes ground connected surround the excitation region at the grid edges. These additional electrodes have been placed to cancel stray fields effect. They could also be used to generate gradients or quadrupole fields. For the clarity of Fig.3.3(b) we do not report the six electrodes.
Because of the non perfect geometrical shape of the electrodes and the uncertainty of their positions, a calibration of mean electric field has been done before my arrival at the laboratory. It consists in an experimental reproduction of a the Stark map of a precise Rydberg state. For a fixed value of the applied voltage the Rydberg excitation frequency is registered using the wavelength meter used to control the Ti:Sa laser. The plot of the different excitation frequencies as a function of the applied voltage is then compared to the theoretical Stark map in order to precisely determine the distance between the inner grids. A relative uncertainty of 1 % has been obtained [Huillery, 2013].
As we have already mentioned before, the two holes in the two grids in between the cold Rydberg atoms and the MCP detector are the main source of the inhomogeneities of the electric field in the Rydberg excitation region. This spatial inhomogeneity of the electric field has a direct effect on the spatial distribution of the excited Rydberg atoms because Rydberg atoms are created when the laser excitation is tuned to the Stark shifted Rydberg level. Since the electric field is non-homogeneous the Stark-shift depends on the position of the atoms. We thus have a non-homogeneous excitation of the Rydberg atom sample. We can observe this effect looking at the imaging we obtain with the phosphor screen: we observe that scanning in frequency the Rydberg transition different part of the atomic sample are excited at different frequencies because of the field inhomogeneities. Because of this effect the Rydberg excitation linewidth gets broader.
We have estimated the broadening effect, due to the inhomogeneities, measuring the Rydberg excitation laser linewidth for the Rydberg state $40p_{3/2}$. We first select an electric field range where the Stark shift is linear as shown in 3.7. For this range of the electric field we measure the Rydberg excitation laser linewidth. In order to avoid any broadening effect due to a dipole-dipole coupling we choose an electric field range far from any Förster resonance. The Rydberg excitation laser linewidth is measured scanning the frequency of the Ti:Sa laser near the resonance. With a gaussian fit we obtain the linewidth of laser excitation plotted in Fig.3.8 as a function of the external electric field. We fit the data of Fig.3.8 with a linear curve and we obtain a slope of 1.7 MHz cm V^{-1} with an intercept equal to 7 MHz that corresponds to the laser excitation Rydberg linewidth at zero-field. Comparing this result with the slope of the Stark field effect for the $|40p_{3/2}, |m_j| = 1/2\rangle$ plotted in Fig. 3.7 we obtain a relative

inhomogeneity of the electric field of 1.6×10^{-3}.

3.3.2 Micro-channel plate detector

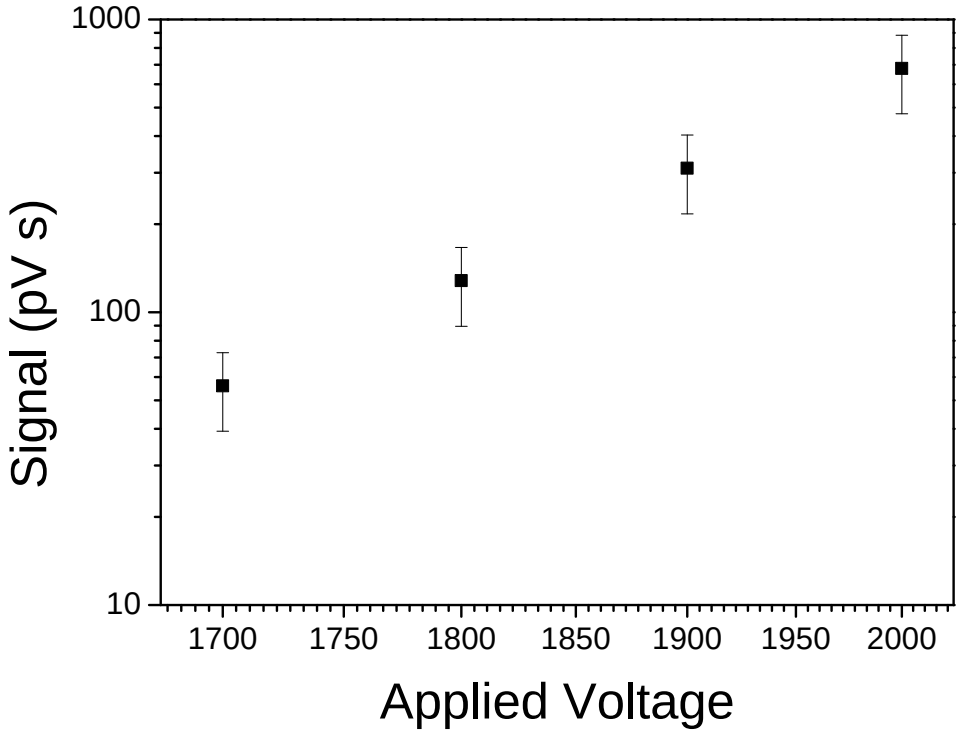

Figure 3.9: MCP calibration

The Rydberg atoms we excite with a three photon excitation are then detected by field ionization. We apply an high voltage ionization pulse at the two inner grids (the grid B in Fig.3.3(b) is switched to the ground and the high voltage is applied to the grid A). We use two high voltage switches (GHTS by Belkhe) to control the Stark and the ionization field. The ions are accelerated by the same ionization field and then detected by a micro-channel plate detector (MCP) placed at a distance of 210 mm from the MOT.
The MCP we use is a commercial one, the F2222-21PGF from Hamamatsu with an

effective surface of 20 mm and a nominal detection efficiency of 50%. An MCP detector is a two-dimension sensor that consists in a disk crossed by micro channels with diameter of the order of ≈ 10 μm. On the two sides of the disk two different voltages of the order of kV are applied. When an ion hits the inner surface of a micro-channel an avalanche reaction produces a flux of electrons. The amplification of the electron flux, the MCP gain, is determined by the potential applied to the MCP disk. The electron flux is then collected by an anode. The current at the output of the anode is amplified and then converted in a tension which is then collected by an oscilloscope (Waverunner 1 GHz by LeCroy).
The anode is coated on a side with a luminescent phosphor screen (P43 from Hamamatsu). When a burst of electrons generated by the avalanche process inside the micro-channel hits on the phosphor screen this latter emits light. We collect the light emitted with a camera and we thus obtain a 2D image of the incoming ions. The resolution of the image is related to the diameter of the micro-channel for the MCP we use are of 12 μm, but we have also to take into account the phosphor screen resolution which is of 30-50 μm [Hamamatsu,]. Considering we have an estimated enlargement of a factor 3 of ions cloud, we can finally estimate the initial position of the ions at the moment of the ionization with a precision of ≈ 15 μm. Because of the large number of Rydberg atoms, the ion impact clouds on the phosphor screen overlap and we usually cannot resolve single ions. This becomes possible for much smaller excitations of a few tens of Rydberg atoms.
We are more interested in collecting the signal which is proportional to the number of detected ions. We thus need to calibrate our MCP in order to find a correspondence between the MCP gain and the number of detected atoms. We thus measure the signal detected for a single ions for different MCP gain. In Fig.3.9 we report the single ion signal measured for different applied voltage i.e. gain. We then use the single ion signal to estimate the number of detected atoms for a fixed MCP gain taking into account the detection efficiency of 50 %.

3.3.3 Time-of-flight detection

As mentioned before in our experimental set up we are more interested in detecting the number of Rydberg atoms and also distinguish the different Rydberg states created. We have already seen in the previous chapter that it is possible to characterize a Rydberg state by its ionization field. We use a selective field ionization technique [Kellert et al., 1981]. This technique consists in ramping the ionization pulse in order to ionize different Rydberg states at different times, a simple way to ramp the voltage of the ionization pulse is by using an RC circuit. By apply a high voltage to a RC

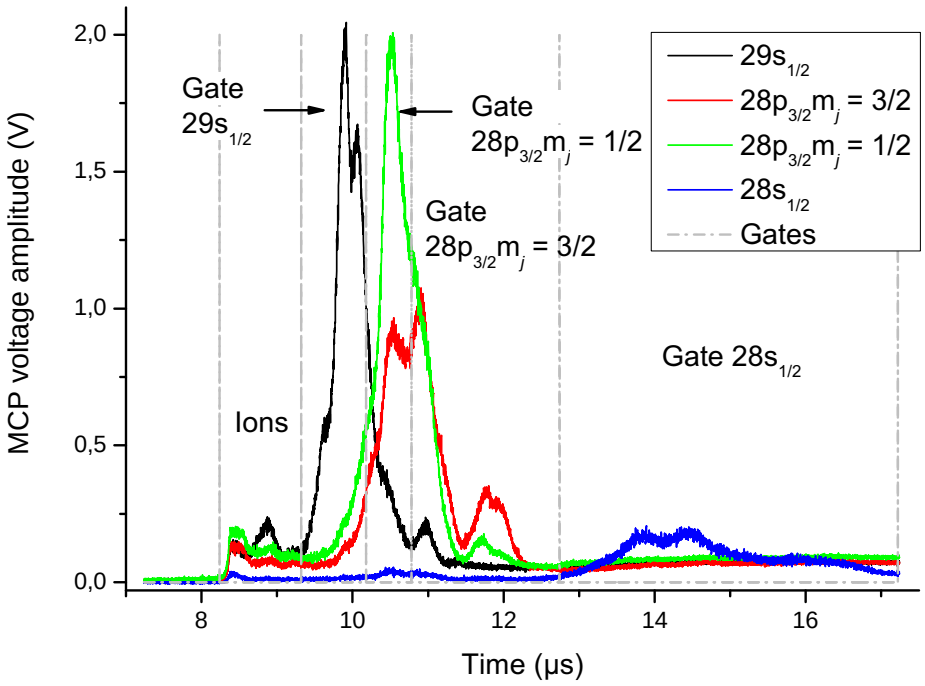

Figure 3.10: Time-of-flight signal (TOF) reference signal from a selective field ionization of the $|29s\rangle$, $|28s\rangle$, $|28p_{3/2}, |m_j| = 3/2\rangle$ and $|28p_{3/2}, |m_j| = 1/2\rangle$. Each state has been directly excited in a non-resonant electric field. The vertical lines delimit the gate time acquisition we define for the cros-talk analysis.

circuit we obtain an output signal with the characteristic exponential of a charging RC circuit. Once the RC circuit is connected to the grids the final result is a ramp of ionization with an exponential profile.
When we perform a selective field ionization the good discrimination between the different Rydberg signals is determined by two factor: the Rydberg lifetime and the cross-talk of the signals. A slow ionization ramp allow to reduce the cross-talk of the different Rydberg signals because the different Rydberg levels are ionized at well separated time. But the ramp time constant must stay significantly smaller than the Rydberg lifetime (in our experimental case $\approx 30\mu$s [Beterov et al., 2009]) because a too long time constant leads to a partial ionization of the lowest Rydberg state with a consequent spread of the time-of-flight signal and an increasing of the cross-talk.
The ramp time constant plays also an essential role in determining the shape of the acquired time-of-flight Rydberg signal. In Fig.3.10 we report the time-of-flight signal for 4 different Rydberg state: $|28s\rangle$, $|29s\rangle$, $|28p_{3/2}, |m_j| = 1/2\rangle$ and $|28p_{3/2}, |m_j| = 3/2\rangle$. The shape of the different Rydberg state is an intrinsic property of the ionization ramp we use. When we ramp the ionization field the Rydberg state follow adiabatically one of the curve of a Stark map. Once it arrive at an avoided crossing, the coupling with the other Rydberg states mix the two Rydberg states. The ionization ramp speed will condition whether the adiabaticity is still preserved or if the wavefunction splits the avoided crossing. Consequently, depending on the risetime of the electric field, an initial zero-field Rydberg state can be more or less mixed with other states when it reach the ionization threshold. We thus have several possible paths of ionization which lead to the observed spread of the detection signal of each Rydberg state.
The shape of the detected signal can be also spread because of dipole-dipole transition coupled by the black body radiation. We have already seen that black body radiation can lead to a dispersion of the population in neighborhood of a central Rydberg level. Reducing the delay between the excitation and the ionization as well the duration of the excitation pulse can reduce this dispersion effect.
We can see that several effects concur in the ionization of the Rydberg atoms. If we want well separate the different Rydberg signal a good compromise between the duration of the excitation, the Rydberg lifetime and the rapidness of the ionization must be found.
For that reason in our experimental set up we shape the ionization ramp with a modified RC circuit: the ramp of ionization has a first steeper ramp with a characteristic rising time $\tau \approx 400$ ns where the voltage rise up to ≈ 60 %. The second part of the ionization ramp is then driven by a longer characteristic rising time of $\tau \approx 500$ ns. With this configuration of the ramp we fast achieve the ionization limit of the higher Rydberg state we want to detect and the second part of ramp allows to better resolve

the different Rydberg signals. Moreover additional data processing can help in reduce the impact of cross-talk between the different Rydberg signals. We will discuss more in detail this aspect in the final paragraph of this chapter.

3.4 Experimental control

We finally conclude this chapter presenting the sequence of operation to be done for measuring the population of the different Rydberg state for a fixed Stark field. The experiment is controlled by a digital delay generator (DG 645 by Stanford Research System) that send the necessary TTL for controlling the AOM used for switching the 1470 nm and the Ti:Sa laser beam and the high voltage switches used for switching the ionization ramp and the Stark field. In Fig.3.11 we report a sketch of the experimental sequence. We first fix the Stark field at which we want measure the population of the different Rydberg state. We then excite the Rydberg atoms. As we have previously introduce the laser beam at $\lambda = 1470$ nm is switched on for 1μs while the Ti:Sa laser beam for 200 hundred of ns. This latter pulse thus determine the duration of the entire Rydberg excitation. We can vary the duration of the Rydberg excitation pulse in order to study different Rydberg density regime. The pulse duration have been chosen in order to avoid as much as possible the creation of ions during the Rydberg excitation. The creation of ions can lead to spurious effect like a local electric field which enhance the electric field inhomogeneities, or a trivial detection of Rydberg atoms.
At the end of the Rydberg excitation we apply the ionization ramp at a variable delay that ranges between 0-4 μs. The different delay allows to study the temporal evolution of the system. Once the Rydberg atoms are ionized they are immediately accelerated towards the MCP detector by the same ionizing field. We then collect a tension signal from the MCP with an oscilloscope.
The experimental cycles works at a repetition rate of 10 Hz. At each acquisition we register the oscilloscope signal, the voltage difference between the inner grids and the Ti:Sa laser wavelength using a Labview interface. We finally obtain for a fixed value of the Stark field the number of the detected atoms in the Rydberg states involved in the processes investigated.

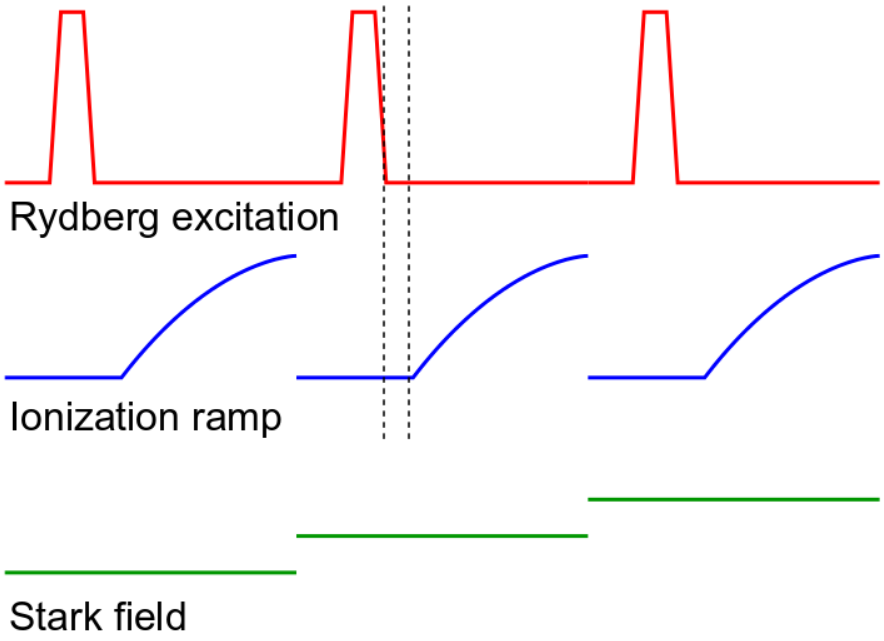

Figure 3.11: Experimental sequence of the excitation and detection of the Rydberg state. We first fix the Stark field (green line) at which we want measure the different Rydberg populations. After that we excite the Rydberg atoms with an excitation pulse of $\approx$ 200 ns (red line). We then apply the ionization ramp with a certain delay after the Rydberg excitation τ_{delay} $0-4\mu$s (blue line). We collect the signal and we repeat the sequence for an another Stark field.

3.4.1 Cross-talk analysis

In chapter 2 we have already introduced the two-body process known as Förster resonance. We have seen that in the case of Cs atoms it is possible to induce a transfer of population from a $|np_{3/2}, np_{3/2}\rangle$ to a $|ns, (n+1)\rangle$ two-atom state. This transfer of population is possible at a well defined external electric fixed. When we thus tune a Förster resonance the time-of-flight obtained from the selective field ionization is the result of the superposition of at least three different Rydberg states. If we want extrapolate the population of the different Rydberg state an additional elaboration of the time-of-flight is necessary.
In order to explain the procedure used to extract the Rydberg populations and remove the cross-talk we propose here the discussion of analysis we have done for the detection of the Förster resonance $2 \times 28p_{3/2} \rightarrow 28s + 29s$, but this method is still valid for the other Förster resonance as well as for other few-body process which involve a transfer of population.
We first collect a reference signal for each one of the Rydberg states involved in the interaction. These signals are taken at fixed electric field where no resonance are predicted. In Fig. 3.10 we have plotted the reference signal collected with the oscilloscope for the Rydberg state $|29s\rangle$, $|28s\rangle$, $|28p_{3/2}, |m_j| = 3/2\rangle$ and $|28p_{3/2}, |m_j| = 1/2\rangle$. The vertical dashed lines delimit the integration gates we define on the oscilloscope for each Rydberg state. The signal collected in each gate is related to the number of atoms detected in the corresponding Rydberg state; in order to estimate the number of detected atoms we divide the collected signal by the coefficient related to the MCP setted gain using the calibration we have already presented in paragraph 3.9. In the conversion we also take into account the MCP detection efficiency which is of 50 %.
We add two additional gates in our detection: one gate is defined at the very beginning of the time of flight signal and we use it to estimate the offset signal; the second one labelled with ions was initially used to quantify the number of ions created before the field ionization. The presence of ions before the ionization ramp is mostly due to dispersion of the Rydberg population produced by the blackbody radiation which can disperse the population even to higher state when a blackbody photon is absorbed.
We can immediately observe that the $|28p_{3/2}, m_j = 3/2\rangle$ and $|28p_{3/2}, m_j = 1/2\rangle$ signal are almost overlapped so we are not able to distinguish these two populations between the original p state. On the other side $29s$ and $28s$ states are well separated and it is thus possible to distinguish between the two population. Nevertheless we have a non-negligible crosstalk between the signals. We can estimate the crosstalk and subtract it from the total signal. The principle of this analysis is the following. Each signal reference can be written as the sum of the contribution of the different gates. If we

restrict to the gate associated to the Rydberg state we have that each signal is the sum of four signal gates. We can thus obtain a 4×4 matrix which relate the reference signal to the gate components. If we now want to retrieve from the collected signal the population of the different Rydberg states we have to multiply the collected signal written as a sum of its signal gate by the inverse of that matrix. We estimate that the residual cross-talk between the s and the p are of the order of ± 0.5 % after correction, while we have an estimated residual cross-talk of $\pm$ 5% or more between the two p states.
The 4×4 matrix obtained from the crosstalk analysis is then used for estimate the different Rydberg populations. For each value of the electric field we realize ~ 300 acquisition. From this we select 50 to 150 data points. The selection is necessary as the Rydberg excitation laser is not frequency locked; for that reason we measure at the same time the frequency of the Ti:Sa. We first select data within ± 3 MHz of the optimum excitation frequency while we observe an excitation linewidth of ± 5 MHz. After this first selection we keep all the data points in an interval of $\pm$ 5% in Rydberg atom number. After averaging N points, the statistical error of the mean (SEM) is estimated by the usual formula of the measured standard deviation σ divided by $\sqrt{N}$. From the data points we finally obtain a mean value of the Rydberg population. We thus plot the percentage of atoms that are transferred from the initial Rydberg state to the product of the reaction as a function of the external electric field. With this procedure we are able to measure the population of the Rydberg states with an error smaller than the 0.5 %.

4 Quasi-forbidden Förster resonances

A Förster resonance is a two-body process due to a dipole-dipole coupling between two resonant two-atom states. It was first observed during the 80s [Safinya et al., 1981] in an effusive thermal beam of Na atoms, where a transfer of population due to the resonant reaction $ns + ns \rightarrow np + (n-1)p$ has been detected. The dipole-dipole interaction coupled the two-body states of the reaction; the final eigenstate of the system is a superposition of the two two-body states. Förster resonances can be detected measuring the transfer of population from a two-body state to another.
The name of "Förster resonance" has been given by Thad Walker and Mark Saffman [Walker and Saffman, 2005] in analogy with FRET (Fluorescence Resonant Energy Transfer). This process was first presented by Theodor Förster [Förster, 1948], after a purely quantum description by Perrin [Perrin, 1932], to explain a non radiative exchange of energy due to a dipole-dipole coupling between two fluorophores called donor and acceptor. The exchange of energy in a FRET process is detected by the fluorescence emitted by the acceptor. FRET resonances are largely used in molecular imaging and microscopy because of their extreme sensitivity to molecular conformation, association and separation in the 1-10 nm range [Jares-Erijman and Jovin, 2003, Weiss, 1999, Rizzo et al., 2004]. FRET seems also to play a leading role in the light harvesting process [Oar et al., 2006, Collini et al., 2010, Ajayaghosh et al., 2007].
In Rydberg physics the important analogy of Förster resonance with FRET has opened the way to use of Rydberg atoms for the study of quantum energy transport induced by 2-body FRET. A recent experiment has shown the diffusion of a Rydberg excitation in a frozen Rydberg gas [Günter et al., 2013] using an imaging technique based on an EIT scheme. Moreover the dipole-dipole coupling in Förster resonance has been used for study the propagation of a Rydberg excitation in a chain of three Rydberg atoms [Barredo et al., 2015].

4.1 Förster resonance in Cs atoms

As we have seen in chapter 2, in order to observe a Förster resonance the two two-body state coupled by the dipole-dipole interaction must be resonant. The most common

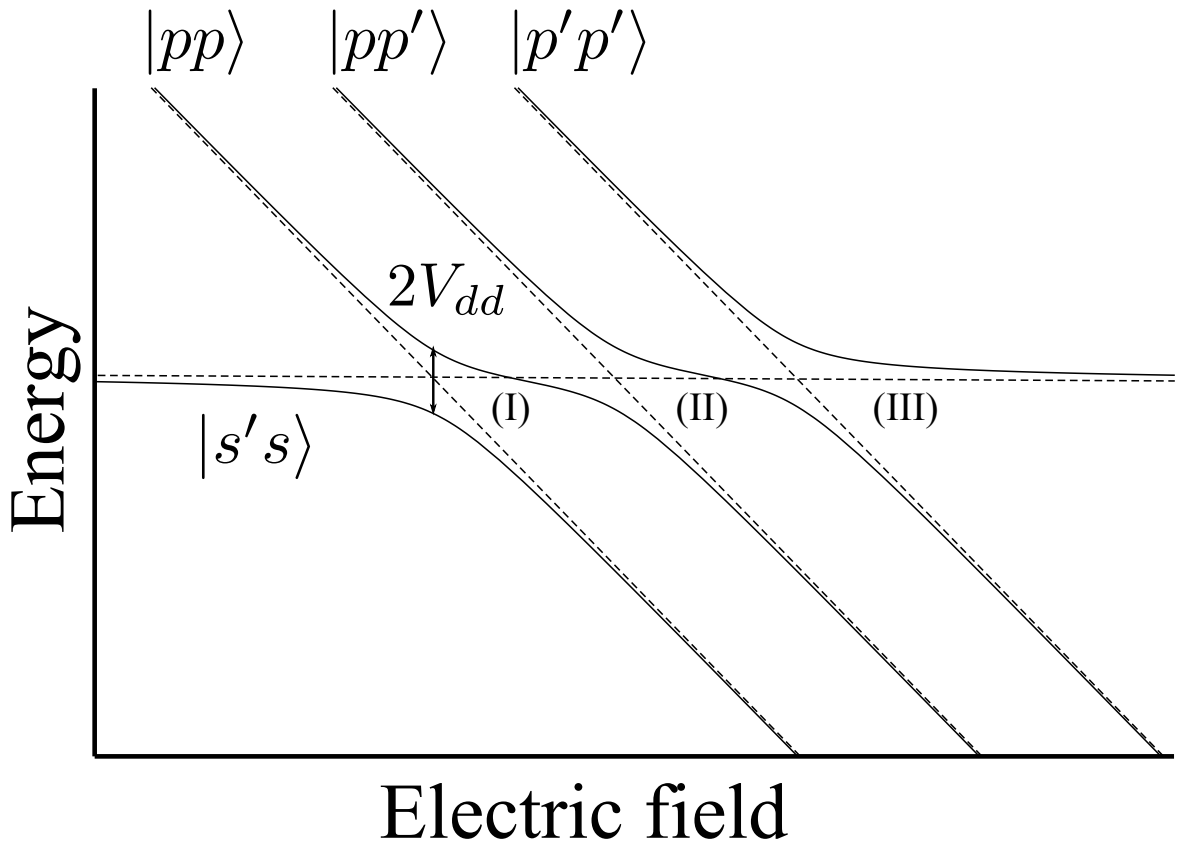

Figure 4.1: Scheme of an avoided crossing for a two-body Stark tuned Förster resonance. We can see the three avoided crossings (I), (II) and (III) respectively due to the Förster resonances described by equations 4.2-4.4 and 4.3. The p, p, s and s' respectively correspond to $|np_{3/2}, |m_j| = 1/2\rangle$, $|np_{3/2}, |m_j| = 3/2\rangle$, $|ns_{1/2}\rangle$ and $|(n+1)s_{1/2}\rangle$ Dashed lines represent the energy of the two-atom states without dipole-dipole coupling. The solid line are the energies considering the dipole-dipole coupling.

technique is to apply an external electric field to Stark shift the Rydberg levels and thus obtain a resonant condition for the two-atom states.
By applying a suitable external electric field we are able to tune Förster resonance for different Rydberg states. This is one of the interesting aspect of Förster resonances: its scalability for different principal quantum number and its reproducibility in different atomic species. It can be observed for large range of principal quantum numbers n and in principle for any kind of atomic species (Na, Rb, Cs etc...). In cold Cs atoms a series of Stark tuned Förster resonance described by the equation:

$$2 \times np_{3/2} \leftrightarrow (n+1)s + ns \tag{4.1}$$

have been observed for n ranging between 25 and 41 [Vogt et al., 2006]. The Stark effect due to an external electric field shifts the Rydberg states $np_{3/2}$, ns and $(n+1)s$ in different ways. It is thus possible to tune the energy of the np state at the average energy of ns and $(n+1)s$. In this case as we have already seen in the previous chapters the resonant dipole-dipole coupling removes the degeneracy of the two-atom states $|np_{3/2}, np_{3/2}\rangle$ and $1/\sqrt{2}(|(n+1)s, ns\rangle + |ns, (n+1)s\rangle)$ and the new eigenstates of the system are a superposition of these two latter states.
The Stark effect also removes the degeneracy of the $np_{3/2}$ Rydberg level and it is thus possible to resolve $|np_{3/2}, |m_j| = 1/2\rangle$ and $|np_{3/2}, |m_j| = 3/2\rangle$ states. The equation 4.1 describing the Förtser resonance thus split in three possible Förster resonances depending on absolute value of the magnetic quantum number m_j of the initial state. We have the case where the two atoms are in the same initial state:

$$2 \times |np_{3/2}, |m_j| = 1/2\rangle \leftrightarrow |ns\rangle + |(n+1)s\rangle \tag{4.2}$$
$$2 \times |np_{3/2}, |m_j| = 3/2\rangle \leftrightarrow |ns\rangle + |(n+1)s\rangle \tag{4.3}$$

or the case of a mixture:

$$|np_{3/2}, |m_j| = 1/2\rangle + |np_{3/2}, |m_j| = 3/2\rangle \leftrightarrow |ns\rangle + |(n+1)s\rangle \tag{4.4}$$

In Fig. 4.1 we schematically present the energy levels for the three kind of Förster resonances. The three avoided crossings (I), (II) and (III) respectively denote the Förster resonances described by equations 4.2-4.4 and 4.3. We can see the relative positions of the avoided crossing at which we would expect the Förster resonances. We consider a linear Stark shift for all the energy levels which is consistent with the Stark map of Cs calculated in [Gurian et al., 2012, Huillery, 2013].
The experimental excitation of a mixture of $|np_{3/2}, |m_j| = 1/2\rangle$ and $|np_{3/2}, |m_j| = 3/2\rangle$ can be realized with excitation scheme we present

in paragraph 3.2.2 of chapter 3. We have also reported the detuning $\delta_{pp'}$ between the two Zeeman sub-levels for different principal quantum numbers: the detuning $\delta_{pp'}$ ranges between 75-90 MHz for $n = 35$ up to 200-240 MHz for $n = 31$. This range for the detuning allows the resolution of the three Förster resonances described by equations 4.2-4.4.

4.2 Quasi-forbidden resonance

4.2.1 Initial purpose: four-body interaction

The generalization of two-body FRET to a N-body process is a great challenge for the comprehension of many-body physics. In this sense a pioneering work where a direct observation of a Stark-tuned four-body resonance has been realized [Gurian et al., 2012]. In this work Gurian et al. observed in a cold Cs Rydberg gas a resonant energy transfer due to a four-body interaction described by the transfer equation:

$$4 \times 23p_{3/2} \rightarrow 2 \times 23s + 23p_{1/2} + 23d_{5/2} \tag{4.5}$$

This four-body process takes advantage of the proximity of a FRET resonance

$$23p_{3/2} + 23p_{3/2} \leftrightarrow 23s + 24s \tag{4.6}$$

and a so-called quasi forbidden Förster resonance:

$$24s + 24s \leftrightarrow 23p_{1/2} + 23d_{5/2} \tag{4.7}$$

This last one would be forbidden by the dipole-dipole selection rules. In the next part of this chapter we will see how such a kind of energy transfer is possible in the presence of an external electric field. Despite the novelty of this four-body interaction, the interaction scheme presents some limitations. First of all the strength of the four-body coupling. The author finally detected a transfer of population to the $23d_{5/2}$ of 1 % that is small compared to the one observed for a two-body FRET. Moreover the process described by equation 4.5 is not generalizable to other principal quantum number n because this four-body process takes advantage of the accidental proximity of the two-body processes described by equations 4.6-4.7 which are so close only for this particular case. For these reason a more general transition scheme can be interesting. The initial target of this PhD thesis was the observation of a more general interaction

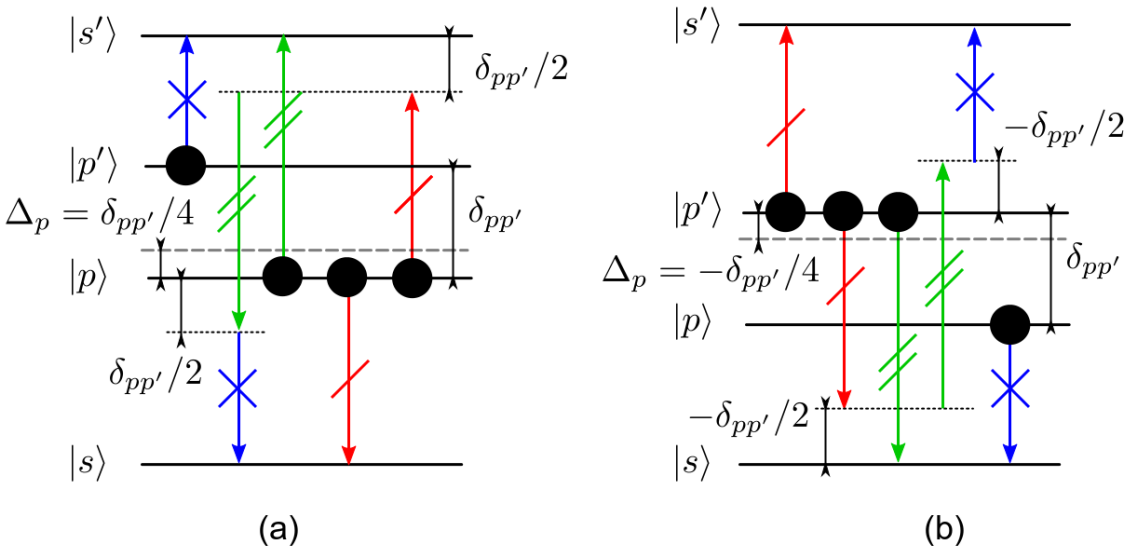

Figure 4.2: (a)-(b) Energy transfer scheme for the four-body interaction respectively described by equations 4.8-4.9. An horizontal dashed line is placed at the energy level $(E_s + E_{s'})/2$ and it represents the resonant condition for a two-body resonance. In both cases there is a first exchange of a virtual photon, symbolized with red arrows crossed with a single mark, that leads the system to a virtual intermediate state. A second virtual photon, symbolized with green arrows crossed with two marks, is then exchanged and drives the atoms in second virtual level. A third exchange of energy, denoted with the blue crossed lines, finally leads to the resonant end state.

scheme for a four-body FRET. The processes we proposed to study are described by the following reactions equations:

$$3 \times p + p' \leftrightarrow 2s + 2s' \tag{4.8}$$

$$p + 3 \times p' \leftrightarrow 2s + 2s' \tag{4.9}$$

where we have introduced a simpler notation in order to avoid a too heavy labelling for each Rydberg state and at the same time stress the universality of this new process. This notation will be useful also for the description of the three-body FRET we will see in the next chapter. The Cs Rydberg states $|ns_{1/2}\rangle$, $|(n+1)s_{1/2}\rangle$, $|np_{3/2}, |m_j| = 1/2\rangle$ and $|np_{3/2}, |m_j| = 3/2\rangle$ will be labelled with s, s', p and p' and E_s, $E_{s'}$, E_p and $E_{p'}$ are the respective energies that depend on the external electric field F. The two reactions described by equations 4.8-4.9 are respectively resonant at a Förster defect for a single atom of:

$$\Delta_p \equiv \frac{E_s + E_{s'} - 2E_p}{2} = \delta_{pp'}/4 \tag{4.10}$$

$$\Delta_{p'} \equiv \frac{E_s + E_{s'} - 2E_{p'}}{2} = -\delta_{pp'}/4 \tag{4.11}$$

where we remind the definition of $\delta_{pp'} = E_{p'} - E_p$.
In Fig. 4.2 we present a possible energy transfer scheme for both the processes. We suppose that two virtual levels, the ones marked with the dotted lines, are involved in such a kind of resonance processes. Despite the fact that we represent a sequence of three exchange of energy we assume that the transfer of population described by equations 4.8-4.9 occurs in a single step because they are too far from resonance.
In Fig. 4.3 we present a preliminary experimental measurement for the detection of the four-body resonance peaks. We plot the ratio of atoms transferred to $s+s'$ starting from an initial atomic sample excited at a p level (blue triangles), a p' (red circles) and a mixture of p and p' (black squares) for a principal quantum number $n = 31$. The three peaks emerging at $F = 8.85,\ 9.25,$ and 9.72 V cm^{-1} are due to the two-body FRET respectively described by equations 4.2, 4.4 and 4.3. The two four-body FRET peaks are instead predicted respectively at $F = 9.03$ and 9.45 V cm^{-1}. For these two values of the electric field we are supposed to observe a transfer peak for the black curve (the mixture of p and p'). We effectively observe a transfer at the predicted values but at the same time we observe a transfer peak for the blue curve which is due to the only excitation of a p. This transfer peak cannot be related to a four-body FRET neither to a two-body FRET. The presence of these unexpected peak complicate the detection of a four-body resonance.

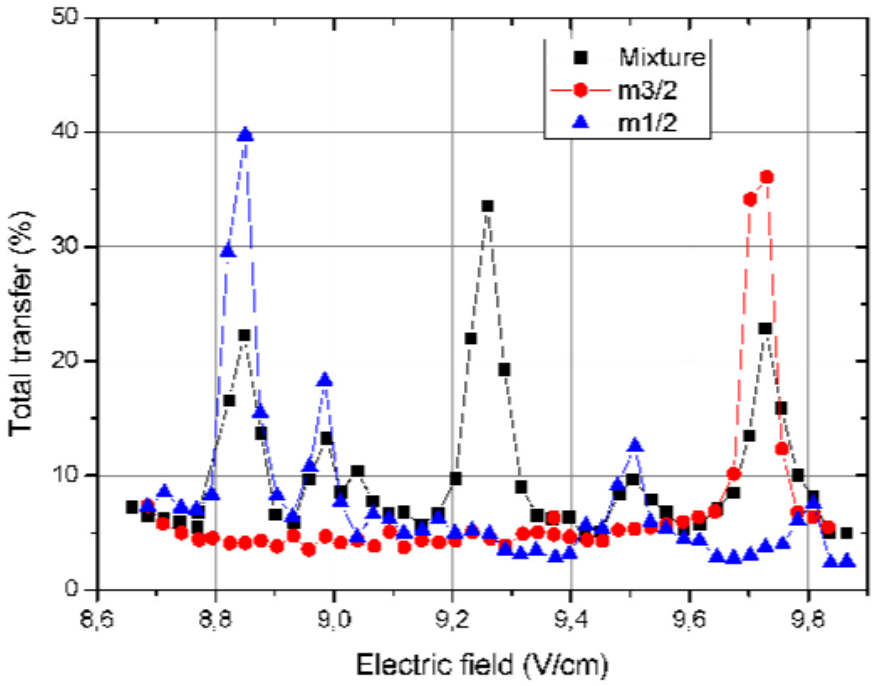

Figure 4.3: Averaged transfer ratio from the initial p state (a) or p' state (b) to $s + s'$ states for $n = 31$ versus the electric field.

4.2.2 Electric field coupling

We finally realize that the unexpected peaks we observe in Fig. 4.3 can be related to a so-called quasi-forbidden Förster resonance. We have already introduced a quasi-forbidden Förster resonance in equation 4.7. This kind of reaction is forbidden by the dipole selection rule $\Delta l = \pm 1$. The $23d_{5/2}$ state is not accessible from a $24s$ state with a single dipole transition. However in the presence of an external electric field, the Stark coupling can change the scenario. We have already seen in chapter 2 that an external electric field couples atomic state by the selection rule $\Delta l = \pm 1$. In this case the angular momentum is no longer a good quantum number and the orbital angular momentum is not well-defined. The Rydberg state excited with our experimental set up is thus a superposition of s, p, d etc... with a predominant p character. In this context the dipole selection rule $\Delta l = \pm 1$ is lifted. Instead, the states mixture opens the possibility of additional dipole-dipole coupling between the different Rydberg levels. We can search for new resonances allowed with the electric field tuning.
We thus decided to do a more systematic investigation of all the possible quasi-forbidden Förster resonances in the neighbourhood of a two-body FRET in order to probe the possibility of detecting the four-body peaks we initially proposed to observe.

4.2.3 Graphical solution

The study of the quasi-forbidden Förster resonances requires first of all to identify at which electric field a resonant dipole-dipole coupling can occurs. One set of quasi-forbidden resonances can be found considering the values of the quantum defect for different orbital angular momentum. In the case of Cs the quantum defect for an s state is $\delta_{ns} \sim 4$ while for an f state or even higher orbital quantum number the quantum defect is close to 0 [Goy et al., 1982]. The energy of ns and $(n-4)f$ Rydberg state are thus close as we can see in figure 4.4. We then expect that a change in the electric field around the previous resonance can lead to a non-negligible resonant dipole-dipole interaction between a two-atom state labelled with "np, np" and the two-atom state ns, $(n-3)f$ or $(n+1)s$, $(n-4)f$. For the next part of the thesis we continue using the label p for the Rydberg state excited with a three photon excitation even if we know that is not completely correct. We find for example that a quasi-forbidden resonance like:

$$2 \times |28p_{3/2}, |m_j| = 1/2\rangle \leftrightarrow |28s_{1/2}, |m_j| = 1/2\rangle + |25f_{7/2}, |m_j| = 1/2\rangle$$

reaches a dipole-dipole coupling of 24.5 MHz at 1 μm for an external electric field $F = 11.95$ V cm^{-1}, which is not negligible compared to dipole-dipole coupling of

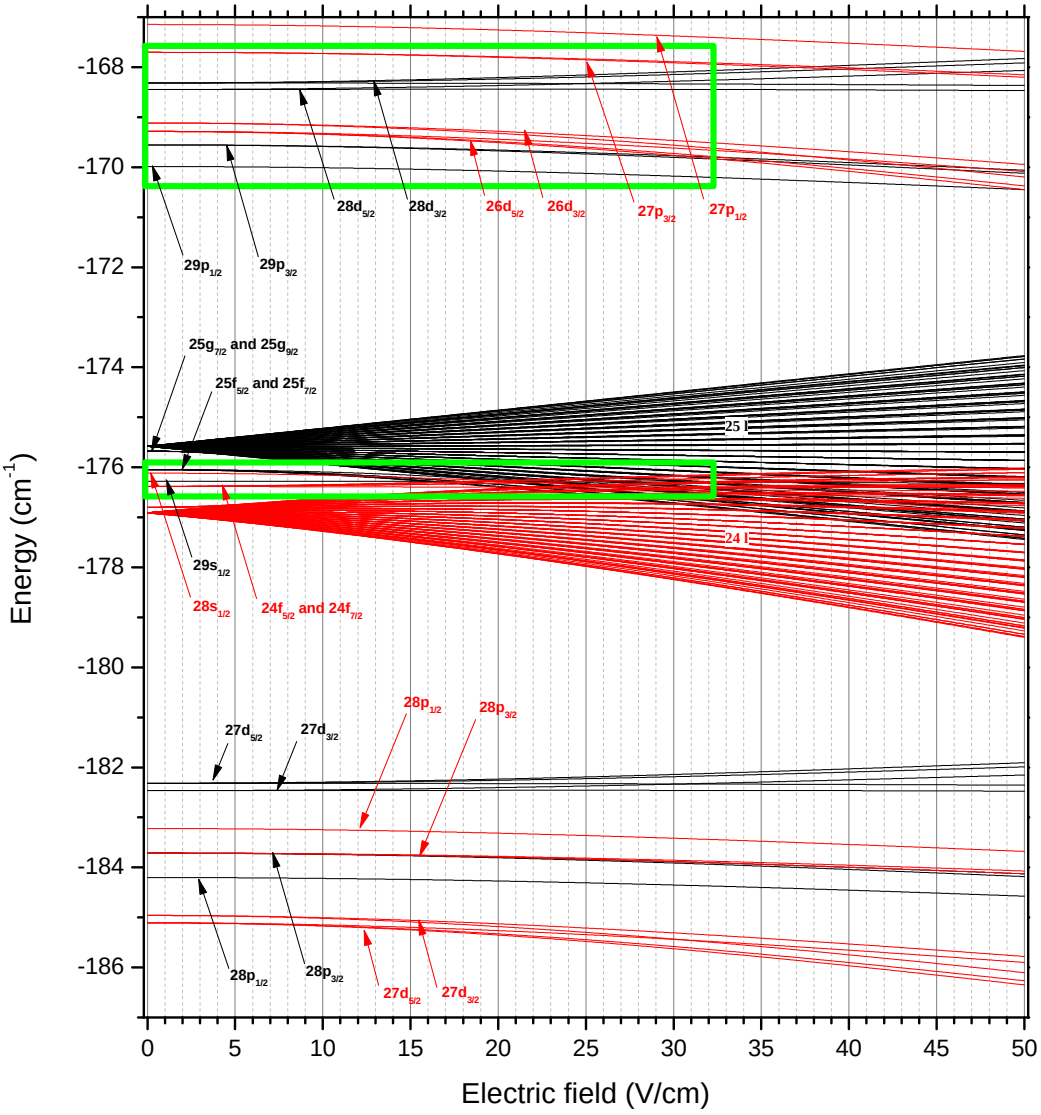

Figure 4.4: Resonance map. In black we plot the different Rydberg levels E'_r above the $|28p\rangle$ state, as a function of the applied external electric field F. In red, we plot the energy corresponding to $2 \times |28p_{3/2}, |m_j| = 3/2\rangle - E_{r''}$ to propose a graphical resolution of the resonance condition occurring in a Förster resonance. In green, we represent the zooms shown in Fig. 4.5 and Fig. 4.6.

175 MHz for a Förster allowed transition

$$2 \times |28p_{3/2}, |m_j| = 1/2\rangle \leftrightarrow |28s_{1/2}, |m_j| = 1/2\rangle + |29s_{1/2}, |m_j| = 1/2\rangle$$

at $F = 19.05$ V cm^{-1}. For the calculation we use a program in C language that has been developed here at Laboratoire Aimé Cotton. The aim of this program is to numerically calculate the radial part of the Rydberg wavefunction considering also the Stark effect. More details on this program can be found at the reference [Huillery, 2013].
As the number of Rydberg levels dramatically increases when we consider more and more orbitals, a graphical solution of the possible resonances is needed.
We consider a general two-body interaction $r + r \leftrightarrow r' + r''$. We know from the definition of the Förster defect that at resonance $\hbar\Delta_F = 2E_r - (E_{r'} + E_{r''}) = 0$. We rewrite this condition on the energy in the following way:

$$E_{r'} = 2 \times E_r - E_{r''}. \tag{4.12}$$

In Fig. 4.4, we present a graphical solution of the resonance condition occurring in a Förster resonance analogous to the one presented in [van Ditzhuijzen, 2009]. In red we plot the energy corresponding to $2 \times |28p_{3/2}, |m_j| = 3/2\rangle - E_{r''}$ that we label with the corresponding Rydberg state r'' while the black plot is the Stark map for different Rydberg levels. The resonance condition described by eq.4.12 is then fulfilled at the crossing of black red curves. We call the resulting plot resonance map.
The advantage of this graphical solution compared to the usual pair state energy plots [Li et al., 2005] lies in the simplicity to find quasi-forbidden resonances especially when a multiplicity is involved. Indeed when the energies of N states are calculated, for a pair state energy plot a priori N^2 curves are necessary to see all the resonances, while in our graphical method only 2N curves are required. The usual idea of the pair state energy plot is that a small number of resonances are present and only the authorized resonances are plotted.

4.2.4 Quasi-forbidden resonances prediction

We now want to discuss more in details the different two-body resonances we can predict with this new graphical method. We will consider the ones that at least conserve the dipole selection rule $\Delta l = \pm 1$ for one of the two atoms. For these quasi-forbidden resonances the efficiency of the transfer of atoms is supposed to be larger because even if the orbital angular momentum of the Rydberg state is not well defined, the p component of the Rydberg wave function is predominant in our excitation scheme. We thus identify two series of resonances where at least one of the

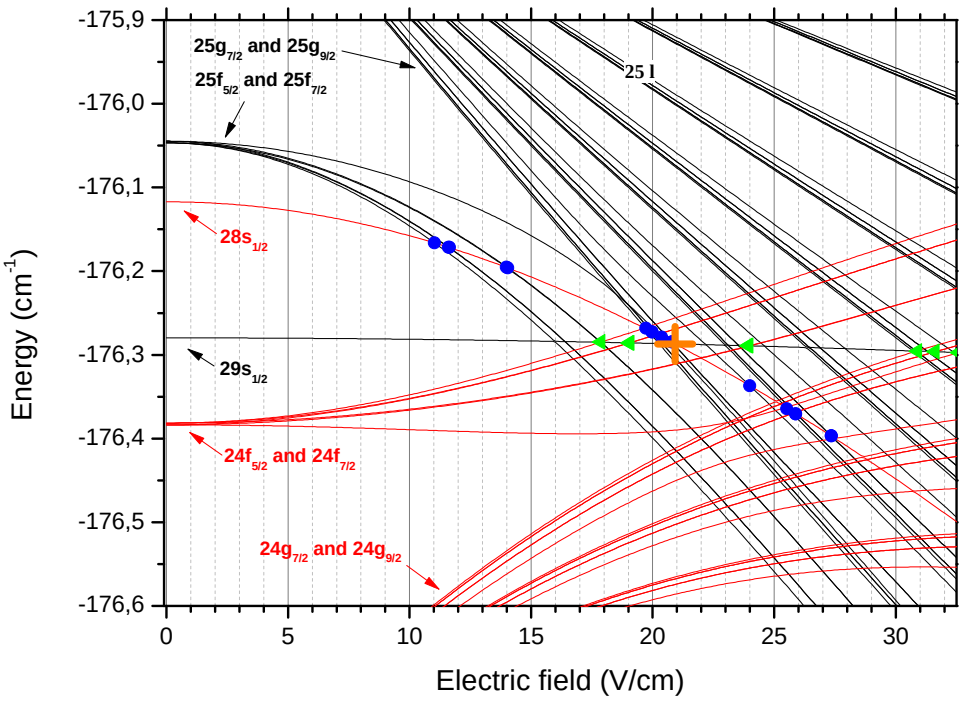

Figure 4.5: Resonance map in the vicinity of the $29s$ and $28s$ states. In black are plotted the eigenenergies $E_{r'}$ vs the applied external electric field F. In red, we plot the energy corresponding to $2 \times |28p_{3/2}, |m_j| = 3/2\rangle - E_{r''}$ to obtain a graphical solution of the resonance condition occurring in a Förster resonance. Here the thick orange cross indicates the allowed Förster resonance, the light green triangles and the blue circles show the multiple quasi-forbidden Förster resonances transferring atoms to the $29s$ and $28s$ states respectively. Only the absolute values of $|m_j|$ are plotted.

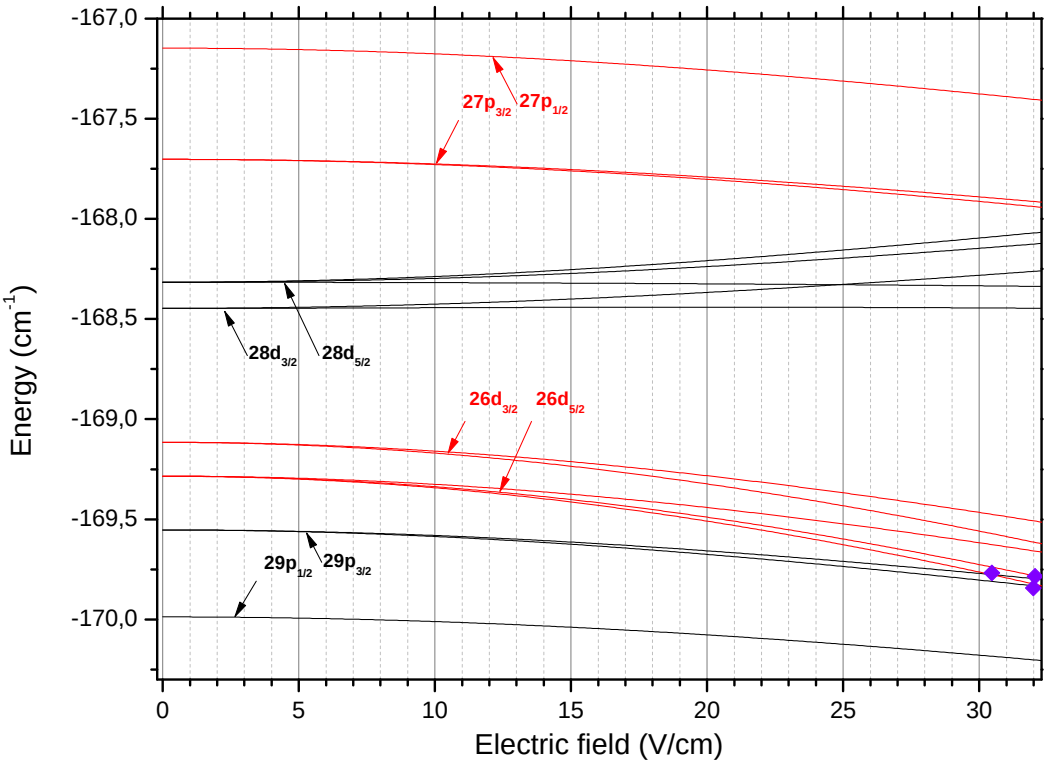

Figure 4.6: Resonance map for the $|28p_{3/2}, |m_j| = 3/2\rangle$ initial state in the vicinity of the $28d$ and $26d$ states. In black are plotted the eigen-energies $E_{r'}$ vs the applied external electric field F. In red, we plot the energy corresponding to $2 \times |28p_{3/2}, |m_j| = 3/2\rangle - E_{r''}$ to obtain a graphical solution of the resonance condition occurring in a Förster resonance. Here the purple squares show the few quasi-forbidden Förster resonances transferring atoms to the $29p$ and $26d$ states. Only the absolute values of $|m_j|$ are plotted.

atoms is transferred in an s or d state.
First we consider the case where at least one of the Rydberg state is an s state. In Fig. 4.5 we plot the zoom of the resonance map close to $r' = 29s$ and $r'' = 28s$. The orange cross at the crossing of the black curve for $29s_{1/2}$ and the red curve labelled $28s_{1/2}$ corresponds to the dipole-dipole allowed Förster resonance. The electric field at which we will observe a two-body Förster resonance is thus $F = 20.91$ V cm^{-1}. The light green triangles and the blue circles are placed at the crossing points at which the resonant condition is fulfilled.
An additional consideration on the projection of the total angular momentum m_j is necessary in order to evaluate the possibility of a dipole dipole coupling. Even if l is no more a good quantum number, the projection of the total angular momentum m_j is still a good quantum number since a uniform electric field only couples quantum state with the same value of m_j. So the dipole selection rule for $\Delta m_j = 0, \pm 1$ are still valid. We thus have to apply this selection rule when we consider the crossing of the red curve labelled $|28s_{1/2}\rangle$ with the black curve of the $25f_{7/2}$ state at $F = 11.03$, 11.6, 13.98, 20.37 V cm^{-1} for $|m_j| = 1/2,\ 3/2,\ 5/2,\ 7/2$ respectively (blue circles). This last one for $|m_j| = 7/2$ is forbidden. As we can see in Fig.4.5 the red curve $28s_{1/2}$ crosses many other Rydberg states. At each crossing point an analogous analysis is necessary to evaluate which resonance are really allowed. This analysis can be applied looking at the crossing of the $29s_{1/2}$ state curve with several red curves (green triangles).
We now consider the second series of resonances when one of the transferred atom is in d state. This is the situation described in Fig.4.6. The red curve labelled with $26d_{5/2}$ crosses the black curve corresponding to $|29p_{3/2}, |m_j| = 3/2\rangle$ (the upper state in the $29p_{3/2}$ manifold) at $F = 30.46, 32.05$ V cm^{-1}. The two crossings correspond to the $26d_{5/2}$ with $|m_j| = 1/2, 3/2$ respectively. Similarly the red labelled $|26d_{5/2}, |m_j| = 1/2\rangle$ curve crosses the $|29p_{3/2}, |m_j| = 1/2\rangle$ black curve at $F = 31.99$ V cm^{-1}.

4.2.5 Experimental observation of quasi-forbidden resonances

We now propose the discussion of the different series of quasi-forbidden resonances we have experimentally observed. We have investigated four different cases changing the initial state excited: $|28p_{3/2}, |m_j| = 1/2\rangle$, $|28p_{3/2}, |m_j| = 3/2\rangle$, $|32p_{3/2}, |m_j| = 1/2\rangle$ and $|32p_{3/2}, |m_j| = 3/2\rangle$. We originally choose to investigate these four states because for this values of the principle quantum number the implementation of the four-body experiment previously described was possible. Unfortunately we observed a variety of quasi-forbidden resonance peaks close to the expected values for a four-body peak.
We finally decided to classify all the quasi-forbidden peaks. The case of $n = 28$ is by itself a suitable example of how many different quasi-forbidden resonances have

to be taken into account in the neighborhood of a Förster resonance. The $n = 32$ is the last principle quantum number for which we observe quasi-forbidden resonances in the neighborhood of a Förster resonance. For higher principal quantum number quasi-forbidden resonances are far enough from the allowed Förster resonance so this case seems to be more favorable for the observation of a four-body interaction.
For completeness we say that we also studied the case of $n = 35$ for the investigation of a four-body interaction but in this case the two-body FRET transfer peaks were too large, because of the scaling n^4 of the dipole-dipole interaction and the distance between the peaks is too small to allow the study of the four-body interaction. We finally realize that the observation of a four-body resonance was not possible in the range of $n = 28 - 35$ because of the presence of the quasi-forbidden resonances and the broadening of the peaks.

Forbidden resonances from $|28p_{3/2}, |m_j| = 1/2\rangle$

The principal target of the analysis we have done is to classify all the possible quasi-forbidden resonance peaks we can observe in the proximity of a FRET peak. We do not precisely investigate the strength of each peak because the number of excited peaks is extremely large and our gate analysis is not suited for the study of so many different possible out-coming states.
In Fig.4.7 (a) we plot the percentage of the population of atoms analyzed as transferred in the $|28s_{1/2}, |m_j| = 1/2\rangle$ and $|29s_{1/2}, |m_j| = 1/2\rangle$ states from atoms prepared initially in the state $|28p_{3/2}, |m_j| = 1/2\rangle$ as a function of the external electric field. We also plot the percentage of atoms detected by the ions gate . In order to determine the baseline, we take a reference measurement at an electric field $F = 19.8$ V cm^{-1} where no Förster resonance is expected. We observe a residual baseline drift probably due to slowly varying ionization limit as a function of the Stark field. We first observe a peak for both states at $F = 19.05$ V cm^{-1} that corresponds to the allowed Förster resonance:

$$2 \times |28p_{3/2}, |m_j| = 1/2\rangle \leftrightarrow |28s_{1/2}, |m_j| = 1/2\rangle + |29s_{1/2}, |m_j| = 1/2\rangle. \tag{4.13}$$

We observe more than 25% of transfer for each state which corresponds to a total transfer of 50% if we consider the two-body states. This saturation effect is mostly due to the random distribution in distances between the Rydberg atoms that lead to a statistical average between pairs of atoms $|28p_{3/2}, |m_j| = 1/2\rangle + |28p_{3/2}, |m_j| = 1/2\rangle$ and $|28s_{1/2}, |m_j| = 1/2\rangle + |29s_{1/2}, |m_j| = 1/2\rangle$.
At $F = 18.3$ V cm^{-1} we observe another peak for both states $|28s_{1/2}, |m_j| = 1/2\rangle$ and $|29s_{1/2}, |m_j| = 1/2\rangle$. This peak cannot be explained by a two-body resonance since no

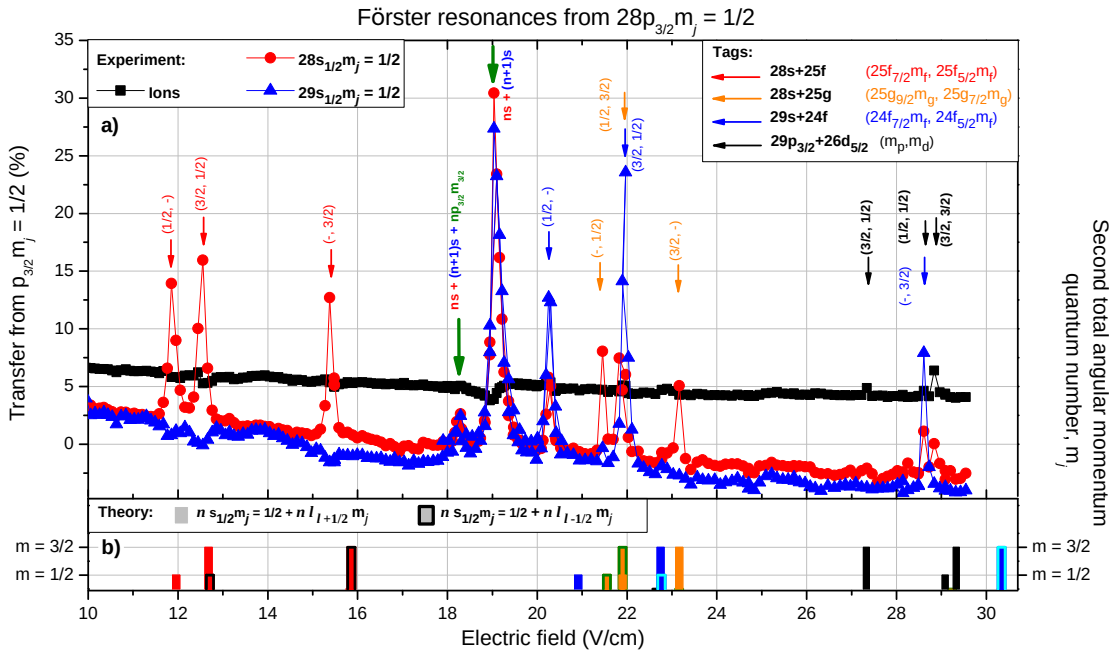

Figure 4.7: Quasi-forbidden Förster resonances around the allowed Förster resonance $2 \times 28p_{3/2}|m_j| = 1/2 \leftrightarrow 28s_{1/2}|m_j| = 1/2 + 29s_{1/2}|m_j| = 1/2$ located at $F = 19.05$ V cm^{-1}. In the upper part of the graph is shown the experimental measurement where all final states of the different resonances are tagged, while in the lower part the theoretical position prediction for those resonances are plotted. The resonance amplitudes in the lower part only reflect the projection of the total angular momentum quantum number m_j of the final state having $j > 1/2$. Moreover we distinguish the $l_{l+1/2}$ and $l_{l-1/2}$ final states with and without a frame around the bar representing the resonance. The data have been taken for an ionization delay of $\tau_{delay} = 2$ μs.

allowed Förster resonance nor quasi-forbidden resonances are expected at this electric field. In the next chapter we will explain that this peak is related to a three-body interaction that is a generalization of two-body Förster resonance.
The peaks of $|28s_{1/2}, |m_j| = 1/2\rangle$ transferred atoms can be explained by two possible series of two-body interaction described by the following equations:

$$2 \times |28p_{3/2}, |m_j| = 1/2\rangle \leftrightarrow |28s_{1/2}, |m_j| = 1/2\rangle + |25f_j, m'_j\rangle \tag{4.14}$$

$$2 \times |28p_{3/2}, |m_j| = 1/2\rangle \leftrightarrow |28s_{1/2}, |m_j| = 1/2\rangle + |25g_j, m'_j\rangle \tag{4.15}$$

where j can be equal to $7/2$ or $5/2$ for the f state because $j = l \pm 1/2$. For the same reason j is equal to $9/2$ or $7/2$ for the g state. We tag the peaks corresponding to the two-body resonances described by eqs.4.14-4.15 respectively with red and orange arrows. We indicate between the parenthesis the magnetic quantum number m'_j for the f or the g state. Because of the dipole selection rules $\Delta m_j = 0, \pm 1$ the absolute value of the magnetic quantum number can acquire two values $1/2$ and $3/2$, otherwise we have to consider interaction to higher order like quadrupole-quadrupole [Schwettmann et al., 2006, Stanojevic et al., 2008] or dipole-quadruple [Deiglmayr et al., 2014] where the selection rule admits transition even with $\Delta m_j = \pm 2$.
In Fig. 4.7 (b) the histograms indicate the different theoretical values of the electric field at which we predict the two-body resonances. The height of the histogram is related to the magnetic quantum number of the f, g or p state produced by the interaction. The histograms corresponding to $j = l - 1/2$ are marked with a frame while the filled histograms denote interactions that involve $j = l + 1/2$. The same color code is applied in Fig. 4.7(b) than in Fig. 4.7(a). In some cases we have an overlap between different possible transitions like in the case of the peak at $F = 12.7$ V cm^{-1} where we predict two different two-body resonances involving either the $|25f_{7/2}, |m_j| = 3/2\rangle$ state or the $|25f_{5/2}, |m_j| = 1/2\rangle$ state. The blue peaks related to the detection of the $|29s_{1/2}, m_j = 1/2\rangle$ are then described by the quasi-forbidden series:

$$2 \times |28p_{3/2}, |m_j| = 1/2\rangle \leftrightarrow |29s_{1/2}, |m_j| = 1/2\rangle + |24f_j, m'_j\rangle$$

with $j = 7/2$ or $j = 5/2$. These resonances are tagged with blue arrows. Using the graphical solution predicted in 4.2.3 we also predict a fourth series of quasi-forbidden resonances described by the following reaction:

$$2 \times |28p_{3/2}, |m_j| = 1/2\rangle \leftrightarrow |29p_{3/2}, m_j\rangle + |26d_{5/2}, m'_j\rangle \tag{4.16}$$

where the absolute value of the two magnetic quantum numbers m_j and m'_j can acquire the values $1/2$ and $3/2$. Observing the transfer induced by these resonances is harder

because the two product state cannot be well detected. The $26d_{5/2}$ is only partially ionized because the ionization ramp hardly achieves the ionization field for this level. On the other side the $29p_{3/2}$ is ionized at the very beginning of the ionization ramp and the signal arrives at a time corresponding to the ions gate. We thus observe an increase of the ions signal at an electric field resonant for the reaction of eq.4.16. The black arrows tag the three tiny peaks we observe for the ions gate signal.
Comparing the experimental and the theoretical values for the resonant electric field we observe a systematic overestimation of the calculated electric field which differs from a series to another. This aspect suggests us that the overestimation could be related to the precision of the quantum defect we use to calculate the Stark map for the graphical solution. Since we have many Rydberg levels with different quantum defects the overestimation can depend on the precision of each single quantum defect. However it is not obvious to find out which one biases the calculation of resonant electric field.
Additional consideration on the ions signal can give some more information about the nature of the dipole-dipole interaction. We observe a reduction of the ions signal on one side of the resonance while the other side presents an enhancement of the ion production. This variation of the ions signal can be explained considering the nature dipole-dipole interaction. For a couple of Rydberg atoms $|np, np\rangle$ with $n < 42$ the dipole-dipole interaction has a repulsive nature [Viteau et al., 2008]. So when we approach the resonant field of the main allowed resonance, the atoms repel each other. At this level the Penning collision, that are the principal cause of the ion signal, are less probable because of the repulsion between the interacting atoms. This effect, which is evident in the case of an allowed Förtser resonance, is present even for the other two-body resonances, but since the dipole-dipole coupling strength is smaller it is finally less evident. We can see a small dip for the resonances described by equations 4.14 at the lower electric field.

Forbidden resonances from $|28p_{3/2}, |m_j| = 3/2\rangle$

In Fig.4.8 we plot an analogous measurement for an ensemble of atoms prepared in the initial state $|28p_{3/2}, |m_j| = 3/2\rangle$. We just need to adapt the Ti:Sa laser frequency and turn the polarization by $\pi/2$ to optimize the excitation efficiency. We find most of the formerly described resonances shifted in the electric field as the $|m_j| = 3/2$ state is higher in energy and it requires a higher electric field to be Stark-shifted down to the resonances. Some additional peaks appear compared to the previous study because now even Rydberg state with $|m_j| = 5/2$ can be coupled by a dipole-dipole interaction.

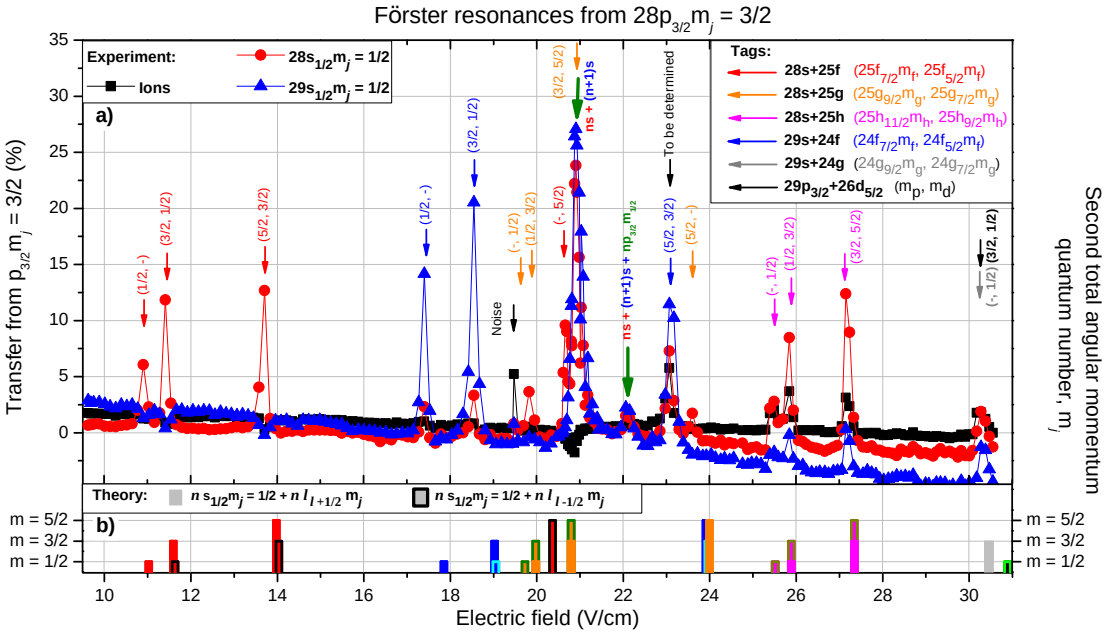

Figure 4.8: Quasi-forbidden Förster resonances around the allowed Förster resonance $2 \times |28p_{3/2}, |m_j| = 3/2\rangle \leftrightarrow |28s_{1/2}, |m_j| = 1/2\rangle + |29s_{1/2},, |m_j| = 1/2\rangle$ located at $F = 20.91$ V cm^{-1}. In the upper part of the graph is shown the experimental measurement where all final states of the different resonances are tagged, while in the lower part the theoretical position prediction of those resonances are plotted. See Fig. 4.7 for more details. The data have been taken for a ionization delay of $\tau_{delay} = 2$ μs.

We predict and observe the allowed Förster resonance described by:

$$2 \times |28p_{3/2}, |m_j| = 3/2\rangle \leftrightarrow |28s_{1/2}, |m_j| = 1/2\rangle + |29s_{1/2}, |m_j| = 1/2\rangle,$$

at $F = 20.91$ V cm^{-1}. We observe at $F = 22.05$ V cm^{-1} a peak due to a three-body interaction that we will describe more in detail in the next chapter. Among the formerly described quasi-forbidden Förster resonances, we observe an additional series of resonances described by the reaction:

$$2 \times |28p_{3/2}, |m_j| = 3/2\rangle \leftrightarrow |28s_{1/2}, |m_j| = 1/2\rangle + |25h_j, m_j'\rangle \tag{4.17}$$

where $j = 11/2$ or $j = 9/2$. The peaks corresponding to this series of interaction are tagged with a purple arrow in Fig.4.8 (a). For these peaks, that are characterized by the detection of Rydberg atoms in $|28s_{1/2}, |m_j| = 1/2\rangle$ we also observe a non negligible signal for the ions and the $|29s_{1/2}, |m_j| = 1/2\rangle$ state that can be due to the detection of $25h_j$ which have an energy level close to the $29s_{1/2}m_j = 1/2$.
We also observe an additional quasi-forbidden resonances for the $|29s_{1/2}, |m_j| = 1/2\rangle$ described by the reaction:

$$2 \times |28p_{3/2}, |m_j| = 3/2\rangle \leftrightarrow |29s_{1/2}, |m_j| = 1/2\rangle + |24g_{7/2}, |m_j| = 1/2\rangle$$

that is tagged with a grey arrow in Fig. 4.8 (a).
In Fig. 4.8 we also observe two different peaks that are not totally understood. The first one is a peak of the ions signal at $F = 19.4$ V cm^{-1} where no resonances are expected. Indeed on other measurement this peak does not appear. The fact that we observe this anomalous ions signal only for one value of the electric field lets us interpret this point as a noisy measurement.
The second peak that is not totally clear is the one observed at $F = 23.1$ V cm^{-1}. At this value of the electric field we observe a transfer to the $|29s_{1/2}, |m_j| = 1/2\rangle$ that can be well explained by the two quasi-forbidden resonances:

$$2 \times |28p_{3/2}, |m_j| = 3/2\rangle \leftrightarrow |29s_{1/2}, |m_j| = 1/2\rangle + |24f_{7/2}, |m_j| = 5/2\rangle \tag{4.18}$$
$$2 \times |28p_{3/2}, |m_j| = 3/2\rangle \leftrightarrow |29s_{1/2}, |m_j| = 1/2\rangle + |24f_{5/2}, |m_j| = 3/2\rangle, \tag{4.19}$$

but we further observe a non negligible signal for the ions gate and the $|28s_{1/2}, |m_j| = 1/2\rangle$ that we cannot explain with one of the series we previously proposed. A possible explanation might be the presence of an additional quasi-forbidden resonance described by:

$$2 \times |28p_{3/2}, |m_j| = 3/2\rangle \leftrightarrow |27f_{7/2}, |m_j| = 1/2\rangle + |25d_{5/2}, |m_j| = 3/2\rangle \tag{4.20}$$

The direct demonstration of this kind of resonance is not so easy in our experimental set up because we are not able to obtain a reference signal for $|27f_{7/2}, |m_j| = 1/2\rangle$ which is not excited from the $|7s\rangle$ state. Moreover the superposition with the resonances described by eqs. 4.18-4.19 add additional noise to the detection of the resonance described by eq. 4.20.
Otherwise looking at the time of flight signal profile we can do some consideration that justify our assumption. In Fig.4.9 we plot the TOF signal for the reference curve taken for the $|28p_{3/2}, |m_j| = 3/2\rangle$ at a non resonant field $F = 19.8$ V cm^{-1} (red profile) and the detected signal at $F = 23.1$ V cm^{-1} (green profile). We can see the presence of transferred atoms due to Förster resonance: in the $28s_{1/2}$ gate we observe an increased signal respect to the reference one. This signal should correspond to the 24 f state. We can see that in this gate the signal is spread and it does not go to zero at the end of the acquisition time window. This spread is probably due to a partial ionization of $24f$ but could also contain ionization from another low energy state like $|25d_{5/2}, |m_j| = 3/2\rangle$. But on the high energy part of the TOF, we clearly see both signals in the $29s$ gate and in the ions gate. This signal could be related to an higher Rydberg level like $|27f_{7/2}, |m_j| = 1/2\rangle$.

Forbidden resonances from $|32p_{3/2}, |m_j| = 1/2\rangle$ & $|32p_{3/2}, |m_j| = 3/2\rangle$

We now want to examine the two cases of quasi-forbidden resonances observed from an initial Rydberg state labelled with $|32p_{3/2}, |m_j| = 1/2\rangle$ and $|32p_{3/2}, |m_j| = 3/2\rangle$. As we have mentioned before in these two cases we observe less quasi-forbidden peaks with respect to the previous case on $28p$ because the quasi-forbidden resonances are then expected further apart from the allowed resonance. The resonant field for quasi-forbidden resonances of the kind $p + p \leftrightarrow s + f$ or $p + p \leftrightarrow s + g$ changes slowly. For increasing principal quantum number, the resonant field decreases due to a stronger Stark effect. But it decreases slower than the resonant field for the allowed resonance which tends to zero field at n=42 where the Frster defect changes sign. Starting from $n = 33$ these resonances are at bigger electric field. On the other side the resonances $p+p \leftrightarrow p+d$ change their position from a principal quantum number to another very fast and appear at a smaller electric field with respect to the allowed Förster resonance starting from $n = 31$.
Turning back to $n = 32$, the allowed Förster resonances involved are described by:

$$2 \times |32p_{3/2}, |m_j| = 1/2\rangle \leftrightarrow |32s_{1/2}, |m_j| = 1/2\rangle + |33s_{1/2}, |m_j| = 1/2\rangle$$
$$2 \times |32p_{3/2}, |m_j| = 3/2\rangle \leftrightarrow |32s_{1/2}, |m_j| = 1/2\rangle + |33s_{1/2}, |m_j| = 1/2\rangle.$$

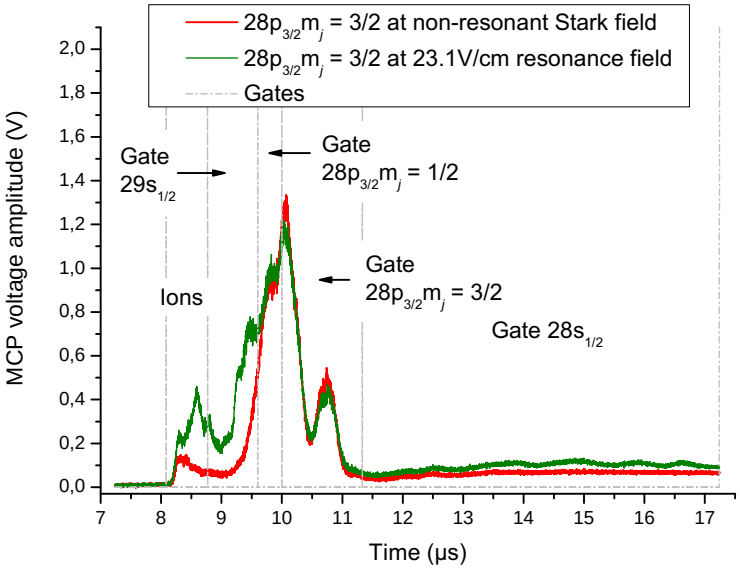

Figure 4.9: Time-of-flight (TOF) from selective field ionization to detect the $np_{3/2}$, $ns_{1/2}$ and $(n+1)s$ signals where only the np states has been excited at a quasi-forbidden resonant electric field $F = 23.1$ V/cm (in green). We compare it to the reference signal (in red) shown on Fig. 3.10.

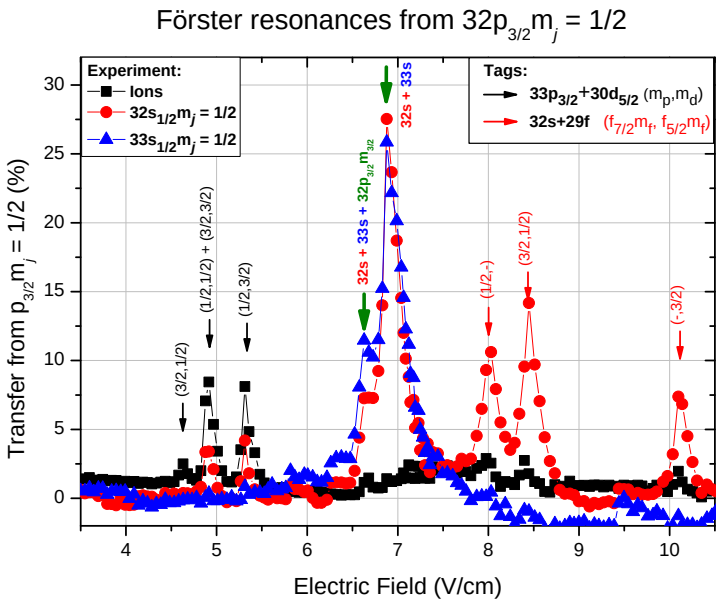

Figure 4.10: Quasi-forbidden Förster resonances around the allowed Förster resonance $2 \times |32p_{3/2}, |m_j| = 1/2\rangle \leftrightarrow |32s_{1/2}, |m_j| = 1/2 + |33s_{1/2}, |m_j| = 1/2\rangle$ located at $F = 6.89$ V cm^{-1}. Here is shown the experimental measurement where all final states of the different resonances are tagged. The data have been taken for an ionization delay of $\tau_{delay} = 2$ μs.

On Fig. 4.10 and Fig. 4.11 we respectively plot the signals detected by the ions gate (black square), the $|32s_{1/2}, |m_j| = 1/2\rangle$ gate (red circle) and $|33s_{1/2}, |m_j| = 1/2\rangle$ (blue triangle). We tag with a green arrow the two-body FRET resonance expected and observed respectively at $F = 6.89$ V cm^{-1} and $F = 7.56$ V cm^{-1} and the three-body processes described by:

$$3 \times |32p_{3/2}, |m_j| = 1/2\rangle \leftrightarrow |32s_{1/2}, |m_j| = 1/2\rangle + |33s_{1/2}, |m_j| = 1/2\rangle + |32p_{3/2}, m_j\rangle = 3/2\rangle$$
$$3 \times |32p_{3/2}|m_j| = 3/2\rangle \leftrightarrow |32s_{1/2}, |m_j| = 1/2\rangle + |33s_{1/2}, |m_j| = 1/2\rangle + |32p_{3/2}, |m_j| = 1/2\rangle$$

and observed respectively at $F = 6.65$ V/ cm^{-1} and $F = 8.06$ V cm^{-1}. These three-body processes are analogous to the one we have already observed for $n = 28$. It is a general process due to a second perturbative order dipole-dipole coupling. We will discuss into more details this new process in the next chapter. For now we will concentrate more on the quasi-forbidden resonances.
We observed two series of quasi-forbidden resonances. The first is described by the following equations:

$$2 \times |32p_{3/2}, |m_j| = 1/2\rangle \leftrightarrow |33p_{3/2}, m'_j\rangle + |30d_{5/2}, m''_j\rangle \quad (4.21)$$
$$2 \times |32p_{3/2}, |m_j| = 3/2\rangle \leftrightarrow |33p_{3/2}, m'_j\rangle + |30d_{5/2}, m''_j\rangle \quad (4.22)$$

and tagged with black arrows in both Figs. 4.10 and 4.11. The different possible combination of magnetic quantum number for the final state are stated between parenthesis. In the case the initial state in equation 4.21 is $|32p_{3/2}, |m_j| = 1/2\rangle$ $|m'_j|$ and $|m''_j|$ take the values 1/2 and 3/2 while in the case of equation 4.22 they can also take the value 5/2.
The second series is described by the equation:

$$2 \times |32p_{3/2}, |m_j| = 1/2\rangle \leftrightarrow |32s_{1/2}, |m_j| = 1/2\rangle + |29f_{j'}, m_{j'}\rangle \quad (4.23)$$
$$2 \times |32p_{3/2}, |m_j| = 3/2\rangle \leftrightarrow |32s_{1/2}, |m_j| = 1/2\rangle + |29f_{j'}, m_{j'}\rangle \quad (4.24)$$

where j' can take the values 7/2 and 5/2. These resonances are tagged with a red arrow in both Figs. 4.10, 4.11. In this case the $|m_{j'}|$ can take the values 1/2 and 3/2 if the starting state is $|32p_{3/2}|m_j| = 1/2\rangle$ and 5/2 if the initial state is instead $|32p_{3/2}, |m_j| = 3/2\rangle$.

4.3 Conclusion

We have seen that in the vicinity of the allowed 2-body Förster resonance many quasi-forbidden 2-body Förster resonances are also present. The identified forbidden res-

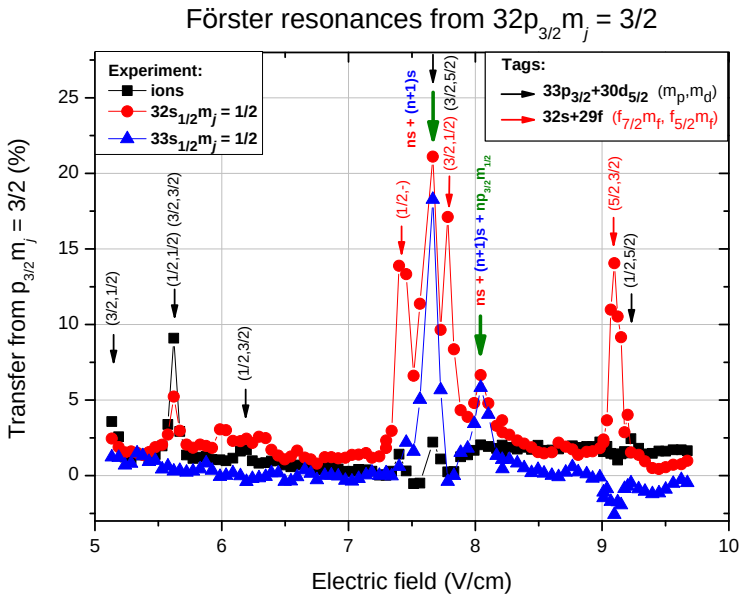

Figure 4.11: Quasi-forbidden Förster resonances around the allowed Förster resonance $2 \times |32p_{3/2}, |m_j| = 3/2\rangle \leftrightarrow |32s_{1/2}, |m_j| = 1/2\rangle + |33s_{1/2}, |m_j| = 1/2\rangle$ located at $F = 7.56$ V cm^{-1}. Here is shown the experimental measurement where all final states of the different resonances are tagged. The data have been taken for an ionization delay of $\tau_{delay} = 3$ μs.

onances are no longer close in electric field from the allowed resonance for n larger than 32. They show an estimated total transfer up to $\approx 30\%$, compared with the total transfer of 50% for the allowed resonances. In presence of a low electric field, dipole-dipole coupling in those quasi-forbidden Förster resonances allow population transfer with a change in the orbital quantum number from a "labelled" p-state up to a "labelled" h-state or allow transfer involving no change of the l-state between the initial and final states. We can assume that at higher fields $\Delta l > 4$ resonances due to l-mixing would appear as presented in [Kachru et al., 1983, Renn et al., 1994]. We have also proposed a graphical resolution of the resonance condition of Förster resonances, allowing to identify clearly the position of the different quasi-forbidden Förster resonances.

Those quasi-forbidden 2-body Förster resonances could be of interest in the case of potential processes requiring tunable interactions over a broad band of electric field, like in the search for few-body interactions or to realize macro-molecules built from Rydberg atoms. Indeed, they increase dramatically the number of addressable resonant energy transfers in the Cs atom with an efficiency of the order of the well-known allowed resonances.They also allow to excite Rydberg state with higher orbital angular momentum l which are hard to reach with the common excitation scheme. As we have already said in paragraph 4.2.1, a quasi-forbidden a resonance can facilitate cascade processes like the one described in [Gurian et al., 2012].

The investigation of quasi-forbidden resonance is also necessary in order to classify the different transfer peaks we observe. As we have already introduce, a transfer of atoms due to a new three-body interaction has been observed next to the allowed two-body resonance. A scrupulous analysis of the different transfer peaks has been realized in order to exclude that this peak can be related to any kind of quasi-forbidden resonance. Moreover transfer of atoms due to dipole-quadrupole interaction as the one observed in [Deiglmayr et al., 2014] have been predicted in the proximity of a Förster resonance. The Rydberg state coupled by a dipole-quadrupole interaction can be excited even by a quasi forbidden Förster resonance. In this context the classification of quasi-forbidden resonances in order to exclude any effect due to a quasi forbidden resonance is necessary.

The presence of a quasi-forbidden Förster resonance can also have non-negligible effect in the calculation of interaction strength even for non-resonant interaction. For that reason a careful analysis of all the possible dipole-dipole coupling is necessary when we want to calculate a non resonant interaction between two Rydberg atoms when an electric field is applied.

5 Borromean three-body FRET

5.1 A new resonant interaction

In paragraph 4.2.5 we have observed, in between the different quasi-forbidden resonance peaks, the appearance of an unexpected peak for the four experimental cases: $|28\ p_{3/2}, |m_j| = 1/2\rangle$, $|28\ p_{3/2}, |m_j| = 3/2\rangle$, $|32\ p_{3/2}, |m_j| = 1/2\rangle$ and $|32\ p_{3/2}, |m_j| = 1/2\rangle$. The unexpected peak appears at smaller electric fields for the $|28\ p_{3/2}, |m_j| = 1/2\rangle$ and $|32\ p_{3/2}, |m_j| = 1/2\rangle$ allowed Förster resonances. In Figs. 4.7-4.10 we tag this peak with a green arrow. For the other two cases examined $|28\ p_{3/2}, |m_j| = 3/2\rangle$ and $|32\ p_{3/2}, |m_j| = 3/2\rangle$ the unexpected peak appears at a larger electric field for the Förtser resonance (see the green arrow in Figs. 4.8-4.11). In all the 4 cases we observe an equal transfer of atoms to ns and $(n+1)s$ in analogy with dipole-dipole allowed resonance. However we have not found any kind of quasi-forbidden resonance at the corresponding electric field which could explain this transfer of atoms. Moreover comparing the results between $n = 28$ and $n = 32$ we can see an increase of the transfer peak at the increasing of the principal quantum number. In both cases these transfer peaks seem to appear at an electric field correlated to the one at which we observe the Förster resonance in contrast with the quasi-forbidden resonance peaks. Quasi-forbidden Förster resonances are uncorrelated from the position of principal two-body Förster resonance because the Rydberg state involved are not necessarily the same and thus the avoided crossing between the resonant two-atom states occur at independent positions.
All these characteristics suggested us to look for a more general process at the origin of these transfer peaks. For the explanation of these unexpected peaks we thus elaborate a new three-body process that is a generalization of a two-body Förster resonance. Because of its evident analogy with the two-body Förster resonance also known as FRET we will extend this appellation also to the new three-body interaction.
In this chapter we will give an interpretation of this new process providing an exhaustive experimental characterization, proposing a generalization to an n-body process. We will finally conclude with possible application of three-body processes in quantum computing and quantum information.

5.1.1 Borromean interaction

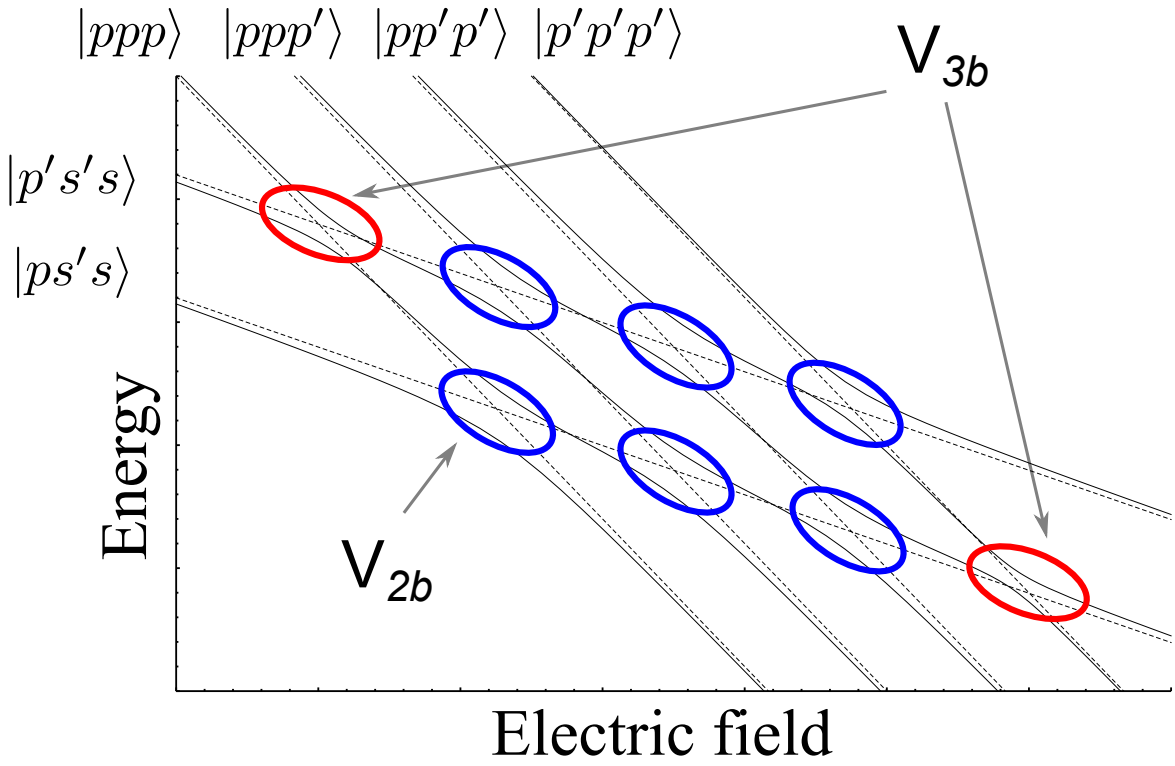

Figure 5.1: Schematic Stark map of the different 3-atom states energies as a function of the external electric field. The blue ellipses correspond to the avoided crossing of 2-body Förster resonances while the red ones tag the avoided crossing expected for the new three-body processes.

Before starting to describe the three-body process we remind here the notation we introduced in paragraph 4.2.1. For the next part of the thesis we will label the Cs Rydberg states $|ns_{1/2}\rangle$, $|(n+1)s_{1/2}\rangle$, $|np_{3/2}, |m_j| = 1/2\rangle$ and $|np_{3/2}, |m_j| = 3/2\rangle$ with s, s', p, and p' respectively. We label the respective energies with E_s, $E_{s'}$, E_p and $E_{p'}$ that depend on the external electric field F. This simpler notation allows to avoid a too heavy label for each Rydberg state and at the same time stresses the universality of the new observed process.
In Fig. 5.1 we schematically present the energy level of all the possible three-atom states we can obtain from the combination of p and p' states. We approximate the Stark shift with a linear one because we consider the variation from the quadratic shift

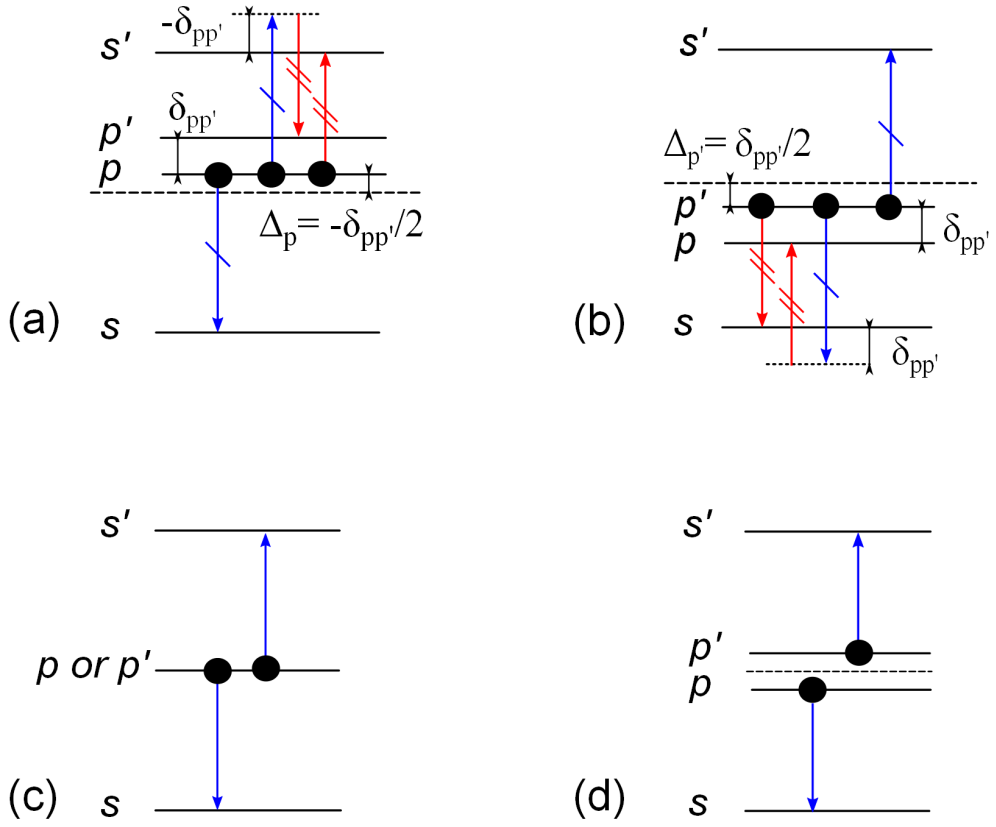

Figure 5.2: Energy transfer scheme of 2 and 3-body interaction. (a)-(b) Energy transfer scheme for the three-body interaction described by respectively by equations 5.1-5.2. The horizontal dashed line is placed at the energy level $(E_s + E_{s'})/2$ and it represents the resonant condition for a two-body resonance. In both cases there is a first exchange of a virtual photon, symbolized with blue arrows crossed with a single mark, that leads the system to a virtual intermediate state. A second virtual photon, symbolized with red arrows crossed with two marks, is then exchanged and it finally leads to the resonant end state. (c)-(d) Energy transfer scheme for the two-body interaction described by respectively by equations 4.2-4.3 and 4.4.

is negligible as we can see from the Stark map of Cs calculated in [Gurian et al., 2012, Huillery, 2013]. We additionally plot the three-atom states $|p's's\rangle$ and $|ps's\rangle$. Since the slope of Stark shift of s and s' is much smaller compared to the one of p and p' the energy levels of $|p's's\rangle$ and $|ps's\rangle$ will cross the three-atom state composed by p and p'. In Fig.5.1 we see eight crossings marked with red and blue ellipses. The blue ellipses are placed at the avoided crossings we expect for a two-body resonance. In this case one of the three atoms in p or p' does not play a role in the interaction. The 6 avoided crossings thus correspond two-by-two respectively to the two-body Förster resonances described by equations 4.24.4 we have previously introduced in paragraph 4.1. In these cases two of the three atoms interact and one is left in its initial state.
The two remaining crossings denoted with red ellipses require a deeper analysis. We cannot describe this coupling with a two-body interaction because in both cases the third atom moves to another Zeeman sub-level. We thus propose to consider this coupling between the two three-atom states due to a three-body interaction. We can generalize equations for a FRET to the case of a three-atom interaction:

$$3 \times p \leftrightarrow s + s' + p' \tag{5.1}$$

$$3 \times p' \leftrightarrow s + s' + p. \tag{5.2}$$

We know from the definition of a Förster resonance we gave in chapter 2 that the dipole-dipole coupling is maximum when the two two-atom states are resonant which corresponds to a Förster defect Δ_F equal to zero.In analogy with Förster resonance the coupling between the three-atom states would be maximum when the initial and final states have the same energy. From the definition of Förster defect for a single atom $\Delta_p \equiv \frac{E_s+E_{s'}}{2} - E_p$ and $\Delta_{p'} \equiv \frac{E_s+E_{s'}}{2} - E_{p'}$, we obtain that the three-atom states of equation 5.1 and 5.2 are resonant respectively for $\Delta_p = -\delta_{pp'}/2$ and $\Delta_{p'} = \delta_{pp'}/2$ where $\delta_{pp'} = E_{p'} - E_p$ is the energy splitting between p and p'.
The three-body interaction $|ppp\rangle \rightarrow |ss'p'\rangle$ cannot be described with the exchange of a single virtual photon. We can imagine that the transition takes place by the help of a virtual state we denote $|ss'^*p\rangle$. The sequence is the following:

$$|ppp\rangle \rightarrow |ss'^*p\rangle \rightarrow |sp's'\rangle.$$

In Fig. 5.2(a)-(b) we report the energy transfer scheme for the three-body interactions respectively for p and p'. In both cases a dashed line is traced at an energy level corresponding to $(E_s + E_{s'})/2$. In the first case we can imagine that one of the three atoms in a p state acts as a relay. In the scheme we present, this role is played by the atom in the middle: a first exchange of energy, denoted by the blue arrows with single mark, is due to a dipole-dipole coupling we label with $V_{dip1} \propto \frac{\vec{\mu}_{ps} \cdot \vec{\mu}_{ps'}}{R^3}$ where

$\vec{\mu}_{rr'}$ is the matrix dipole element for the dipole transition $r \to r'$. This coupling drives the transition $|ppp\rangle \to |ss'^*p\rangle$. The three-body state $|ss'^*p\rangle$ is a virtual state detuned $2\Delta_p = -\delta_{pp'}$ from the real one $|ss'p\rangle$. At this electric field, the transfer ratio is strongly depressed because the interaction is out of resonance. We do not expect any two-body resonant energy transfer. A second exchange of energy, now denoted with a double marked red arrows, is due to a dipole coupling $V_{dip2} \propto \frac{\vec{\mu}_{s'p'} \cdot \vec{\mu}_{ps'}}{R^3}$ and it drives the transition $|ss'^*p\rangle \to |sp's'\rangle$. The interaction Hamiltonian in the three-atom state basis $|ppp\rangle,\ |ss'^*p\rangle,\ |sp's'\rangle$ is:

$$H_{3b} = \frac{1}{2} \begin{pmatrix} 0 & V_{dip1} & 0 \\ V_{dip1} & 2\Delta_p & V_{dip2} \\ 0 & V_{dip2} & 0 \end{pmatrix} \tag{5.3}$$

where we have set the energy of the two resonant states $|ppp\rangle,\ |sp's'\rangle$ equal to zero. In the hypothesis $|\Delta_p| \gg V_{dip1},\ V_{dip2}$ the population of $|ss'^*p\rangle$ is strongly suppressed and we can proceed to the adiabatic elimination of this level. The system simply reduces to a two-level system $|ppp\rangle$ and $|sp's'\rangle$ coupled by an interaction term we call V_{3b}. In analogy with adiabatic elimination theory [Shore, 1990, Torosov and Vitanov, 2012] we obtain:

$$H_{3b}^{ad} = \frac{1}{2} \begin{pmatrix} -\frac{V_{dip1}^2}{2\Delta_p} & -V_{3b} \\ -V_{3b} & -\frac{V_{dip2}^2}{2\Delta_p} \end{pmatrix} \tag{5.4}$$

where we have introduced the three-body coupling:

$$V_{3b} = \frac{V_{dip1} V_{dip2}}{2\Delta_p} \tag{5.5}$$

Even if we use a virtual level for the description of resonant energy transfer, the transition occurs in a single step because we can neglect the population of the virtual level which is largely detuned compared to the resonant one. This three-body interaction has thus a "Borromean" character since the two-body coupling is negligible to the three-body one: a tern of atoms can interact while a couple cannot. This kind of interaction find thus an analogy with the trimer Efimov state [Kraemer et al., 2006, Pollack et al., 2009] and predicted Borromean interaction in Rydberg atoms [Kiffner et al., 2013].
An alternative interpretation of this three-body interaction is to consider it as two-body assisted resonance. In this interpretation we consider that the atom which acts as a relay absorbs the energy detuning of the virtual level changing its Zeeman sublevel. This relay atom allows thus a two-body transfer $|pp\rangle \to |ss'\rangle$ at an electric field

where the dipole-dipole coupling is suppressed. However we still require to consider a virtual level for the energy transfer and we always have a net three particle interaction to consider.
We have examined the case of three atoms in p state, but the same considerations are valid even for the case of three atoms in p'. We just need to adjust the Förster defect $\Delta_{p'} = \delta_{pp'}/2$ and consider a slightly different energy transfer scheme which is resumed in Fig. 5.2(b). Even for p' state we can write an analogous formula for the three-body coupling.
Using the scaling properties introduced in chapter 2, we can estimate the scaling of V_{3b}. V_{dip1}, $V_{dip2} \propto n^4/R^3$ so we immediately obtain $V_{3b} \propto n^8/R_1^3 R_2^3$ where we consider the general case of two different distances R_1 and R_2 between the relay and the other two atoms. The spatial configuration of the tern of atoms thus plays an important role in determining the strength of the coupling. Moreover the spatial orientation of the three atoms strongly influences the strength of the single dipole-dipole coupling V_{dip1} , V_{dip2} and consequently the three-body coupling. Unfortunately our experimental set up cannot allow us to excite Rydberg atoms at a fixed geometry so we have not investigated in much detail the dependence of the coupling as a function of the geometry. For all the estimation we have done of the three-body coupling we have considered three atoms arranged in an equilateral triangle with a distance equal to the mean calculated distance between atoms. This assumption seems to be a reasonable approximation because it is the most favorable configuration for a three-body interaction. In our experimental set up we estimate to excite Rydberg atoms at a mean distance of 3 μm.

5.2 Experimental characterization

In the following paragraph we present the experimental characterization of the new three-body processes. We will propose the study of the population transfer from the initial Rydberg state p or p' to the s and s' states as a function of the external electric field. After that we present a characterization of the number of transferred atoms as a function of the initial density. This kind of measurement finally shows a cubic dependence of the number of transferred atoms which is characteristic of a three-body interaction.

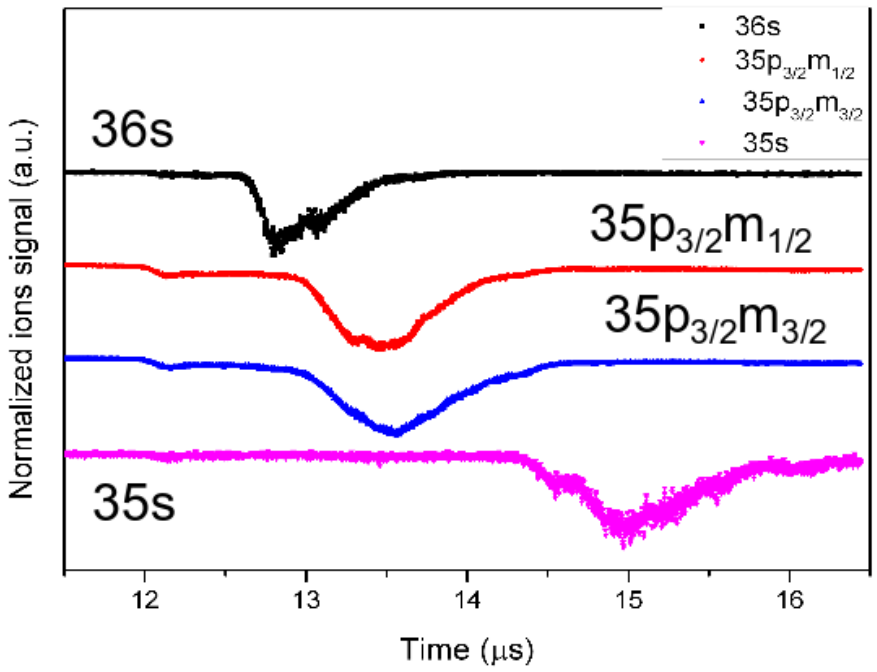

Figure 5.3: Reference Time-of-Flight signal taken for $|35s\rangle$, $|36s\rangle$, $|35p_{3/2}, |m_j| = 1/2\rangle$ and $|35p_{3/2}, |m_j| = 3/2\rangle$. Each signal has been taken at the reference field $F = 2.70 V cm^{-1}$.

5.2.1 Two & three-body resonance peaks

We now present the study of the two and three-body transfer peaks for different principal quantum number $n = 28,\ 32,\ 35$. The experimental protocol is the same described in chapter 3 and used for the detection of the quasi-forbidden resonances described in chapter 4. We study both the three-body resonances described by equations 5.1-5.2. In the first case we plot the ratio of atoms transferred to $s + s'$ starting from an initial atomic sample excited at a p level. We chose to plot the ratio of $s + s'$ instead of $s + s' + p'$ because as we can see in Fig.5.3 the signal corresponding to p and p' are mostly overlapped and the residual cross-talk after correction are still on the order of $\pm 5\%$ or more between them. This choice does not affect the observation of the transferred peak even if the detection of p' will be a more direct demonstration of the three-body process. In the case of equation 5.2 we just have to inverse the role of p and p' but the considerations we have already done are still valid.

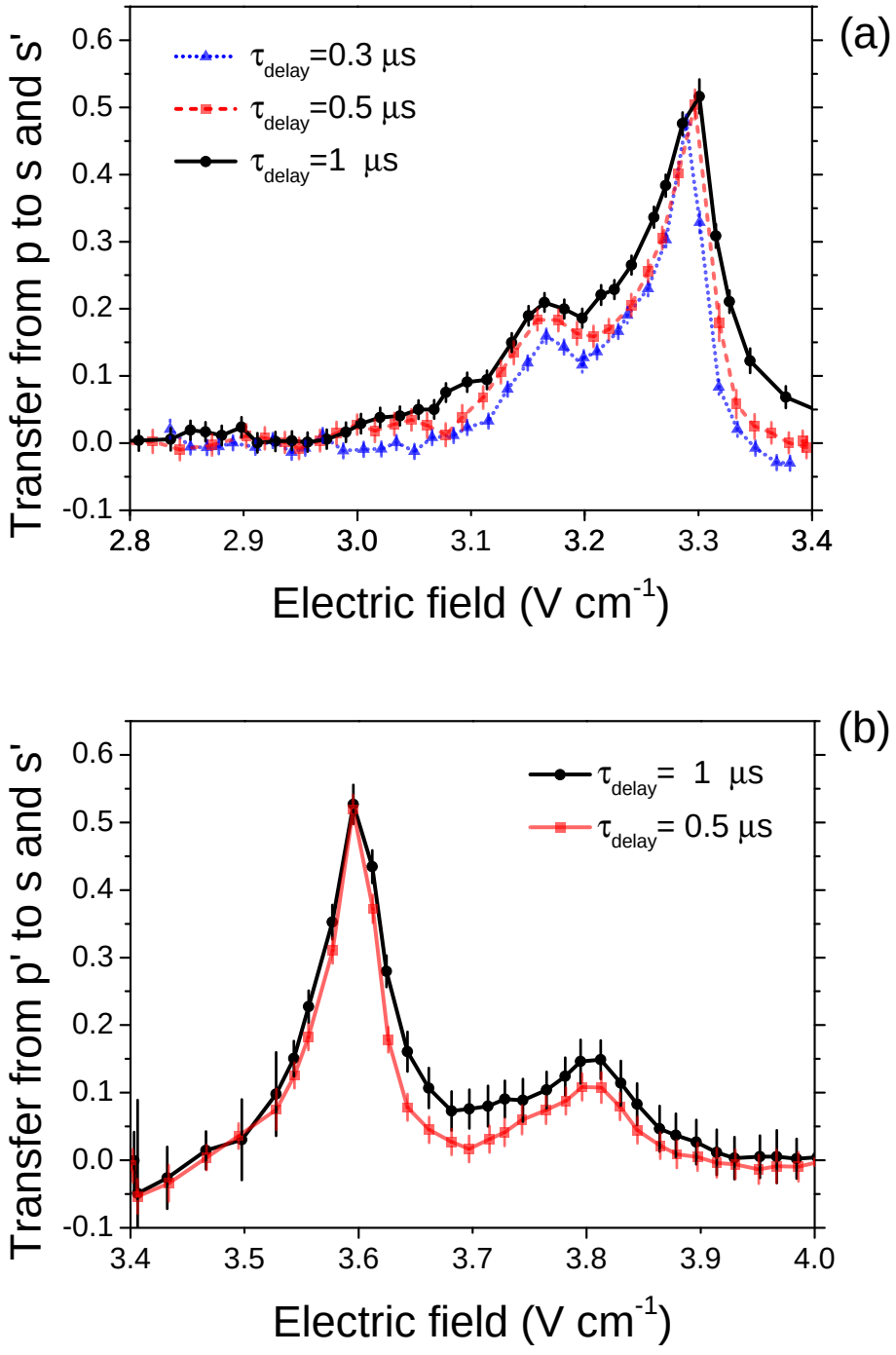

Figure 5.4: Averaged transfer ratio from the initial p state (a) or p' state (b) to $s + s'$ states for $n = 35$ at different τ_{delay} versus the electric field.

We start by considering the case of $n = 35$ which presents the strongest transfer as we could expect from the scaling of the three-body coupling term (see equation 5.5). In Fig. 5.4 (a), we plot the population transfer ratio as a function of the external electric field F for an initial state p. The different colors correspond to a different ionization delay τ_{delay} we set. We resolve two peaks respectively at $F = 3.17 \pm 0.02$ V cm^{-1} and $F = 3.30 \pm 0.02$V cm^{-1}. The first one corresponds to the three-body interaction described by 5.1 while the second peak is due to the two-body interaction described by equation 4.2. We can calculate the theoretical value for the electric field in the analogous way we calculate the ones for the quasi-forbidden resonances in chapter 4. We finally obtain the values of $F = 3.15 \pm 0.05$ V cm^{-1} and $F = 3.28 \pm 0.05$ V cm^{-1} respectively for three-body and two-body peaks.
In the case of a saturated three-body interaction we would expect to transfer half the population in $s + s' + p'$ while the other half remains in $p + p + p$, so the ratio of atoms in $s + s'$ would be $1/3 \approx 33\%$. We finally observe a transfer up to 21 %, close to but below the expected one.
For the case of the two-body resonance we observe a saturated peak of 50 % of transfer. The saturation can be due to two different effects: the dipole blockade and the mean effect of coherent oscillation of the two-atom states populations.In the case of a Förtster resonance a partial blockade effect can lead to the direct excitation of one of the two exciton states $1/\sqrt{2}[|pp\rangle \pm 1/\sqrt{2}(|ss'\rangle + |s's\rangle]$. The direct excitation and detection of these latter states with our detection apparatus corresponds to the detection of a transfer ratio of 50 %. For the experimental case considered we estimate a dipole-dipole coupling of 15 MHz for two atoms at a distance of 3 μm that is reasonable considering our experimental density $\approx 5 \times 10^9$ atoms per cm^3. The laser linewidth of the Rydberg excitation is estimated of ≈ 10 MHz so at this level a partial excitation blockade effect is non negligible. The laser excitation can thus directly excite one of the two exciton states $|\psi_\pm\rangle = \frac{1}{\sqrt{2}}\big[|p, p\rangle \pm \frac{1}{\sqrt{2}}(|s, s'\rangle + |s', s\rangle]$ and this explains the saturated peak. In the case of the three-body interaction we estimate a three-body coupling $V_{3b} \approx 3$ MHz for atoms at 3 μm well below a blockade regime.
The second effect that can lead to the transfer saturation is related to the coherent oscillations of the two exciton states and directly depends on the ionization delay. If we consider a couple of Rydberg atoms initially prepared in a $|pp\rangle$ the system will oscillates between $|pp\rangle$ and $\frac{1}{\sqrt{2}}(|s, s'\rangle + |s', s\rangle)$ at a frequency equal to the dipole-dipole coupling because at resonance the eigenstates of the system are the exciton states $|\psi_\pm\rangle$. The coherent oscillation of two Rydberg atoms coupled by a dipole-dipole interaction at a Förster resonance has been recently observed in [Ravets et al., 2014]. In this experiment the precise control of the orientation and of the reciprocal distance between

Rydberg atoms allow the observation of a coherent oscillation. In our experimental set up the Rydberg atoms are excited at random distances with random orientation, so it is not possible to observe a coherent oscillation. What we see is the mean effect of all dipole-dipole couplings between all the possible couple of Rydberg atoms. The saturation is reached after a characteristic time $1/V_{dd}$, where $V_{dd} = \langle pp|\widehat{H}_{dd}|ss'\rangle$, which corresponds to the period for a single coherent oscillation. For the case $n = 35$ since a dipole-dipole coupling strong enough to induce a partial blockade is already present in this case the saturation is the combination of the two effects.
In Fig. 5.4 (b) we observe the analogous measurement for an initial state p'. We resolve the two and three-body peak respectively at $F = 3.59 \pm 0.02$ V cm^{-1} and $F = 3.80 \pm 0.02$ V cm^{-1} in good agreement with the predicted values $F = 3.6 \pm 0.05$ V cm^{-1} and $F = 3.80 \pm 0.05$V cm^{-1}. We still observe a saturated peak for the Förster resonance and a smaller transfer efficiency for the three-body peak of 15 % due to a smaller estimated coupling $V_{3b} \approx 2$ MHz. We can expect a smaller coupling because as we increase the external electric field the splitting energy $\delta_{pp'}$ gets larger (from ≈ 70 MHz for $F = 3.15$ V cm^{-1} to ≈ 95 MHz for $F = 3.80$ V cm^{-1}). For this same reason, the peak for the two-body and three-body peaks are better resolved.

In Fig. 5.5 we plot the analogous measurement for a principle quantum number $n = 28$. In both cases we observe a three-body transfer peak on the left-side of Förster peak for an initial p state and a three-body transfer peak on the right-side of Förster peak for an initial p' state. The predicted values for the three-body and two-body peaks for a p state are $F = 18.30 \pm 0.05$ V cm^{-1} and $F = 19.05 \pm 0.05$ V cm^{-1}. The predicted value for a p' are at $F = 22.05 \pm 0.05$ V cm^{-1} for a three-body interaction and at $F = 20.91 \pm 0.05$V cm^{-1} for a two-body interaction. In both cases we observe a saturated two-body peak even if the estimated dipole coupling $V_{dd} \approx 5$ MHz, not large enough to induce a blockade effect. In this case the peak saturation is due, as we have previously introduced, to the mean effect of the coherent oscillations. The ionization delay we choose, 2 μs is comparable to $1/V_{dd}$ so large enough to see a saturation due to a temporal evolution.
In the case of $n = 28$ the peaks are well resolved because the energy splitting $\delta_{pp'}$ is bigger than in the case of $n = 35$. We observe a transfer of $\approx 4\%$ well below the 21 % we observe for $n = 35$. This is compatible with the scaling of V_{3b}.
In Fig. 5.5 we observe additional peaks that are due to quasi-forbidden Förster resonances as the one we described in chapter 4. They are related to two quasi-forbidden

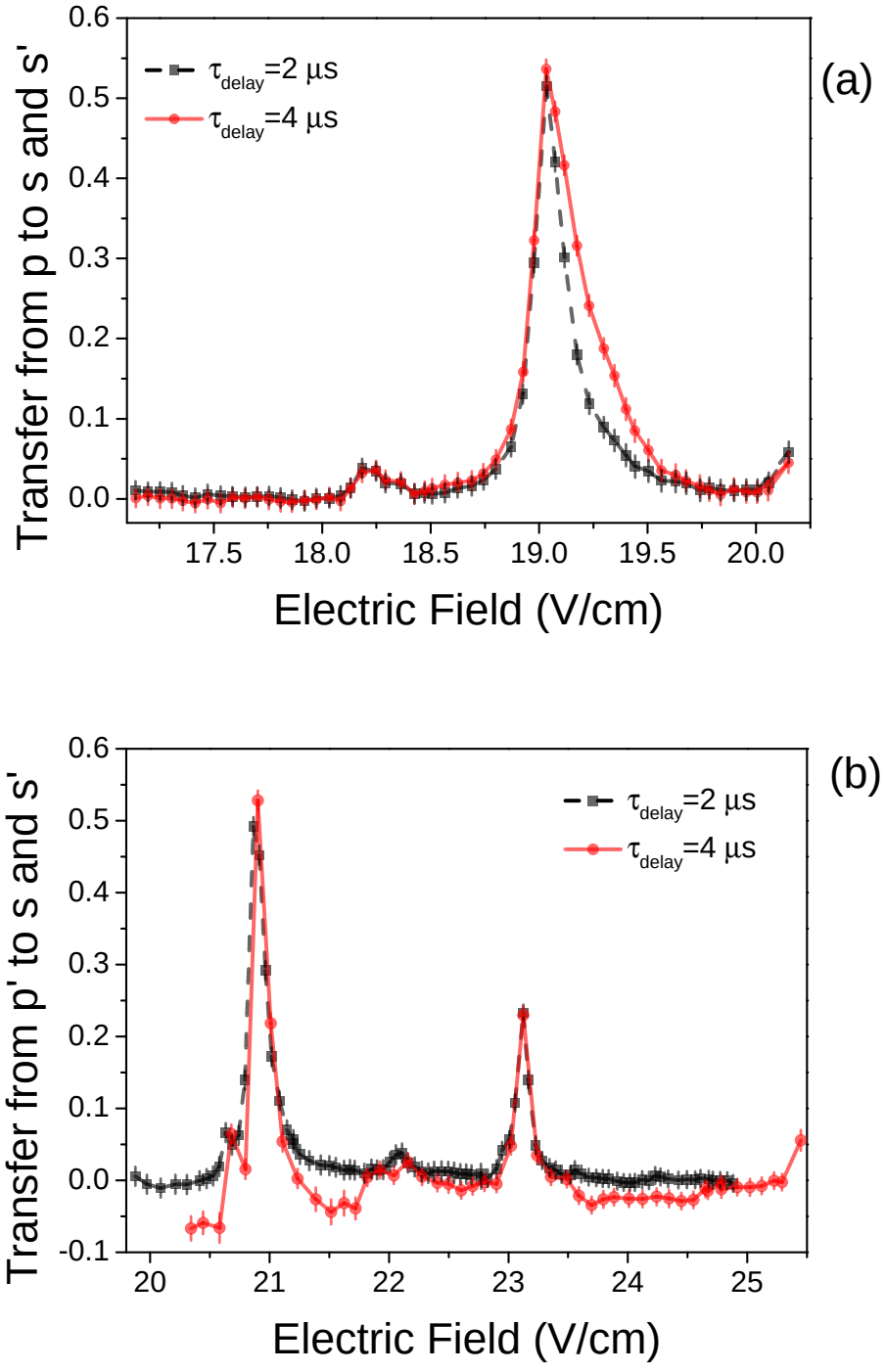

Figure 5.5: Averaged transfer ratio from the initial p state (a) or p' state (b) to $s + s'$ states for $n = 28$ at different τ_{delay} versus the electric field.

Förster resonances:

$$2p_{3/2}|m_j| = 3/2 \leftrightarrow 29s_{1/2} + 24f_{7/2}|m_j| = 3/2$$
$$2p_{3/2}|m_j| = 3/2 \leftrightarrow 29s_{1/2} + 24f_{7/2}|m_j| = 5/2$$

which occur at the same electric field. We have already observed this peak in Fig. 4.8. A more detailed description can be found in paragraph 4.2.5 in the section Forbidden resonances from $|28p_{3/2}|m_j| = 3/2\rangle$.

5.2.2 Time dependence

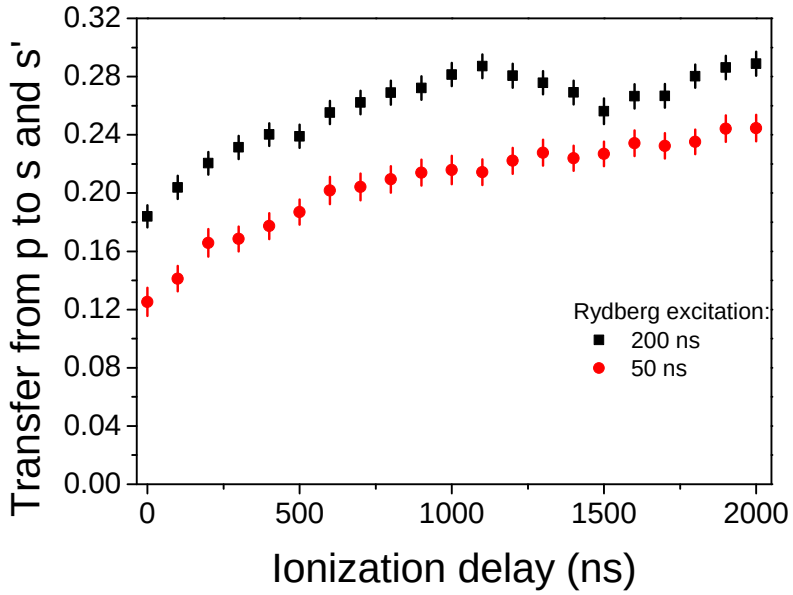

Figure 5.6: Time evolution of three-body transfer peak for p ($n = 35$) for two different Rydberg pulse durations.

In Fig. 5.4 we plot the transfer ratio for different ionization delays τ_{delay}. We can see an evolution of the transferred ratio of the three-body peak when we increase the ionization delay. In Fig. 5.6-5.7 we report a more accurate study of the temporal evolution of the transfer ratio at the resonant field for an initial state p ($F = 3.15$ V cm^{-1}) and for an initial state p' ($F = 3.80$ V cm^{-1}) both for $n = 35$.

We report the measurement for both p and p' resonance for two different initial densities of Rydberg atoms corresponding to two different pulse durations for the Rydberg excitation. We have for a pulse of 50 ns a corresponding Rydberg density $d \approx 8 \times 10^8$ atoms per cm^3 while for 200 ns the density is $d \approx 4 \times 10^9$. In both cases we observe a transfer ratio different from zero even for zero ionization delay. The evolution of the population even at a zero ionization delay due to two different aspect: the finite time of the Rydberg excitation and the strength of the three-body coupling. Since we need a Rydberg pulse that last tens or even hundreds of ns we can even have a time evolution of the Rydberg populations during the excitation of the Rydberg atoms. Moreover the three-body coupling is $V_{3b} \approx 2 - 3$ MHz that cannot be totally neglected compared to the laser linewidth $\Gamma_L \approx 10$ MHz. The three-body coupling is not strong enough to saturate the transfer as in the case of the two-body interaction, but it can lead to the direct excitation of the three-body exciton states:

$$|\psi_{\pm}\rangle = \frac{1}{\sqrt{2}}\big[|ppp\rangle \pm \frac{1}{\sqrt{6}}(|ssp'\rangle + |sp's'\rangle + |s'sp'\rangle + |s'p's\rangle + |p'ss'\rangle + |p's's\rangle)\big].$$

We observe an increase of the transferred ratio as we increase the ionization delay. We obtain a maximum transfer ratio of 29 % for a ionization delay of 2 μs (Fig. 5.6). For an estimated three-body coupling of 2 MHz we would expect a saturation due to the temporal evolution for a $\tau_{delay} \approx 500$ ns.

We also study the temporal evolution of the transferred atoms for the two-body resonance of equation 4.3. In Fig.5.8 we plot the time evolution of the transfer ratio for a two-body resonance of p' at a resonant field $F = 3.60$ V cm^{-1} for a Rydberg pulse duration of 100 ns (with a corresponding density $d \approx 2 \times 10^9$ atoms per cm^3), 50 ns ($d \approx 8 \times 10^8$ atoms per cm^3) and 13 ns ($d \approx 4 \times 10^8$ atoms per cm^3). For density $d \approx 4 \times 10^8$ atoms per cm^3 we can see a transient regime before reaching the saturation at $\tau_{delay} \approx 1.5$ μs which is consistent with an estimated coupling of ≈ 1.5 MHz. For the higher density the transfer ratio is already saturated due to the strong dipole-dipole interaction. In Fig. 5.8 we can see that the transfer ratio overcome the 50 %. We are not able to say if it is related due to an overestimation of the number of transferred atoms or if related to a new physical phenomenon.

In Fig. 5.4 we can see as we increase the ionization delay the peak of transfer gets broader. This effect is compatible with the many-body diffusion model proposed in [Mourachko et al., 1998, Anderson et al., 1998]. This model considers that once several couples of atoms have been transferred from $p'p'$ to ss', because of resonant Förster coupling, the migration processes $p' + s \rightarrow s + p'$ and $p' + s' \rightarrow s' + p'$ can lead to the diffusion of s and s' atoms. The diffusion of the s and s' products can allow the original pair to interact again from two p' states and thus facilitate a Förster resonance

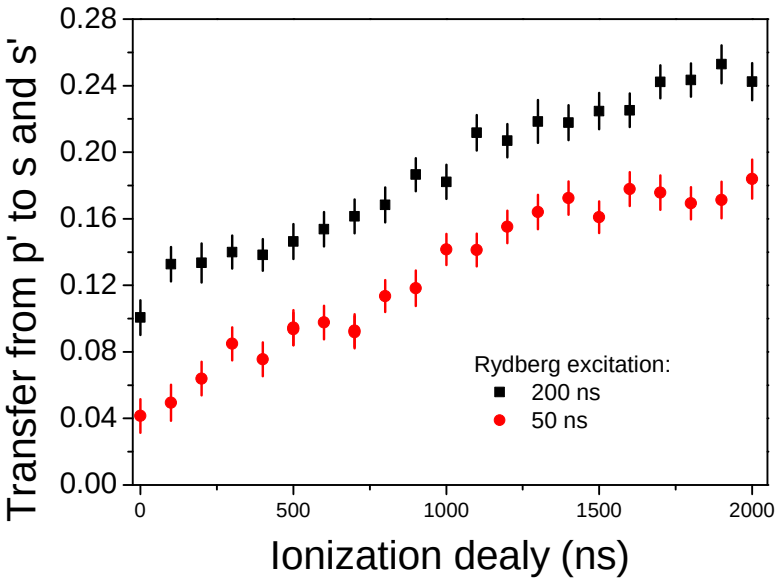

Figure 5.7: Time evolution of three-body transfer peak for p' ($n = 35$) for two different Rydberg pulse durations.

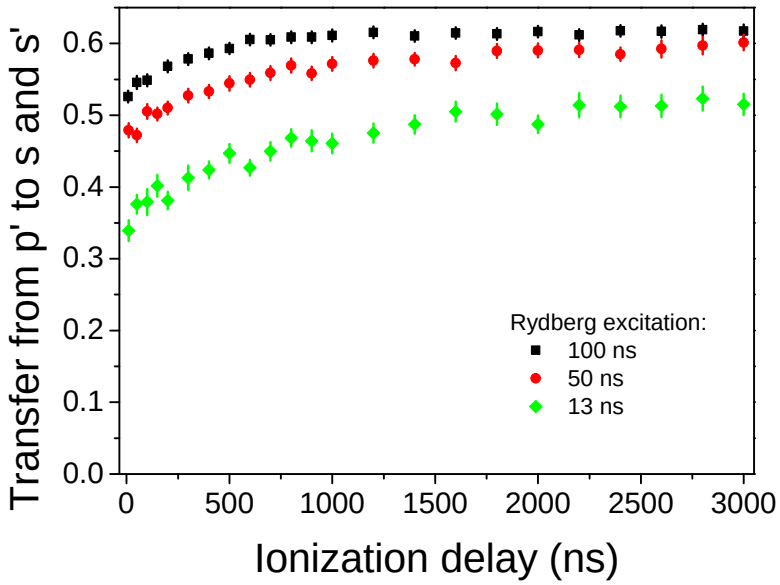

Figure 5.8: Time evolution of the transfer for a non-resonant electric field two-body peak for p' ($n = 35$) for different Rydberg pulse durations.

transfer. This kind of model can be also applied to the three-body processes. The three-body processes can lead to the excitation of s and s' states that can diffuse in the atomic sample because of migration processes and facilitate further three-body interactions.

5.2.3 Density dependence

To further characterize the three-body interaction we studied the transfer dependence on the initial Rydberg atom density. This measurement is analogous to the one used in [Gurian et al., 2012] for characterizing a four-body interaction. In the case of a diluted gas an N-body process will depend as the N-power of the initial density. We can thus expect for a two-body interaction a quadratic scaling of the transfer of atoms while for three-body we instead expect a cubic scaling versus the initial density.
We choose to study this scaling for the p' state because the two peak are better resolved compared to the case of p. We also choose the case of the highest principal quantum number we have studied ($n = 35$) because for this value we have the largest

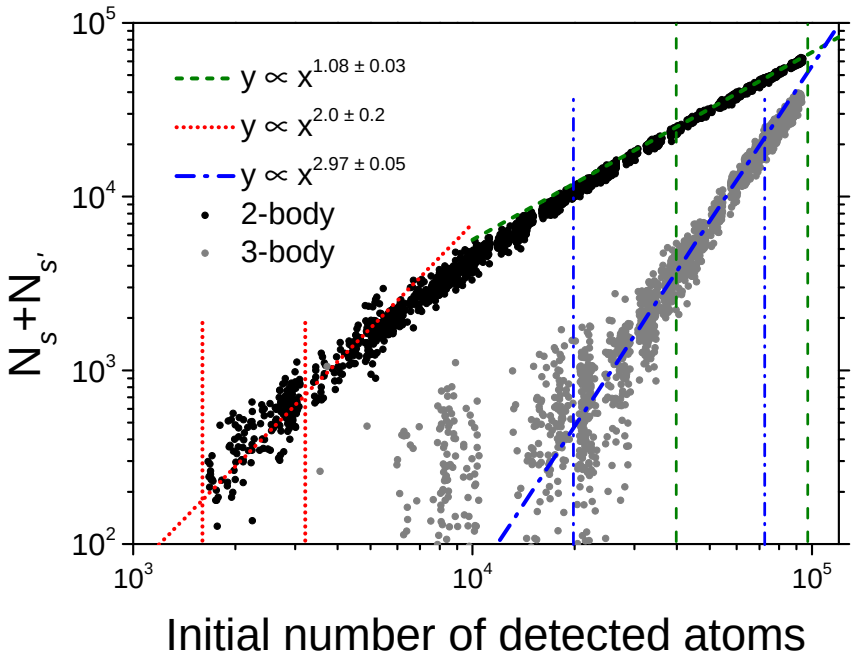

Figure 5.9: Sum of detected atoms in s and s' states (N_s+$N_{s'}$) versus the initial $n = 35$ p' Rydberg atoms density for a ionization delay of $\tau_{\text{delay}} = 0.5$ μs at a fixed electric field of 3.60 V cm^{-1} for the 2-body (black points) in bi-logarithmic scale. n the low density regime, the fit is compatible with a quadratic law (red dotted line) while in the high density regime is compatible with a linear scaling (green dashed line). The grey points are taken at 3.80 V cm^{-1} for the three-body resonance and the scaling is compatible with a cubic law (blue dotted dashed line). The data range used for each fit is demarcated by couples of vertical lines with corresponding color and style.

dipole-dipole coupling. We thus set the value at the resonant field respectively for the two-body and three-body peak and then we measure the number of atoms transferred to an $s + s'$ state varying the Rydberg pulse duration and thus the initial density of atoms in p'.
In Fig. 5.9 we plot in a bi-logarithmic scale the resulting number of transferred atoms as a function of the initial number of Rydberg atoms for the two-body resonance at 3.60 V cm^{-1} (black points). For the case of the two-body resonance we observe a quadratic scaling as revealed by the red dotted line with slope coefficient 2.0 ± 0.2 in the low density regime (up to $d \approx 1.5 \times 10^8$ atoms per cm^3). In this regime the density of atoms in $s + s'$ scales as $\rho_{s+s'} \propto \rho_{p'}^{2.0\pm0.2}$. The green dashed line is the linear fit with slope coefficient 1.08 ± 0.03 and it reveals when the two-body process starts to saturate with a transfer ratio around 50 % and it starts at a density $d \approx 8 \times 10^8$ atoms per cm^3 as we have already seen in Fig. 5.8 for the the red points at 50 ns. At this density we estimate a dipole-dipole coupling of $V_{dd} \approx 1.5$ MHz at 3 μm distance, so the dipole blockade effect should be negligible and the saturation is due to the temporal evolution since the ionization delay we choose for the density dependence study is 500 ns which corresponds roughly to $1/V_{dd}$. The grey points are the analogous data taken for the three-body resonant field $F = 3.80$ V cm^{-1}. The points can be fitted by the blue dashed-dotted line with slope coefficient of 2.97 ± 0.05. For a three-body process we thus see a characteristic scaling $\rho_{s+s'} \propto \rho_{p'}^{2.97\pm0.05}$. We start to observe a change of the slope for high density $d \approx 5 \times 10^9$ atoms per cm^3 when the transfer ration reaches the corresponding value of 25 %, close to the expected maximum of 33 %. An increase of the Rydberg density would probably reveals a transitory regime before reaching the saturation value of 33 %.

5.3 From few to many-body interaction

The generalization of few-body process has acquired more and more interest because it seems to have promising perspectives for the comprehension of many-body processes. In this way theoretical works have opened the study of three-body Borromean state [Kiffner et al., 2013] and their extension to N-body interaction, the so called Brunnian interaction [Yamashita et al., 2010]. Concerning the interaction scheme we propose for a three-body interaction, the use of a virtual level for absorbing the energy mismatch of Δ_p can also inspire an extension of the mechanism to a many-body process. The first condition required is to consider two resonant many-body states composed by single atom states p, p', s and s'. The energy mismatch of the Förster defect is the adjustable parameter that permits to tune the two n-atom states. In the following

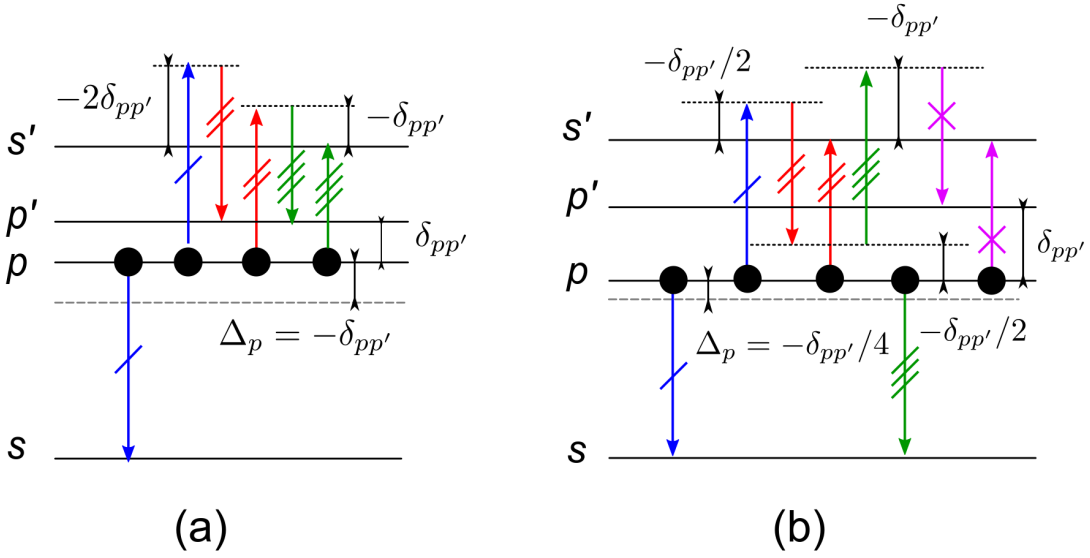

Figure 5.10: Generalization of possible energy transfer for: (a) a four-body FRET denoted with 4^2 and (b) a five-body FRET denoted with 5^1. The scheme refers only to the case of 4 or 5 atoms in a p state but it can be also generalized to the case of p'.

section we will discuss the generalization of the resonances from a p state, but of course the same can be done if we consider p' state. For a number of atoms $2N + M$ where N and M are natural numbers, we can define the following resonant transfer equation:

$$(2N + M) \times p \leftrightarrow N \times s' + N \times s + M \times p' \tag{5.6}$$

with a Förster defect:

$$\Delta_p = -\frac{M}{2N}\delta_{pp'}. \tag{5.7}$$

With this definition for the many-body interaction we can introduce a new notation $(2N + M)^M$. With this notation the two-body Förster resonance is labelled with 2^0 while the three-body FRET is 3^1.
In Fig.5.10 we present the energy transfer scheme respectively for (a) the four-body resonance 4^2 at a Förster defect $\Delta_p = -\delta$ and (b) the five-body resonance 5^1 at a Förster defect $\Delta_p = -\delta/4$. The 4^2 process can be described by the transfer equation:

$$4 \times p \leftrightarrow s + s' + 2p'. \tag{5.8}$$

with a Förster defect:

$$\Delta_p = -\delta_{pp'} \tag{5.9}$$

The energy transfer scheme of Fig. 5.10 (a) is a simple generalization of the one presented in Fig.5.2(a) where we just need to add an additional virtual level detuned by the quantity $-2\delta_{pp'}$ from the s' level. This additional virtual level implies an additional order in the calculation of the four-body coupling. In analogy with equation 5.5 we can write the four-body coupling as:

$$V_{4b} = \frac{V_{dip1}V_{dip2}V_{dip3}}{(2\Delta_p)^2} \tag{5.10}$$

where V_{dip1}, V_{dip2} and V_{dip3} are the dipole-dipole coupling between the states connected respectively by the blue single marked, the red double marked and the green triple marked arrows. It seems evident that this four-body coupling is strongly depressed compared to the three-body. It is evident because the resonance condition is obtained at a larger detuning Δ_p from the two-body FRET and because the coupling is calculated at a higher order of perturbation. At this electric field the detuning at denominator of equation 5.10 depresses the 4-body coupling.
In Fig. 5.10 (b) we instead present a slightly different energy scheme where we consider two virtual levels detuned by $-\delta_{pp'}/2$ and $-\delta_{pp'}$ with respect to the s' state and

a third virtual level detuned a quantity $-\delta_{pp'}/2$ respect to p. The 5^1 process can be described by the transfer equation:

$$5 \times p \leftrightarrow 2s + 2s' + p'. \tag{5.11}$$

with a Förster defect:

$$\Delta_p = -\delta_{pp'}/4 \tag{5.12}$$

In this case the five-body coupling is the result of a forth-order perturbative calculation but the smaller Förster defect, $\Delta_p = -\delta_{pp'}/4$ can compensate the additional order of expansion.

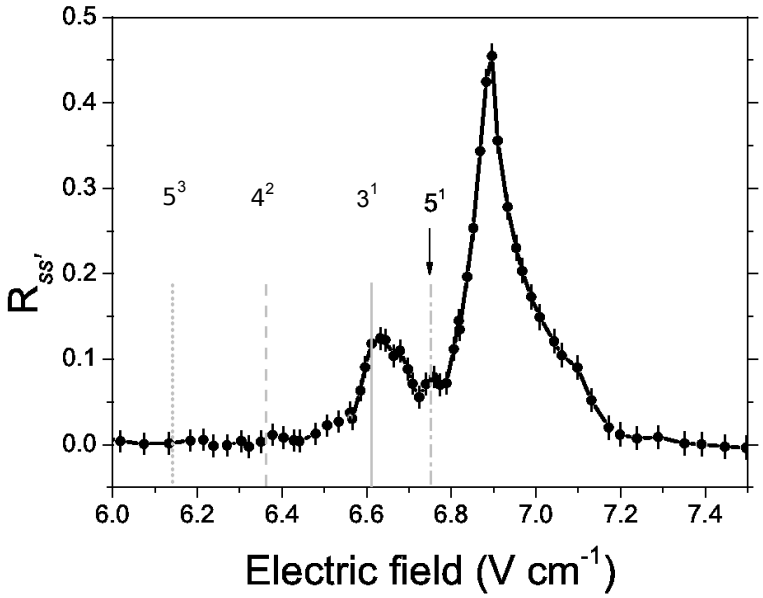

Figure 5.11: Averaged transfer ratio from the initial p state to $s + s'$ for $n = 32$ with a ionization delay of $\tau_{delay} = 1$ μs. The dotted line at 6.14 V cm^{-1} corresponds to the 5^3 5-body FRET, the dashed line placed at 6.36 V cm^{-1} corresponds to the expected 4^2 4-body FRET and the dashed dotted line at 6.74 V cm^{-1} corresponds to the 5^1 5-body FRET. We also report the solid line at 6.61 V cm^{-1} for the expected electric field for the 3-body FRET peak.

In Fig. 5.11 we present some preliminary measurement of a many-body interaction for principal quantum number $n = 32$. We clearly observe a two-body peak at $F = 6.89 \pm 0.02$ V cm^{-1} and a three-body peak at $F = 6.63 \pm 0.02$ V cm^{-1} that are in perfect agreement with the predicted values $F = 6.89 \pm 0.05$ V cm^{-1} and $F = 6.61 \pm 0.05$ V cm^{-1}. We also report with a vertical line the predicted values for the new few-body resonances we have introduced. The dot-dashed line at $= 6.74 \pm 0.05$ V cm^{-1} states for the predicted value for a 5^1 resonance peak while the dashed line in at $F = 6.36 \pm 0.05$ V cm^{-1} is placed at the predicted electric field for a 4^2 resonance. We also report the predicted value for a 5^3 resonance at $F = 6.14 \pm 0.05$ V cm^{-1}.
In Fig.5.12 we plot a zoom of Fig.5.11 in the electric field range from 6.55 to 6.95 V cm^{-1} that corresponds to the range between the three-body peak and the two-body peak. In this range of the electric field we predict to observe a 5^1 resonance peak. We observe a small increase of the transfer ratio with a maximum at an electric field $F = 6.75 \pm 0.02$ V cm^{-1} which is close to the expected value for a 5^1. However, the amplitude of this signal is comparable to the measurement error. Additional investigation of these range of electric field are necessary if we want to evaluate if this smooth peak is really due to a 5^1 or it is only an artefact due to the overlap of the two-body and three-body peak. Moreover we estimate the coupling for this kind of resonance with a generalization of the equation 5.5 for a forth-order of perturbation and we find $V_5 = 25$ kHz for an inter-particle distance of 3 μm which seems too small to explain the visibility of this effect.

In Fig. 5.13 we report a zoom for the electric field range from 6 to 6.6 V cm^{-1} where we expect to observe a four-body resonance of the kind 4^2 for an electric field of $F = 6.36 \pm 0.02$ V cm^{-1}. In this case we observe a slight increase of the transfer ratio at an external electric field $F = 6.37$ V cm^{-1}, but the amplitude of the peak ≈ 0.01 is comparable to the experimental error bars and thus compatible with zero. The eventual detection of a four-body peak is completely covered by the statistical noise of our detection procedure. We have also estimated the four-body coupling of equation 5.10 and we obtain $V_{4b} = 11$ kHz for for an inter-particle distance of 3 μm.
The data we present in Figs.5.11-5.12-5.13 are the average of 150 - 300 individual measurements, while the data in Fig. 5.4 are the average of 50 - 150 individual measurements. We almost double the number of acquired points in order to reduce the signal to noise ratio and thus make the 5^1 and 4^2 peak emerge from the noise. Even though we increase the number of measurement we do not observe clearly an increase of the transfer ratio at the expected electric field. Several factors can reduce the possibility to observe these resonances. First of all the weak coupling compared

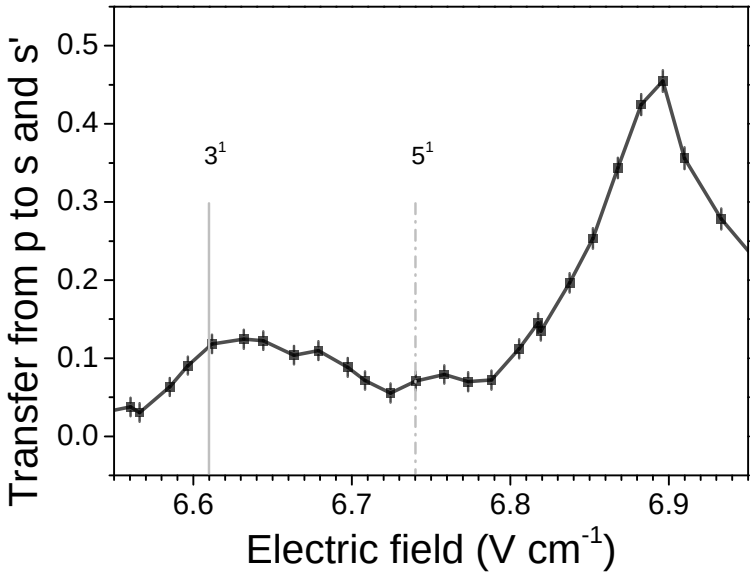

Figure 5.12: Zoom of Fig.5.11 from 6.55 to 6.95 V cm^{-1}. We can see a small increase of the signal in the proximity of the dot dashed line at 6.74 V cm^{-1} which mark the expected electric field for a 5^1 resonance. The solid line at 6.61 V cm^{-1} corresponds to the 3-body FRET.

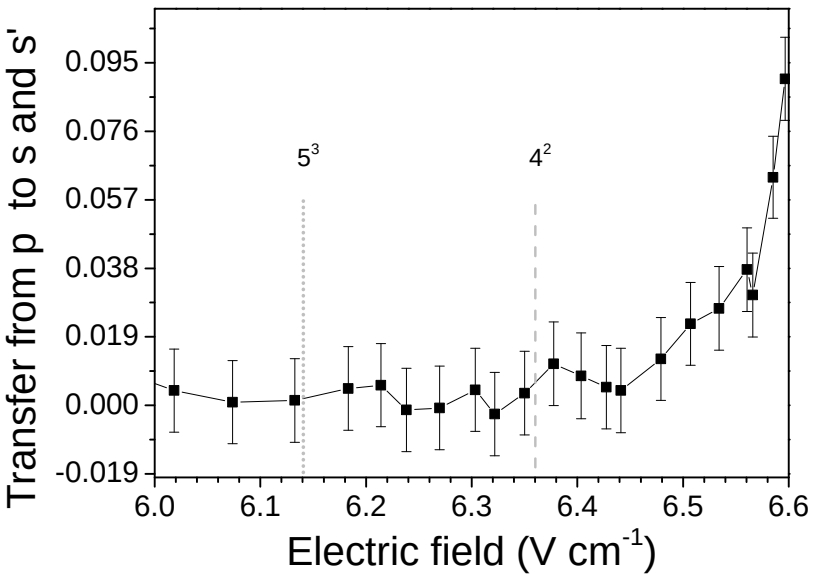

Figure 5.13: Zoom of Fig.5.11 from 6 to 6.6 V cm^{-1}. The dotted line at 6.14 V cm^{-1} corresponds to the 5^3 5-body FRET while the dashed line at 6.36 V cm^{-1} corresponds to 4^2 4-body FRET.

to the one of a two-body and three-body FRET. For that reason a possible solution could be to increase the density of atoms in the sample. However the increase of the atomic density could lead to a broadening effect of the two-body and three-body peak because of a strong coupling and thus the merge of all the resonance peaks.

5.4 Quantum engineering with 3-body interaction

Förster resonances have attracted the interest of the scientific community for their promising applications in quantum optics and quantum computing. The external tunability of a Förster resonance has been exploited for the realization of an entanglement experiment [Gaëtan et al., 2009, Wilk et al., 2010]. Moreover the strong dipole-dipole interaction has been proposed for the implementation of quantum gates [Saffman et al., 2010]. In this direction important results have been achieved in the implementation of a C-NOT quantum gate [Isenhower et al., 2010] that represents the first demonstration of quantum gates and entanglement between a single pair of

trapped neutral atoms. The strong analogy between two-body and three-body FRET makes them a promising candidate for the implementation of quantum entanglement experiment as well as quantum gates.
Considering the scaling $1/R^3$ of the dipole-dipole interaction it seems evident that the control of inter-particle distances has an essential role if we want to use the three-body coupling V_{3b} for the implementation of an entanglement experiment and three-body quantum gate. Unfortunately our experimental set up does not allow a precise control of the distances between excited Rydberg atoms. So that the proposed application of a three-body FRET in quantum computing requires an experimental set up with a high precision control as the one of [Barredo et al., 2015] where the exploitation of optical tweezer array allows the precise control of the reciprocal distances between Rydberg atoms. For the next paragraph we will treat the case of three atoms in a p state, but the same consideration can be done for three atoms in a p' state.

5.4.1 3-body entanglement

The first application we examine is the implementation of three-body entangled state. We have already seen that a two body FRET finally produced an entangled state of $|pp\rangle$ and $|ss'\rangle$:

$$|\psi_{\pm}\rangle = \frac{1}{\sqrt{2}}\big[|pp\rangle \pm \frac{1}{\sqrt{2}}(|ss'\rangle + |s's\rangle\big]. \tag{5.13}$$

where we take into account the symmetrization of the $|ss'\rangle$. In an analogous way we can write the fully entangled state for the case of a three-body interaction as:

$$|\Psi\rangle = \frac{1}{\sqrt{2}}\big[|ppp\rangle \pm \frac{1}{\sqrt{6}}(|ssp'\rangle + |sp's'\rangle + |s'sp'\rangle + |s'p's\rangle + |p'ss'\rangle + |p's's\rangle)\big] \tag{5.14}$$

where we take into account all the possible permutations of s, s' and p' for the symmetrization of $|ssp'\rangle$. We can thus use the three-body interaction for the implementation of the fully entangled state described by equation 5.14.
The implementation of this entangled state requires first of all some considerations on the geometry of the array of atoms. First of all the asymmetric role of the relay atom which exchanges energy twice with the other two and necessarily ends in a p' state can a priori forbid to obtain a fully entangled three-atom state. Moreover the anisotropy of the dipole-dipole interaction and the probability distribution of the orbitals p imposes extra conditions for a possible interaction. In order to overcome these limitations we propose to arrange the three atoms at the extremity of an equilateral triangle configuration with the external electric field perpendicular to the plane containing the three

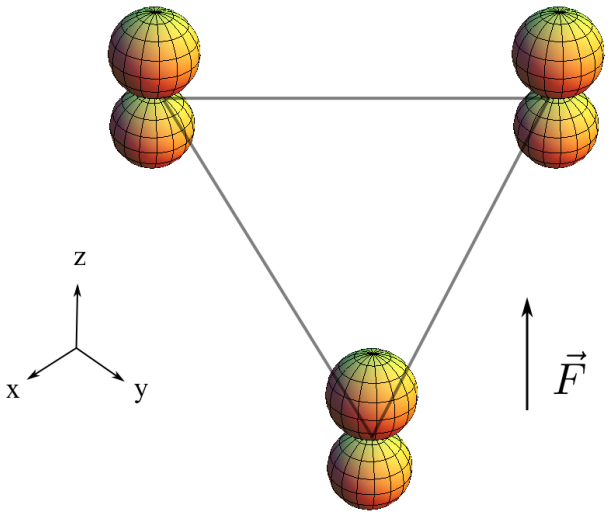

Figure 5.14: Proposed scheme for a three-body entanglement. The three atoms are represented by the p orbital placed at the extremity of equilateral triangle in the x-y plane. The external electric field is perpendicular to this latter plane.

atoms. In Fig. 5.14 we present a schematic representation of such a configuration. We choose as quantization axis the direction of the external electric field. The electric field induces a dipole moment in each atoms, we can thus consider the orbital p, we use to describe the Rydberg state, oriented along the direction of the electric field. The atoms are at the extremity of an equilateral triangle. This configuration is symmetric by a rotation of 120 ° along the z axis and by a reflection with respect to the x-y plane. Each atom is at the same distance from each other is oriented in the same direction. It results that no atom has a privileged role, each one can play the role of the relay because the coupling between the atoms will be the same. The realization of such kind of experiment require an extremely precise control of the geometry of the system because any variation can break the symmetry and thus the realization of fully entangled state.

5.4.2 Heralded entanglement

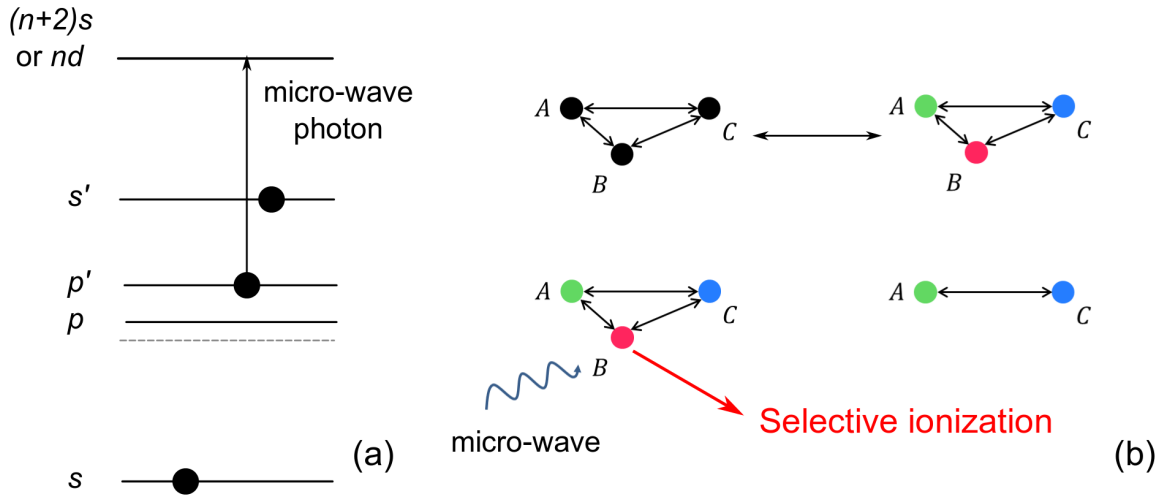

Figure 5.15: (a) Scheme of a possible μ-wave assisted ionization. The p (or p') state is selectively ionized without affecting the other Rydberg states. (b) Procedure for a heralded entanglement experiment: the atoms are first prepared in a p state and because of a three-body resonant interaction the atoms change their states. The atom in a p' state is then selectively ionized with a μ-wave photon and the final state is an entangled state of s and s'.

In an entanglement experiment a "witness", or "herald" signal which demonstrate the effective entanglement can increase the reliability of the operation. The herald signal can be generated by the detection of a photon signal [Bernien et al., 2013, Casabone et al., 2013].
We propose here the implementation of an heralded entanglement experiment using the relay atom, that changes its Zeeman sub-level after a three-body interaction as the herald. We have seen that when a three-body interaction takes place the final state is a superposition of $|ppp\rangle$ and all the possible permutation of $|ss'p'\rangle$. The selective ionization of the p' state will project the three-atom state into the two-body entangled state:

$$|\psi_{heralded}\rangle = \frac{1}{\sqrt{2}}(|ss'\rangle + |s's\rangle). \tag{5.15}$$

and thus the detection of the ionized p' state will herald the entanglement. Since the p' state is in a lower energy level compared to the s' we cannot simply field ionize it because we will also destroy the entangled state. We propose to use an external micro-wave field to couple the p' to a Rydberg state of a higher manifold and then ionize it with an ionization ramp. In this case the ionization field required will be well below the ionization limit for an s' state. In this way it should be possible to ionize just the p' state without affecting the entangled state of equation 5.15. Because of the dipole selection rules we can couple the p' with a d or s state of the upper manifolds. In Fig. 5.15 (a) we resume the idea of a micro-wave assisted ionization. The p' can be coupled to the an upper state nd_j with $j = 3/2$ or $5/2$. A second possibility is to choose the transition $p \rightarrow (n+2)s$. In both cases the energy required for the transition is in a range between tens and hundred of GHz for the principal quantum numbers $n = 28 - 35$ we studied.
In Fig. 5.15 (b) we present a possible experimental sequence for the realization of this kind of experiment. We can first excite atoms in a p state at the resonant field for a three-body resonance. At this field three atoms interact because of the three-body coupling and are then transferred in a $|ss'p'\rangle$ state. At this moment the relay atom which now is in a p' state is coupled to an upper manifold by a micro-wave radiation and can thus be ionized without destroying the two-body entangled state.

5.4.3 Fredkin gate

In paragraph 5.4.1 we have seen that the three-body interaction forcedly produce an entanglement between the three-body atom states. We have also written in equation 5.14 the expression of the fully entangled state as a superposition of the $|ppp\rangle$ and all the permutations of $|ss'p'\rangle$. The permutations correspond to all the spatial

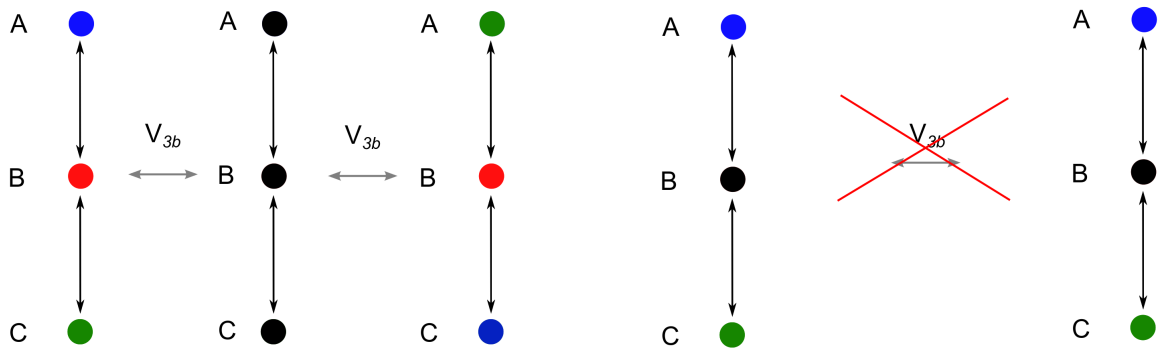

Figure 5.16: Implementation of a Fredkin quantum gate. (a) The control qu-bit B is set to 1. The temporal evolution of a three-body interactions can lead to to the final swap of the states between the atoms in A and C while (b) when the control qu-bit B is set to 0, no three-body interaction is allowed and thus no swap between A and C is possible.

configurations we can obtain with three atoms in s, s' and p'. We have to consider all the possible spatial permutations because we are not able to distinguish which atom turns to which state. The symmetrization of the $|ss'p'\rangle$ can thus be exploited for the swap of the atoms that is the base for the implementation of a Fredkin gate [Fredkin and Toffoli, 1982].
A Fredkin gate also known as CSWAP is a three-body quantum gate. It is composed by two input bits and a control bit. When the control bit is set to one the Fredkin gate acts a swap on the two input bits. The output bits are thus the two input bits with exchanged positions. When the control bit is set to zero the input bits are left unchanged. We report for clarity the truth table of Fredkin gate where C is the control bit and I_1, I_2 are the input bits and O_1, O_2 are the output bits.

The idea is to use the temporal evolution of a three-atom state due to a three-body coupling as the leading mechanism for the swap of the qu-bits. In Fig. 5.16 we present a possible implementation of a Fredkin quantum gate. Three atoms are placed in a linear lattice. The atom in B plays the role of the control qu-bit and it is in a p' (red circle). The atom in A and C are prepared in a s (blue circle) and s' (green circle) state. An external electric field resonant with the three-body interaction $|ppp\rangle \leftrightarrow |sp's'\rangle$ is applied. Because of the three-body coupling the system oscillates between the $|ppp\rangle$ and the $1\sqrt{2}(|sp's'\rangle + |s'p's\rangle)$. The state $|s'p's\rangle$ exactly corresponds to the final state of the swap action. On the other side if the atom in B is not in an p' at the beginning, there is no three-body coupling and consequently no swap action.

Input			**Output**		
C	I_1	I_2	C	O_1	O_2
0	0	0	0	0	0
0	0	1	0	0	1
0	1	0	0	1	0
0	1	1	0	1	1
1	0	0	1	0	0
1	0	1	1	1	0
1	1	0	1	0	1
1	1	1	1	1	1

Table 5.1: Truth table of a Fredkin gate. C represents the control bit, I_1 and I_2 the input bits while O_1 and O_2 are the output bits.

It is evident that this kind of interaction scheme presents some critical point that must be tackled. First of all we have to consider that the $|ppp\rangle$ state is also coupled to other three-atom states like $|pss'\rangle$. In this case the global three-body coupling is smaller because of the symmetry of the configuration. In a linear configuration the atom in B is the most favourable to play the role of the relay atom because it will have the biggest intermediate couplings V_{dip1} and V_{dip2}. Even if the coupling $|ppp\rangle \leftrightarrow |pss'\rangle$ is smaller than the one for $|ppp\rangle \leftrightarrow |sp's'\rangle$, it could have a non-negligible effect on the fidelity of the swap operation. Another possible coupling which can reduce the fidelity of the quantum gate is the dipole-dipole coupling that drives the migration reaction like $p' + s \leftrightarrow s + p'$. Even in this case the symmetry of the system can be broken by an additional coupling affecting the fidelity.

5.5 Conclusions

In this chapter we have observed this new Borromean three-body FRET process for different principal quantum numbers. It has emerged that it is a general process like the two-body FRET. In principle it can be generalized to every atomic species that present a Förster resonance with an initial state with a total angular momentum $j > 1/2$. This last condition is necessary because the process requires an additional state close to degeneracy with the starting state. We thus require an initial state with at least two Zeeman sub-level.
We have proposed the generalization of this three-body interaction to a N-body interaction (Brunnian interaction). The observation of such a kind of general process would give a great improvement towards the understanding of many-body physics. It could also have interesting applications in the study of quantum energy transport in many-body systems in analogy with recent already cited experiments [Barredo et al., 2015, Günter et al., 2013] which exploit a two-body FRET for studying diffusive effect in a Rydberg chain or in a Rydberg gas. Moreover the three-body FRET finds a strong analogy in biology with the so called donor-bridge-acceptor or super-exchange configurations [Scholes, 2003].
Three-body FRET as well as two-body FRET can also be exploited for the realization of entanglement experiments and the implementation of quantum gates. We thus propose the realization of a heralded entanglement experiment using the relay atom as the herald. We finally propose to exploit the three-body interaction as the leading mechanism for the qu-bit swap in a Fredkin gate.

6 Van der Waals explosion of a 1 D chain of Rydberg atoms

In the previous chapters we have discussed two and three-body FRET processes. We have seen that FRET processes are due to a resonant dipole-dipole interaction between Rydberg atoms. In the investigation of these processes we focus our attention more on the dipole-dipole interaction effect on the internal degree of freedom of the Rydberg atoms. In our investigation we start from the hypothesis of a "frozen Rydberg gas" [Mourachko et al., 1998] where the mechanical effect due to the Rydberg-Rydberg interaction can be neglected. This approximation works very well when we consider a partial or even a fully blockade regime because the dipole-blockade radius imposes a minimum distance between two neighbouring Rydberg excitations. At this distances the interaction potential is flat, so repulsive or attractive effects can be neglected. When we instead consider an off-resonant Rydberg excitation we can excite two Rydberg atoms at distance where the van der Waals interaction is not flat and repulsion or attraction between atoms in non-negligible. A mechanical effect due to an attractive van der Waals interaction was observed in previous works [Amthor et al., 2007, Li et al., 2005]. There, the strong attraction between Rydberg atoms, due to an off-resonant Rydberg excitation, produces the ionization of one the two atoms by Penning collisions. Moreover the van der Waals repulsion between two Rydberg atoms excited with an off-resonant Rydberg excitation has been exploited for measuring the C_6 coefficient [Béguin et al., 2013, Thaicharoen et al., 2015]. In [Thaicharoen et al., 2015] a single atom imaging technique implemented with an MCP detector, as the one we describe in paragraph 3.3.3, is used for measuring the positions of the ions produced by the the field ionization. From the average pair correlation function of the atoms positions the authors estimate the initial atom-pair separation and the terminal velocity, which yield the van der Waals interaction coefficient C_6.
In this chapter we present a direct measurement, with a time of flight detection technique, of a mechanical effect due to a van der Waals explosion of a cluster of Rydberg atoms in analogy with a Coulomb explosion imaging technique largely used in molecular physics [Bocharova et al., 2008, Vager et al., 1989, Pitzer et al., 2013]. Coulomb explosion imaging are usually realized using MCP or COLTRIM [Bocharova et al., 2008,

Pitzer et al., 2013] which permits to acquire a time-of flight signal and also determine the impact position of the charged particles. The experiment has been realized at the Physics Departement of Physics of the University of Pisa. In our experimental set up we use a Channel Electron Multiplier (CEM) detector, also known as channeltron, which provides a time-of-flight signal of the Rydberg atoms and with an appropriate calibration of the ions arrival time we are able to determine the initial position of the atoms.

6.1 Off-resonant Rydberg excitation

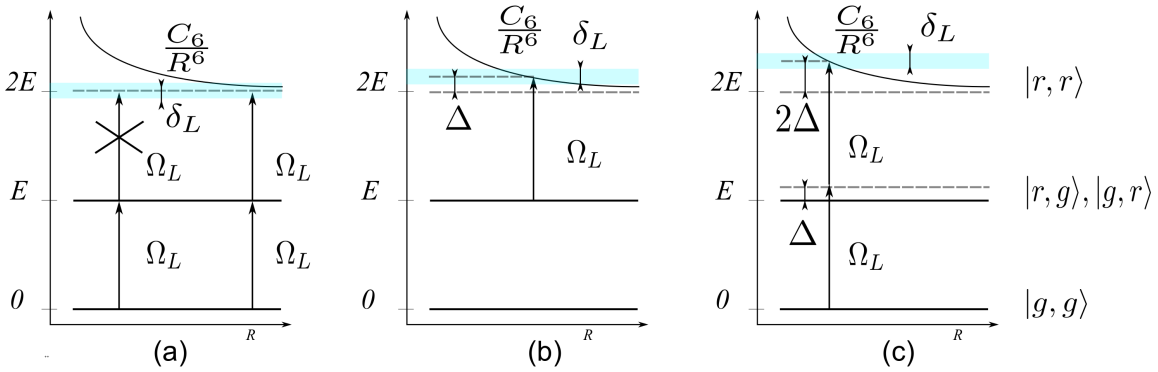

Figure 6.1: Schematic representation of the three possible excitation scheme of a pair of Rydberg atoms as a function of the reciprocal distance R. E and $2E$ are the energy of respective one and two Rydberg atoms without considering any kind of interaction. The dashed blue region corresponds to the laser linewidth δ_L. Δ is the detuning of the laser excitation with respect to the resonant transition. (a) On resonant excitation: the van der Waals interaction can inhibit the excitation of a second Rydberg atom at a distance closer than the Rydberg blockade radius. For an off-resonant excitation two paths are possible: (b) the presence of an already excited Rydberg atom can facilitate the excitation of a second Rydberg atom, or (c) two Rydberg atoms can be excited at the same time.

In the first chapter we have seen that if the interaction between two Rydberg atoms is strong enough the presence of an already excited Rydberg atom can suppress the excitation of a second one at a distance smaller than the so-called blockade radius. In

Fig.6.1(a) we report a scheme of an on resonant Rydberg excitation. When two atoms are close enough the van der Waals coupling between the two Rydberg atoms shifts the energy level of the two-atom state $|r, r\rangle$ and only one can be excited to a Rydberg level. On the other side when the two atoms are far apart they can be both excited to a Rydberg state.
If we instead consider an off-resonant excitation, the van der Waals interaction can on the contrary compensate the energy mismatch and facilitate the excitation of a pair of Rydberg atoms. Two atoms at a distance r from each other can be simultaneously excited if the detuning Δ of the laser excitation fulfils the following condition:

$$\frac{C_6}{r^6} = 2\hbar\Delta. \tag{6.1}$$

This is the case represented in Fig.6.1 (c). For $70S_{1/2}$ ^{87}Rb Rydberg state the $C_6 = h \times 0.86$ THz μm^6 [Walker and Saffman, 2008]. The two atoms thus undergo a van der Waals repulsion. If we consider an off-resonant excitation detuned by an amount $\Delta/2\pi = +10$ MHz, the condition of eq.6.1 is fulfilled for a pair of atoms at a distance $r = 5.92\mu$m. Typically for a Rydberg excitation characterized by a linewidth $\delta_L/2\pi = 0.7$ MHz, this is the excitation linewidth estimated for the experimental set up in Pisa, the Rydberg blockade is equal to $r_b = (C_6/\hbar\delta_L)^{1/6} = 10.5\mu$m. It is thus possible to overcome the limit due to the Rydberg blockade.
If a Rydberg excitation is already present the van der Waals interaction can then facilitate the excitation of a second Rydberg atom. In Fig.6.8(b) a scheme of this off-resonant excitation is presented. In this case the second Rydberg atom can be excited at a distance r which fulfils the condition:

$$\frac{C_6}{r^6} = \hbar\Delta. \tag{6.2}$$

This resonant condition is the opposite of the blockade effect, where the interaction suppresses the excitation process, allowing at most one single (collective) excitation within a blockade radius. Each new Rydberg excitation can facilitate the excitation of a new Rydberg atom at a distance equal to r_{fac} defined as:

$$r_{fac} = \left(\frac{C_6}{\hbar\Delta}\right)^{1/6} \tag{6.3}$$

. For a detuning of +10 MHz we obtain a $r_{fac} \approx 6.64\mu$m. Because of the finite laser linewidth of the Rydberg excitation δ_L we have an entire shell in which we can excite atoms to the Rydberg state. The thickness of the shell can be expressed as

[Lesanovsky and Garrahan, 2014]:

$$\Delta r_{fac} = \left(\frac{C_6}{\hbar}\right)^{1/6} \frac{1}{6} \frac{\delta_L}{\Delta} \tag{6.4}$$

which thus identify a facilitation volume:

$$V_{fac} = \frac{4\pi}{3}[(r_{fac} + \Delta r_{fac})^3 - r_{fac}^3] = \frac{2\pi}{3}\sqrt{\frac{C_6}{\hbar}}\frac{\delta_L}{\Delta^{3/2}}\left[1 + \frac{1}{6}\frac{\delta_L}{\Delta} + \frac{1}{108}\frac{\delta_L^2}{\Delta^2}\right] \tag{6.5}$$

An avalanche process can thus start leading to the formation of spatial structures known as aggregates. The geometries of the aggregates depend on the geometrical configuration of the Rydberg laser excitation. Focusing one of the laser of the Rydberg excitation to a waist dimension comparable to the facilitation radius it is possible to create the aggregate along the direction of the focused laser obtaining a 1 D aggregate like the one illustrated in Fig.6.2.

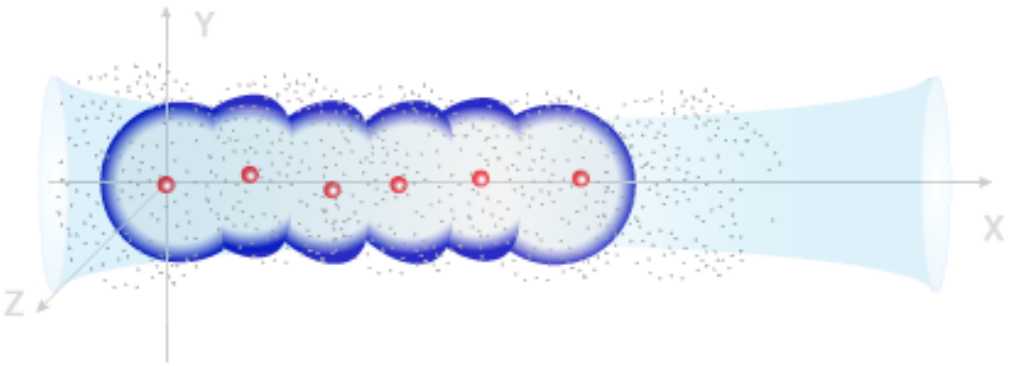

Figure 6.2: Sketch of 1 D Chain of Rydberg atoms. The laser excitation (shaded blue) is focused to a waist comparable to the facilitation radius r_{fac}. The dark blue shells represent the facilitation volume V_{fac} where a Rydberg excitation is possible. The limitation of the Rydberg excitation region obliges the aggregate to develop along the axis of propagation of the laser beam.

The dynamic of the formation of Rydberg aggregates has been theoretically proposed [Lesanovsky and Garrahan, 2014] and experimentally investigated in several

works [Malossi et al., 2014, Gärttner et al., 2013, Schempp et al., 2014, Valado, 2015]. The avalanche process has been characterized studying the increase in the normalized second central moment of the Rydberg number distribution, the Mandel Q parameter defined as:

$$Q = \frac{\langle \Delta N_e \rangle^2}{\langle N_e \rangle} - 1 \tag{6.6}$$

where N_e is the number of excitation and $\langle \Delta N_e \rangle^2 = \langle N_e^2 \rangle - \langle N_e \rangle^2$. In the case of negligible interaction between Rydberg atoms we can consider that each Rydberg excitation occurs independently from the others. In that situation the statistics of the Rydberg excitation can be described with a Poissonian distribution where $(\langle \Delta N \rangle)^2 = \langle N \rangle$ and $Q = 0$.
In the opposite case of a "fully blockade" regime where the excitation of a single Rydberg atom suppresses the excitation of any others we have that $\langle N_e^2 \rangle = \langle N_e \rangle^2$ and $Q = -1$ [Ates et al., 2006]. In the intermediate range of finite interaction the Q parameter can assume values between -1 and 0; this is the so-called sub-Poissonian regime [Mandel, 1979].
The avalanche process is instead a super-Poissonian process characterized by positive values of the Q parameter [Valado, 2015]. This behaviour is due to two aspects of the avalanche process: the low probability of exciting a Rydberg atom with an off-resonant laser excitation and the sudden interruption of the avalanche when no atoms are present in the next facilitation shell. The histograms of the counting distribution show a bimodal distribution [Valado, 2015].

6.2 Experimental setup

The experimental set up used in Pisa was first conceived for the study of a Bose Einstein Condensate of Rubidium atoms. A detailed description of the entire experimental set up can be found in [Ciampini, 2003, Radogostowicz, 2010]. Here we report a short description of the apparatus focusing the attention on the Rydberg excitation process and the Rydberg detection.

6.2.1 Vacuum chamber

We first start by describing the vacuum chamber of the experiment. The vacuum chamber is composed by two quartz cells of respective dimensions 80 mm ×47 mm ×47 mm and 70 mm ×24 mm ×18 mm. In the first cell there are two dispenser strips in which Rubidium is chemically bound to the surface. The dispensers

emit Rb atoms when an electric current heats the metal strip and induces chemical reactions. In this cell the ^{87}Rb atoms are loaded in a 2D MOT. The second quartz cell is placed at a distance of 20 cm and connected by a glass tube of inner diameter of 12 mm to the first one. The two cells are respectively connected to two ion pumps both by Varian. At one of the extremity of the glass tube, a thinner graphite tube of 5 mm of internal diameter and a length of 6 cm is placed in order to create a gradient of pressure between the two quartz cells. The first cell is kept at a pressure of 10^{-8} mbar while the second cell is kept at a pressure of 10^{-11} mbar. Thanks to this pressure gradient we are able to push the atoms loaded in the 2D MOT inside the second quartz cell where the atoms are cooled down and trapped in a 3D MOT.

6.2.2 Cooling down the atoms: 2D and 3D MOT

For the realization of the 2D and 3D MOT several laser sources are used in order to provide sufficient power to the trap and repumping beams. For that reason both cooling and repumping laser are locked in a master-slave configuration. We use diode laser (Mitsubishi ML60114R) external-cavity stabilized as master laser that is then injected in a slave laser (Sanyo DL-7140-201). After this first amplification stage the rempumping beam is first collected with an optical fiber and is directly sent to the vacuum chamber while the cooling laser is sent to an OPA (oscillator power amplifier) for a third step of amplification. The output of the OPA is then split in two beams that are the collected by two optical fibers and sent respectively to the two quartz cells. We finally obtain the cooling beams for the 2D and the 3D MOT with respective powers of 60 and 15 mW.

In Fig. 6.3 we highlight the two relevant transitions of the D2 line of Rb for cooling and trapping Rb atoms. The cooling transition is the $5S_{1/2}(F = 2) \rightarrow 5P_{3/2}(F = 3)$ transition at $\lambda = 780$ nm. We stabilize the frequency of the master with the well known saturated absorption technique using a Rb cell for the Doppler free spectroscopy. In Figs.6.4-6.5 we report respectively the transmission spectra for the transitions $F = 2 \rightarrow F'(= 1, 2, 3)$ and $F = 1 \rightarrow F'(= 1, 2)$. We lock the master laser on the crossover peak 2-3. The repumping laser is then locked on the peak of $5S_{1/2}(F = 1) \rightarrow 5P_{3/2}(F = 2)$.

For the 2D MOT we use a couple of counter-propagating beams with a waist of 12 mm. The laser frequency of the beams is detuned by $\delta = 2.4\Gamma$ from the $5S_{1/2}(F = 2) \rightarrow 5P_{3/2}(F = 3)$ transition, where $\Gamma/2\pi = 6.065$ MHz and represent the natural linewidth of the $5P_{3/2}(F = 3)$ level. For the 2D MOT a linear quadrupole

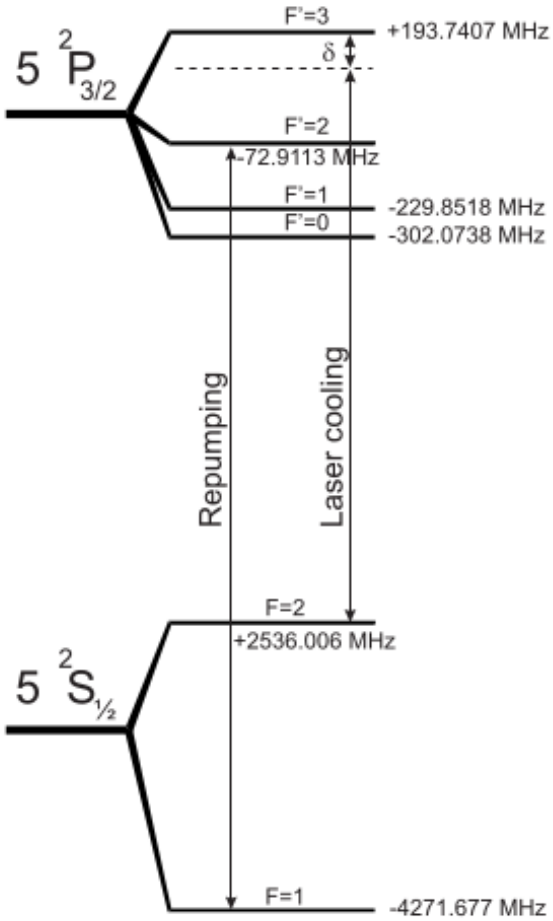

Figure 6.3: Scheme of D2 line of 87 Rb. The laser cooling and repumping transition are respectively labelled with black arrows. δ is the detuning of the trapping laser.

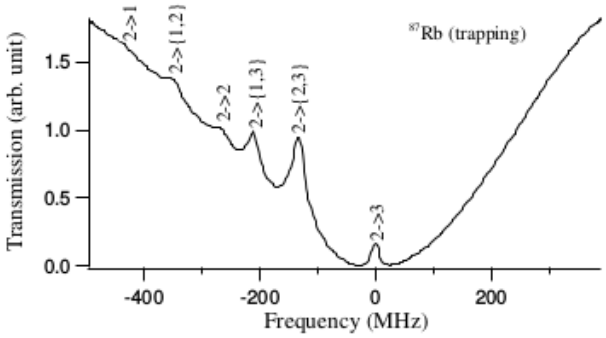

Figure 6.4: Transmission spectra for the transitions $F = 2 \rightarrow F'$ of 87 Rb for the cooling transition. The notation $F \rightarrow \{F_a, F_b\}$ indicates a cross-over.

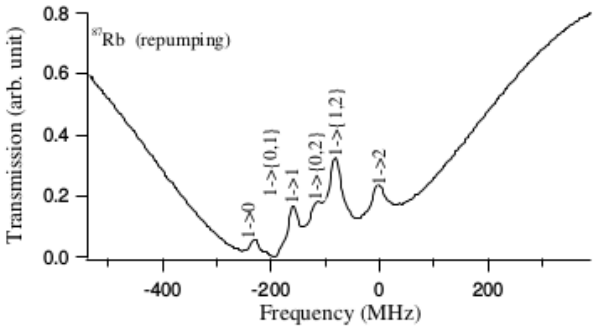

Figure 6.5: Transmission spectra for the transitions $F = 1 \rightarrow F'$ of 87 Rb for the repumping transition. The notation $F \rightarrow \{F_a, F_b\}$ indicates a cross-over.

field is generated by two couples of coils in an anti-Helmoltz configuration two by two. The atoms are cooled in two dimensions, in a cigar shape cloud. In the same direction as the long axis of this cloud, a pushing beam is sent in order to transfer the atoms into the second cell where the atoms are trapped in a standard 3D MOT. The 3D MOT is composed by three pairs of counter-propagating beams with a waist of 8 mm and power of ~ 5 mW on each direction. In this case the laser frequency of the beams is detuned by $\delta = 2.9\Gamma$ from the $5S_{1/2}(F = 2) \rightarrow 5P_{3/2}(F = 3)$ transition. We obtain a frequency stabilized up to 200 kHz. A couple of coils in an anti Helmoltz configuration is necessary to apply the quadrupole field necessary for the trapping. The quadrupole field has a gradient of 12.2 G cm^1 along the coils axis parallel to the z axis (see Fig. 6.6 for the Cartesian direction). The magnetic field gradient is two times smaller along the other direction. Three additional couples of coils have been mounted along the three axes x, y and z in order to compensate the earth magnetic field as well as spurious magnetic field due to the ionic pump. The magnetic field applied is of the order of 0.5 G. These three additional coils also allow to displace the zero of the magnetic field and thus the center of the MOT. We will see in the next paragraphs that the displacements of the center of the MOT results also in a shift of the ions arrival time. These additional coils will be useful for the calibration of such shift.

We monitor the 3D MOT with two CCD cameras. One camera is used to check the presence of the MOT. The fluorescence signal due to the absorption and emission cycle is collected and visualized on a TV screen. A second camera, placed along the y axis with a higher resolution, is used for absorption imaging. Thanks to a previous calibration of the camera [Ciampini, 2003], we can get from the integrated profiles of the fluorescence of the MOT along the x and the z directions an estimation of the dimensions of the MOT in these two directions and an estimation of the number of atoms inside the trap with an uncertainty of about 20 %. The resolution of the CCD camera has been estimated to be 6.5 μm. This estimation takes into account the finite dimension of the pixel of the camera and the diffraction limit that has been estimated to be 5.7 μm for our experimental configuration [Ciampini, 2003]. We can also evaluate the peak density of our MOTs using the relation:

$$n_{peak} = \frac{N_{atoms}}{\sigma_x \cdot \sigma_z \sqrt{\sigma_x \cdot \sigma_z}} \tag{6.7}$$

where σ_x and σ_z are the dimensions of the MOT respectively along the x and the z directions, N_{atoms} is the number of atoms in the MOT. We finally obtain a sample of Rubidium atoms with a typical peak density of $10^{10} - 10^{11}$ atoms per cm^3 and an estimated temperature of T $\sim 150\mu$K consistent with the Doppler cooling limit. We

are able to control the dimension of the MOT by changing the electric current in the two anti-Helmoltz coils of the 3D MOT. The typical dimension of the MOT we use in the experiment range between 30 μm to about 200 μm.

6.2.3 Two-photon Rydberg excitation

We excite the Rydberg level 70 $S_{1/2}$ with a two-photon excitation. The first step of the Rydberg excitation is the transition $5S_{1/2}(F = 2) \rightarrow 6P_{3/2}(F = 3)$ at $\lambda = 421$ nm. For this transition we use a $\lambda = 842$ nm MOPA laser TA100 from TOPTICA which is sent to a doubling cavity SHG 1004 also from TOPTICA, giving an output power at $\lambda = 421$ nm of around 60 mW. We detune the laser frequency from the resonant transition as we can see in Fig.6.7. This detuning we label with δ permits to reduce the spectral width of the Rydberg excitation. It is known that a resonant excitation of $6P_{3/2}(F = 3)$ will broaden the Rydberg laser excitation because of the short-lifetime of this intermediate level. With a laser excitation detuned of an amount ranging between +300 MHz and +2 GHz the population of the intermediate level $6P_{3/2}(F = 3)$ is negligible and we still have a two-photon Rabi frequency of $\approx 1 - 2$ MHz. This detuning allows also to avoid spurious effect like the direct two-photon ionization of the ground state which can affect the detection of the Rydberg atoms. We control the laser beam power sent to the atoms with an AOM modulator. We are able to finally send up to 30 mW on the atoms.
The second step is the transition $6P_{3/2}(F = 3) \rightarrow nS$ at $\lambda = 1013nm$. We use a DL100 diode laser from TOPTICA injected in a TIGER laser from SACHER. At the output of the TIGER laser we obtain a power of 160 mW. In the experiment I have participated, the Rydberg level we have excited was the $70S_{1/2}$. However it is possible by adjusting the laser frequency of the laser diode excite different Rydberg level ranging between $n = 30$ to $n = 120$.
The stabilization in frequency of the Rydberg excitation lasers is done using a Fabry-Perot interferometer (TOPTICA FPI100). Both the 842 nm and the 1013 nm beams are coupled into the Fabry-Perot cavity together to a reference laser (of $\lambda = 780$ nm), locked with saturated absorption technique on one of the peak of Fig.6.4. The peak we choose is not of essential importance since we use it as a reference for the cavity.
The Fabry-Pérot Interferometer we use is a piezo-electrically scanned device which combines a high finesse F, (F$\sim$ 120 for the 421 nm laser [Radogostowicz, 2010]) with the flexibility of using it as a stable reference cavity. A Labview program provides the interface to control the stabilization of the Rydberg excitation lasers. This is done by modulating the length of the FP cavity over its full free spectral range with a frequency of 200 Hz. On the transmission signal of the Fabry-Pérot, four transmission peaks are

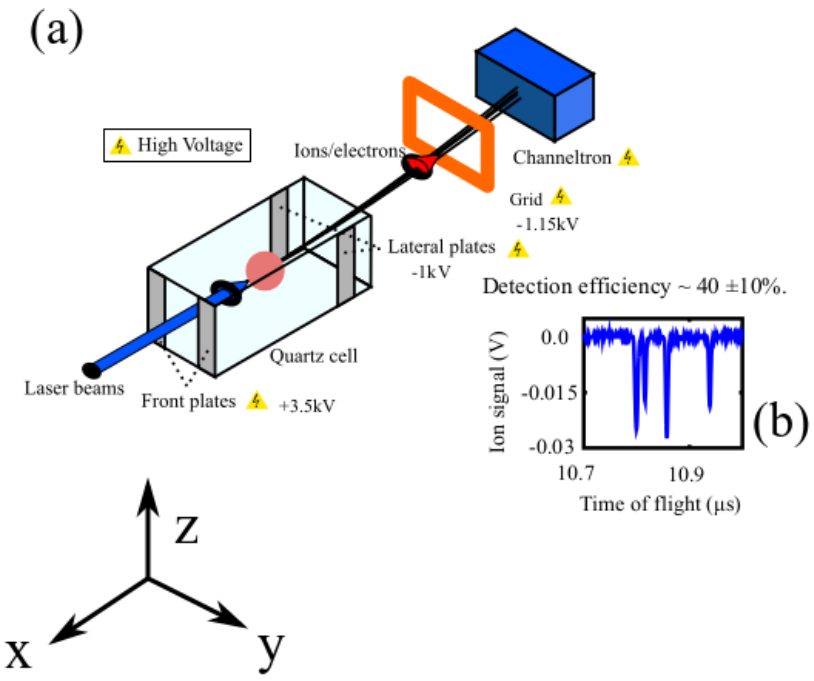

Figure 6.6: (a)Simple sketch of the experimental apparatus used for the detection of the Rydberg atoms. The Rb atoms are cooled down and trapped inside the quartz cell where they are subsequently excited to a Rydberg level. The ionization field is applied by the front and the lateral plates. An additional grid at high voltage drives the ions to the channeltron where they are detected. (b) Typical time of flight signal of detected Rydberg atoms. The signal is collected with an oscilloscope.

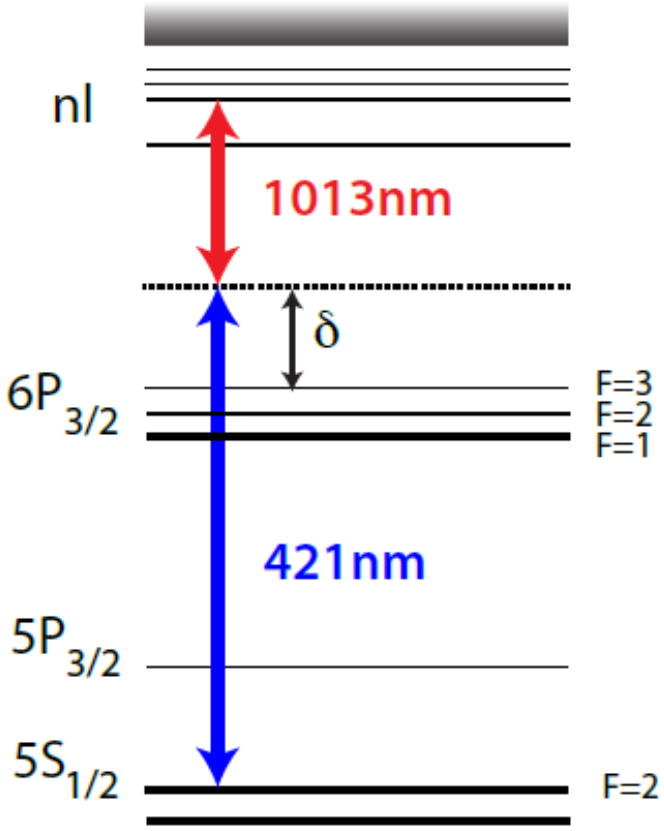

Figure 6.7: Two-photon excitation scheme for the Rydberg excitation. The first step is a blue laser at $\lambda = 421$ nm. δ represents the detuning, ranging between 300 MHz to 2 GHz, of the laser excitation from the resonant transition $5S_{1/2}(F = 2) \rightarrow 6P_{3/2}(F = 3)$. The second step is an infra-red laser at $\lambda = 1013$ nm.

identified, two of them correspond to the Rydberg excitation lasers and the other two peaks belong to the reference laser. These two latter peaks allow to determine a well defined relative frequency scale for the position at which other peaks appear. The program measures the relative positions of the transmission peaks and compares them to the reference position. An error signal obtained from the transmission signal is then sent to a PID110 TOPTICA module used to stabilize the laser frequency on the chosen value. The Fabry-Pérot cavity has a free spectral range of 1 GHz and the main task of the Fabry-Pérot is to stabilize the spectral lines against thermal drift during the measurement. In order to stabilize the temperature of the Fabry-Pérot cavity it has been placed inside an isolated wooden box controlled by a heating system. Using this configuration the lasers remain locked for hours.
The excitation of Rydberg atoms can be realized with two different geometrical configurations which are sketched in Fig.6.8. These two geometrical configuration are obtained splitting the blue laser beam in two beams. One beam is collected by an optical fiber. At the output of the fiber the beam is focused with a lens of focal length $f = 200$ mm to a beam waist of $\omega = 6\mu$m. The IR beam is then collimated with a beam waist of 110 μm and cross the blue beam tilted with an angle of 45°. We thus obtain a Rydberg excitation region limited by the dimension of the blue beam that can be considered a 1D configuration. This is the case of the scheme in Fig.6.8(a). The second possible configuration is instead obtained superposing the remaining blue beam with the IR beam. In this case the Rydberg excitation region is limited by the collimated blue which has a beam waist of 40 μm. This is the case of the scheme in Fig.6.8(b). The duration of the Rydberg pulse excitation can range between 1 to 100 μs depending if we use an on resonant or an off resonant excitation.

6.2.4 Rydberg detection

Rydberg atoms are ionized and detected by a channeltron with a well known time-of-flight technique analogous to the one presented in chapter 3. Since we only excite the 70 $S_{1/2}$ no selective field ionization technique are necessary. The ionization pulse is directly applied without any ramp of ionization to the electrodes placed on the quartz cell. However the ionization is not instantaneous since we have to consider a raising time of the order of $\sim$ 100 ns of the voltage applied to the electrodes. In Fig. 6.6 we present a sketch of the experimental set up used for the ionization of the Rydberg atoms. The frontal plates are kept at + 3,5 kV while the voltage applied on side ones is $\sim$ 1 kV and they remain switched on during 4,3 μs in order to avoid charging up the cell and the creation of an extra spurious electric field. The emitted ions are then guided towards the detector, a Channel Electron Multiplier (CEM) KKBL510,

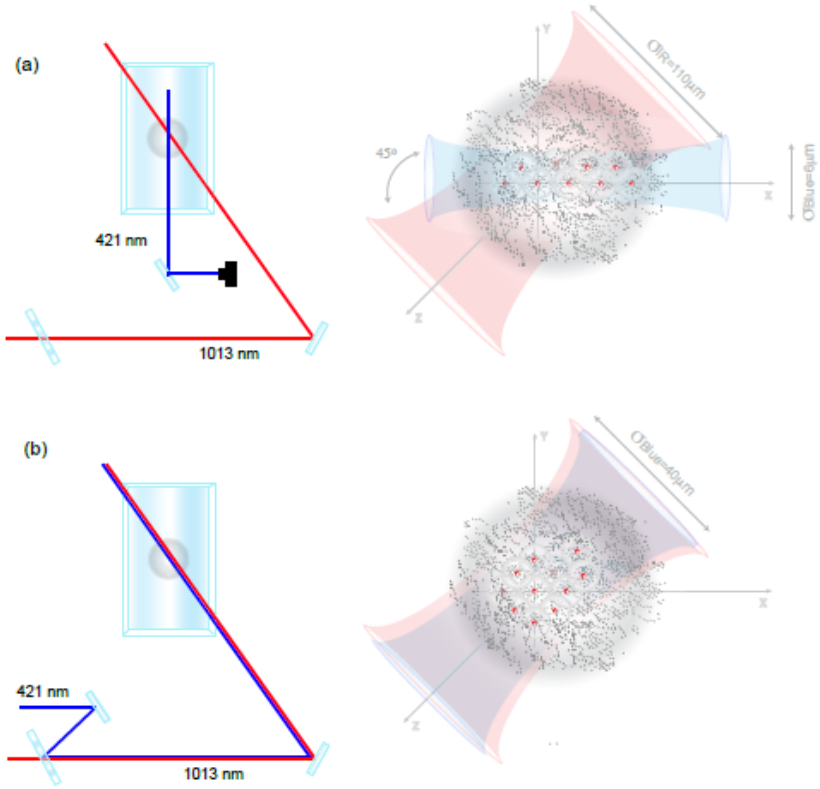

Figure 6.8: (a)1 D configuration: the blue beam is focused to a beam waist $\omega = 6\mu$m and the IR laser is incident with an approximative angle of 45°; (b) the blue and the IR beam are superposed.

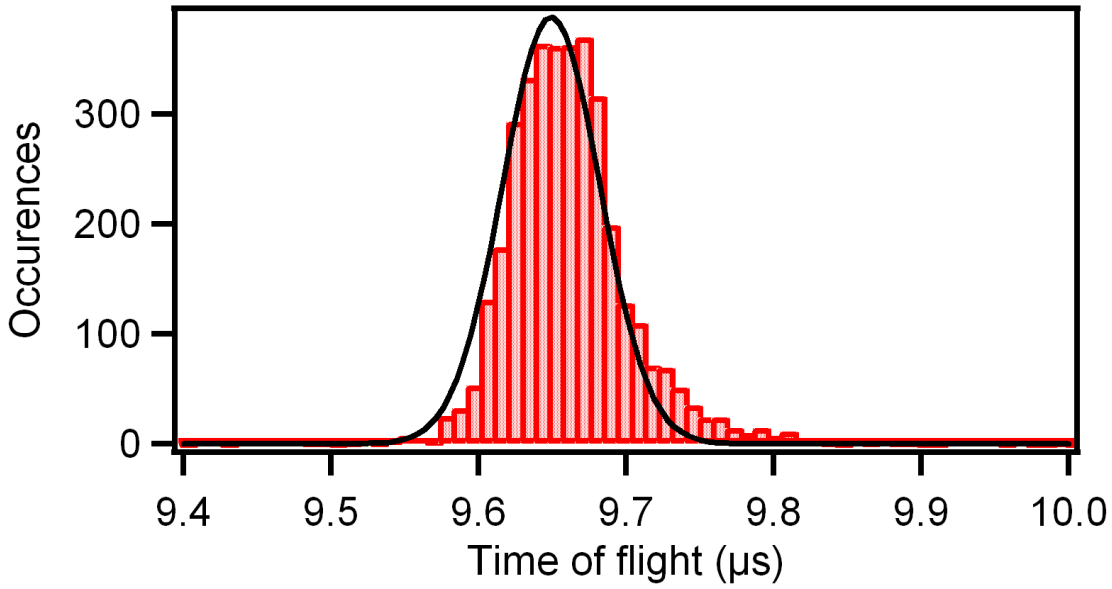

Figure 6.9: Histogram of the arrival times of the ions for a $\langle N_{Rydberg} = 9.17 \rangle$. This measure has been taken with 400 shots.

located around 15 cm from the center of the quartz cell. An additional grid kept at $\sim$ 1.15 kV is used to guide the ions towards the CEM. The channeltron has an internal gain determined by a potential, we set it to the maximum, $\sim 2,5$ kV, in order to ensure the maximum detection efficiency. Finally, the output signal is acquired on the oscilloscope (a LeCroy WaveRunner). The acquired signal is then analyzed with a LabView program in order to obtain the number of detected ions and the arrival time with an accuracy better than 5 %.
Fig.6.6(b) shows the typical signal of the arrival time of the ions given by the oscilloscope. The procedure of excitation and detection of Rydberg atoms is repeated at a rate of 4 Hz. This limitation of the acquisition rate is related to the fact that for higher rate a polarization of the quartz cell leads to the induction of spurious electric field. We usually acquire a number of shot measurement ranging between 200-400. Each shot contains the number of detected ions with the relative arrival times. The LabView program also calculates the mean number of detected ions, the standard deviation and the Mandel Q factor.
In Fig.6.9 we plot an histogram of the arrival times of ions for a mean number 9.17 of Rydberg atoms. The arrival time distribution can be very well fitted with a guassian

curve. From the gaussian fit we obtain the mean value of the gaussian and the standard deviation. These two parameters are useful to quantify the mean arrival times of the ions and the dispersion of the arrival times. In the next paragraph we will see how the center of the gaussian distribution as well as the standard deviation can be used for extrapolating information on the positions and the interaction between Rydberg atoms.
The detection of the ions presents some limitation due to the oscilloscope resolution and the channeltron detection efficiency. The limited oscilloscope resolution oblige us to work with a reduced number of Rydberg atoms. We are able to resolve two different arrival times for two different ions if they are at least separated by 10-20 ns in time. Above a certain number of ions (typically 40) the arrival times of the ions are too closely spaced, preventing us from counting the peaks. For that reasons the experiments can be performed for a number of detected ions below 40 in order to avoid saturation effects.
When we consider the detection efficiency of the ionization of Rydberg atoms we to take into account the losses of ions as well as the intrinsic detection efficiency of the channeltron detector. The overall detection efficiency for this set up, $\nu \approx 35 \pm 10\%$, has been reported in details in [Viteau et al., 2010]. In that case, the determination of the detection efficiency consisted in comparing, during a photoionization process, the number of detected ions with an evaluation of the atomic loss from the cloud performed for different atomic densities and laser power values. For the experiments reported in this Thesis, a detection efficiency of $\nu \approx 40\%$ has been considered. Besides, except for the cases in which it is explicitly indicated, we show observed values, both for the mean number of ions ($\langle N_{obs} \rangle = \nu \langle N \rangle$) as well as for the standard deviations ($SD_{obs} = \nu SD$)

6.3 Experimental Characterization of a van der Waals explosion

6.3.1 Coulomb expansion

The investigation of the mechanical effect due to a van der Waals repulsion in a cluster of Rydberg atoms requires a detection apparatus capable of measuring the position of the atoms at different times. Since we detect Rydberg atoms by field ionization, the additional investigation of the effect due Coulomb repulsion is necessary.
The detector we use, a CEM, is not sensitive to impact positions as an MCP but only to the different arrival times of the ions. Nevertheless we can find a direct relationship

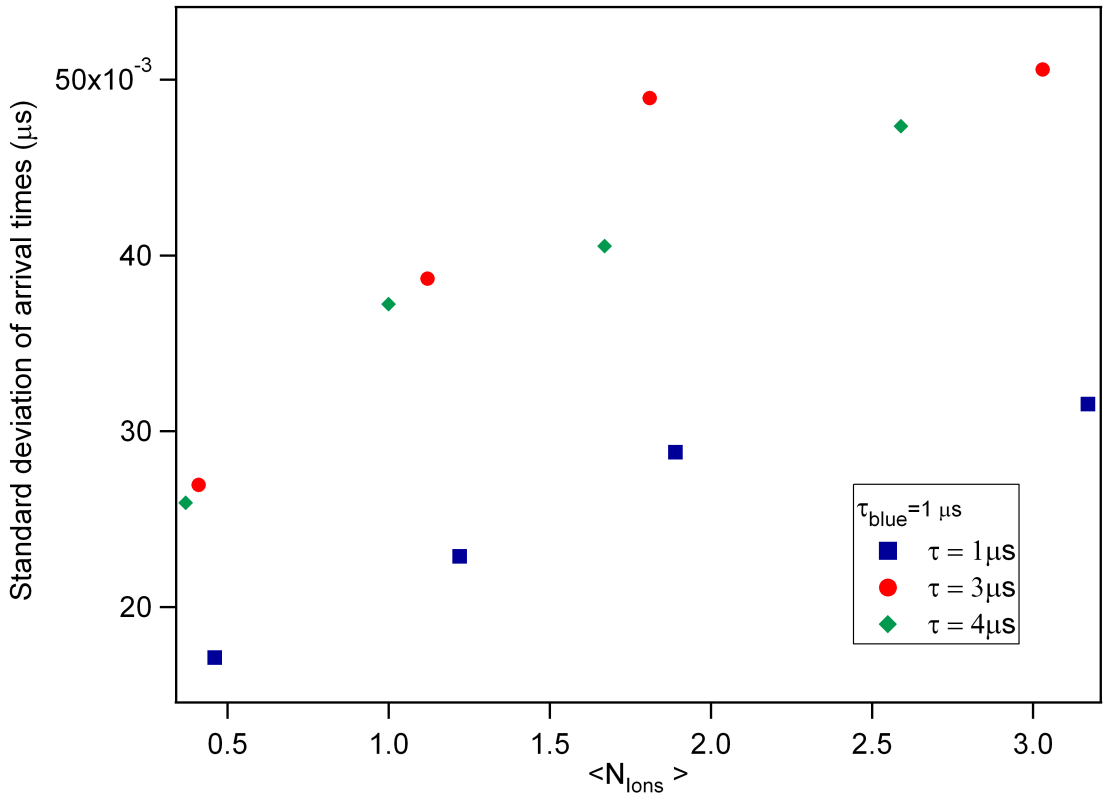

Figure 6.10: Evolution of the distribution width of the arrival time for different $\langle N_{ions} \rangle$ and different delay τ between the ionization and the acceleration of the ions.

between the arrival times and the initial position of the atoms at the moment they are ionized and thus accelerated towards the detector. Such calibration consists in ionizing a particle at a known position in space and looking for its arrival time: once we change the initial position, the particle should experience a variation in its arrival time. We measure the initial position of the ions with a CCD camera we use for measuring the MOT size. We assume as the starting position of the ion the center of the gaussian shaped density profile of the MOT, since the density reflects the probability to create an ion at that position.
In order to map the arrival time of the ions on the detector we decided to study the case of ions produced by the photo-ionization of the $5P_{3/2}$ level; when the trapping beams of the magneto optical trap is on, the population of the $5P_{3/2}$ level cannot be

neglected and the atoms in that level can be ionized with a single blue photon at 421 nm. We choose not to use ions produced by field ionization of the Rydberg atoms because the Rydberg blockade effect will affect the position at which the Rydberg atom can be created. Moreover in this case the ionization and the acceleration of the ions coincide so a study of the temporal evolution of a Coulomb expansion is not possible. The ions produced with a photo-ionization of $5P_{3/2}$ can be accelerated in a second time. This allows us to create ions in the MOT and observe the Coulomb expansion simply by waiting an amount of time τ between the ionization and the beginning of the acceleration.
We are able to control the number of ions by changing the power of the laser beam with the AOM used for switching the blue beam. The ions are created switching the blue laser beam for 1μs and after that they are accelerated by the same external electric field we use for the ionization of the Rydberg atoms. The ions are then detected by the channeltron. We repeat this cycle 200 times in order to have a sufficient statistics to determine the mean arrival times of ions and the dispersion of the arrival times. In Fig.6.10 we plot the standard deviation of the arrival times for different ions mean number and different values of τ. The standard deviation of the arrival times is obtained from an histogram plot like the one of Fig. 6.9 we fit it with a gaussian function. As we increase the mean number of ions the arrival time distribution gets broader because of a stronger Coulomb repulsion. When the expansion time τ passes from $\tau = 1$ μs to $\tau = 3$ μs the distribution of the arrival times almost doubles, while when we pass from $\tau = 3$ μs to $\tau = 4$ μs, the two curves are almost overlapped. This saturation can be explained by considering that the ions that most repel each other fall out of the acceptance region and do not hit the sensitive window. We thus loss information on the Coulomb expansion for the longer τ.

6.3.2 Time of flight mapping

We immediately see that the Coulomb repulsion cannot be neglected in the calibration of the ions arrival times. For this reason in order to reduce the aberration effect due to the Coulomb repulsion between ions we keep the mean number of ions at about $\langle N_{ions} \rangle < 1$, in order to have only one ion on average per shot, and we reduce the expansion time to the minimum value of 1 μs. We map the ion time of flight for different MOT position's along the three axis x, y and z (see the axis coordinate definition in Fig.6.11). In each case we move the MOT only along one direction keeping the position on the other two axes fixed. We then plot a histogram of the arrival times, like the one in Fig.6.9, for each MOT's position. We fit the arrival times distribution

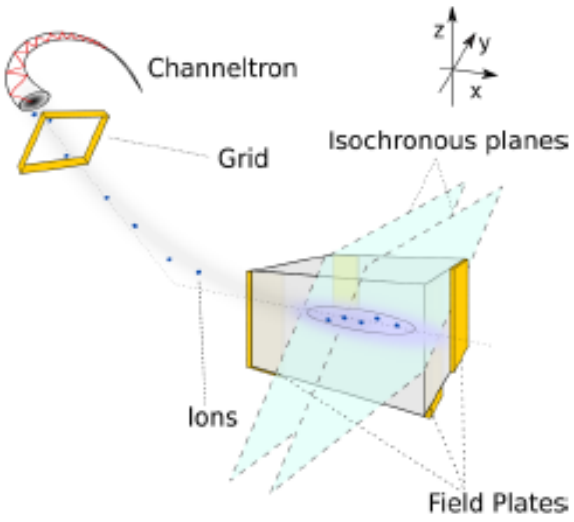

Figure 6.11: Cold atoms in a MOT are excited to Rydberg states in an elongated interaction volume (continuous ellipse), and subsequently expand due to the vdW repulsion. After a variable free expansion time they are field ionized by switching on the field plates. Finally the ions (blue dots) are electrically accelerated through a grid towards a channeltron. The isochronous planes defined in the text are schematically represented.

with a Gaussian fit obtaining the center and the standard deviation. In Fig.6.12 we report the center of the time of flight distribution moving the MOT along the x-axis (blue square), z-axis (red circle) and y-axis (green triangle). We move the MOT's center using three different compensation coils. At each time we adjust the alignment of the MOT lasers and of the blue beam in order to always target the center of the MOT. We fix a MOT sizes $\sigma_x \approx 120\mu$m and $\sigma_z \approx 90\mu$m, assuming $\sigma_x \approx \sigma_y$ because the magnetic field gradient along the x and y-axis are the same [Valado et al., 2013]. Because of the reduced dimension of the blue beam waist 6 μm compared to the MOT size we can assume that the ion is created at the center of the MOT once we have well aligned the blue beam. The center and the sizes of the MOT along the x and z-axis have been measured fitting the intensity profile acquired by a CCD camera oriented along the y-axis with a gaussian fit.

Since we are not able to measure the size and the position of the MOT along the y-

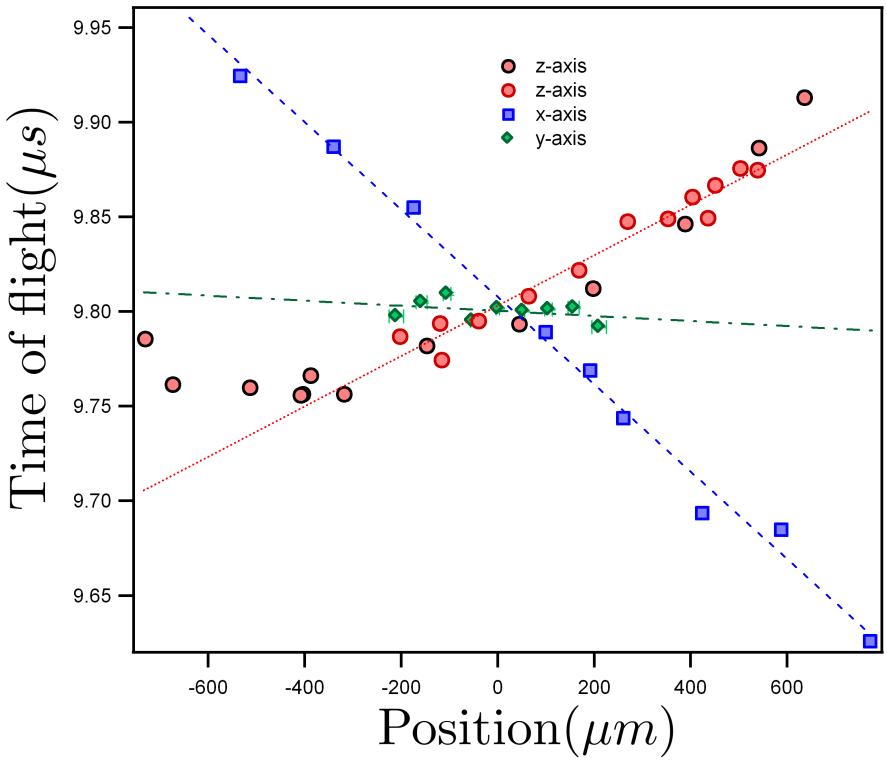

Figure 6.12: Calibration of the arrival time distributions at the channeltron. The center of time of flight distribution is plotted as a function of the position of the center of the MOT along the z-axis (red circle), x-axis (blue square) and y-axis (green diamond) with respective linear fit (red dotted, blue dashed and green dashed dotted lines). In each case, the MOT was centred at 0 in the other two directions. The error bars are smaller than the size of the data symbols. The red circles with black borders correspond to a variation in the z-position for a fixed $x = 460 \pm 5\mu$m where the arrival times were corrected using the x-axis calibration.

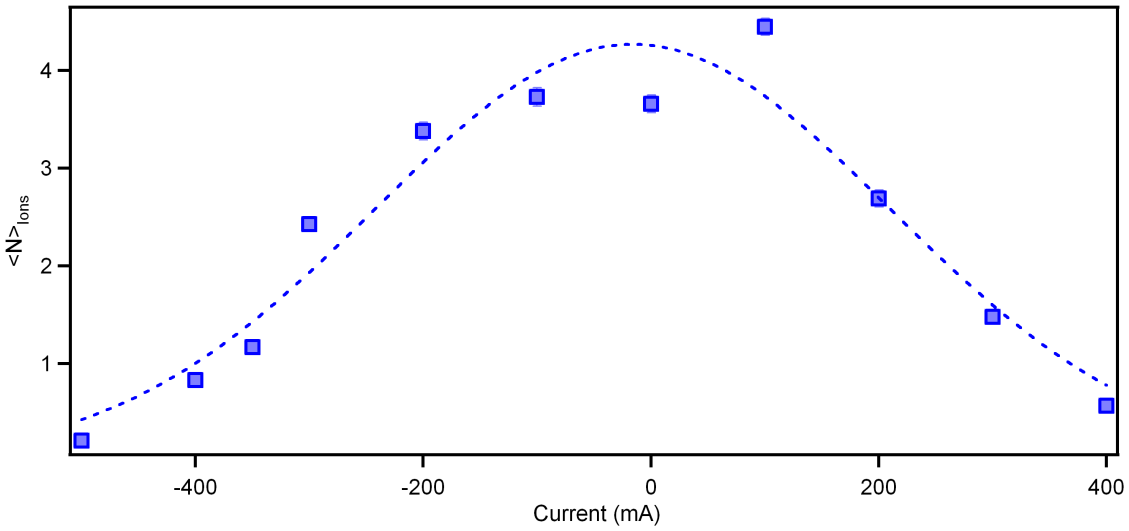

Figure 6.13: Current calibration for the displacement along the y-axis. The mean number of the detected ions is plotted varying the current in the compensation coil.

axis	coefficient label	numerical value
x	α	$(-2.31 \pm 0.08) \times 10^{-4} \frac{\mu s}{\mu m}$
z	β	$(1.34 \pm 0.07) \times 10^{-4} \frac{\mu s}{\mu m}$
y	γ	$(-1.34 \pm 1.26) \times 10^{-5} \frac{\mu s}{\mu m}$

Table 6.1: List of slope coefficients for the calibration of the arrival times.

axis, the calibration along this axis has been realized in an indirect way. We first need to calibrate the displacement along the y-axis. We keep the blue beam fixed in space and we move the MOT along the y axis changing the current of the compensation coil. In Fig.6.13 we plot the mean number of detected ions for different values of the current applied to the compensation coils. Since the number of ions is proportional to the local density of the MOT, we obtain a gaussian profile which corresponds to the one of the MOT along the y direction. Comparing $\sigma_y = 118 \pm 3\mu$m, that we assume to be the dimension of the MOT, with the σ obtained with a gaussian fit we obtain a calibration coefficient of $0.53 \times 10^{-3} \pm 0.04 \times 10^{-3}$ m A^{-1} we use to estimate the displacement of the MOT along the y-axis.

We fit the experimental points of Fig.6.12 with three different linear fit. We obtain

the three slope coefficients summarized in table 6.1. We arbitrarily choose the origin of the axis in order to have a zero intercept for both the three fits. No significant variation of the time of flight can be observed moving the MOT along the y-axis compared to the effect of a displacement along x or z. On the other side we observe a non negligible shift of the arrival time moving the MOT along the x and z axis. We verify the linearity measuring two set of data along the z-axis for two different fixed x positions. In Fig. 6.12 we plot two different series of data for the calibration along the z axis characterized by two different position along the x-axis. One series is taken for $x = 0$ (red circle with red edge) while the second for $x = 460 \pm 5\mu$m (red circle with black edge) and then translated taking into account the bias on the arrival time due to the x-position. We can see that the two sets of data well superposed confirming that the arrival times linearly depend on the position along x and z without any cross terms.
The two slope coefficients α and β allow us to determine a series of isochronous planes in space. Theses series of planes is described by the following equation:

$$t = \alpha x + \beta z \tag{6.8}$$

where t represents the arrival time of the ions. Our detection process projects the positions of ions created in an isochronous plane onto a particular arrival time on the channeltron. All the atoms that belong to this plane have the same time of flight to reach the CEM detector. The calibration we perform turns out to be one dimensional, so we can actually relate each arrival time not to a point but rather to a locus of points in space described by eq. 6.8. A sketch of these isochronous planes is presented in Fig.6.11. They contain the y-axis and they are tilted of an angle of $59.9° \pm 1.5°$ with respect to the x-y plane as we can easily obtain from eq.6.8. From equation 6.8 we can obtain with some simple geometrical consideration a coefficient of proportionality between the temporal delay $\Delta t = t_2 - t_1$ and the distance Δs between to isochronous planes:

$$\Delta t = \sqrt{\alpha^2 + \beta^2}\Delta s. \tag{6.9}$$

This final relation allows us to find a correspondence between the arrival time of the ions and their initial position. With the values on table 6.1 we obtain $\sqrt{\alpha^2 + \beta^2} = (2.64 \pm 0.08) \times 10^{-4}\mu$s/$\mu$m.

6.3.3 Off-resonant excitation: seed technique

We now want to describe the so called "seed" technique that has been developed in Pisa for the excitation of Rydberg atoms with an off-resonance laser excitation. Previous

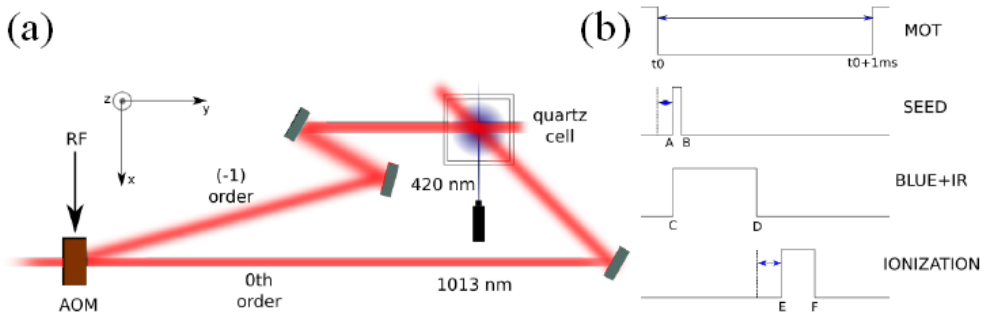

Figure 6.14: (a) Sketch of the optical alignment for the creation of an avalanche process with a seed technique in a 1 D geometry. The IR laser beam is split in two beams by the AOM. The order -1 is used for the on resonant Rydberg excitation while the order 0 provide the off resonant excitation. The blue beam is focused at the center of the MOT. (b) Time sequence of the creation of an avalanche process. During the excitation the MOT laser are switched off. The seed beam is switched on for a duration of ≈ 500 ns, while the blue beam is switched on for 100 μs. The zero order is always on. We ionize the Rydberg atoms with a variable delay.

works have been realized using an off-resonant excitation technique [Amthor et al., 2007, Malossi et al., 2014, Schempp et al., 2014, Teixeira et al., 2015] where a Rydberg excitation detuned from resonance few MHz has been used to investigate the effect of the van der Waals interaction. However the small detuning achievable only by slightly detuning the Rydberg excitation laser limits the strength of the van der Waalls forces we can obtain. A new technique allowing to produce off-resonant Rydberg excitation with a larger detuning and a consequent stronger van der Waals interaction has been developed in Pisa. The novelty introduced by this technique consists in the exploitation of an initial Rydberg excitation with an on resonant laser excitation. The excitation occurs in two steps: first we have the excitation of a single Rydberg atom with an on resonant excitation and then the switch to an off-resonant excitation. The excitation of single Rydberg atom, a "seed", thus facilitates the avalanche process that can only start if a Rydberg atom is present.
In Fig.6.14(a) we present a sketch of the optical set up used for the excitation of an avalanche process. In order to switch from an on resonant to an off resonant Rydberg excitation we use an AOM placed along the optical path of the IR laser. We use the -1 diffraction order for the excitation of the seed atom, so we adjust the laser frequency of the IR laser in order to have the order -1 resonant to the Rydberg excitation. We call it the "seed beam". On the other side the 0 order is blue detuned an amount equal to the RF frequency used to modulate the AOM.
We typically work with RF frequency ranging between +55 and +80 MHz. The limit of 80 MHz corresponds to the optimum operating frequency for the AOM. For higher detuning the facilitation region, described by eq. 6.4 gets narrower so the probability to find an atoms inside the facilitation region decreases and the activation of the avalanche process becomes less and less probable. For that reason we do not try for higher detuning than 80 MHz. The lower limit of + 55 MHz is mostly related to technical reasons: for lower RF frequency the diffracted power dramatically falls and no Rydberg excitation is possible.
In Fig.6.14(b) we sketch the time sequence of the Rydberg excitation and detection. The entire Rydberg excitation (on and off-resonant excitation duration) is determined by the blue beam which is switched on for 100 μs. At the beginning of the excitation the "seed beam" is switched on for a time ranging between 300-500 ns. The duration of the "seed pulse" has been chosen in order to have a mean number of seed ≈ 1. We choose to work with a single seed excitation because in the case of more than one seed, each seed can start an avalanche process and the presence of more than one chain of Rydberg atoms can lead to an artificial broadening of the arrival time distribution due not to the van der Waals repulsion but to the excitation of two or more different Rydberg chains in different places of the MOT. Once the seed pulse is switched off, only

the blue beam and the zero order of the IR laser are sent to the atoms. The duration of the pulse has been chosen because it has been observed that for this duration the total number of Rydberg atoms of the chain achieve a stationary value [Valado, 2015]. In Fig.6.14 we report a scheme of the optical set-up for the excitation of the seed atom and the avalanche process. The zero order of the IR makes an angle of 45° with the blue beam. Approximating the blue beam and the zero order IR beam with two cylinders of respective radius 6 and 110 μ, and the MOT as a ellipsoid with three gaussian profiles $\sigma_x = \sigma_y = 120\mu$m and $\sigma_z = 90\mu$m along the three Cartesian directions we estimate an excitation volume of $\approx 10^{-7}$ cm^3 for the off-resonant excitation. We usually obtain a cluster of a mean number of 10-12 Rydberg atoms.

6.3.4 van der Waals expansion

In the previous paragraph we have seen how it is possible to generate an avalanche process for the formation of a 1 D chain of Rydberg atoms. Now we want to discuss the experimental results we have obtained studying the spatial expansion of the 1 D chain. Since the Rydberg atoms are excited at a distance smaller than the dipole blockade radius they repel each other because of a van der Waals interaction. The amount of the interaction is equal to the detuning of the off-resonant laser excitation from the on resonant Rydberg transition. We compare the expansion of a chain of ≈ 12 atoms created with two different off-resonant excitation respectively detuned by $\Delta/2\pi = +80$ MHz and $\Delta/2\pi = +55$ MHz with the expansion of an ensemble of ≈ 12 Rydberg atoms excited with an on resonant laser excitation. Using equations 6.3-6.4 we can calculate the distance with the respective range of incertitude between two successive Rydberg excitations. We obtain for $\frac{\Delta}{2\pi} = 80$ MHz and $\frac{\Delta}{2\pi} = 55$ MHz the respective facilitation radius $r_{fac} = (4.70 \pm 0.01)$ μm and $r_{fac} = (5.00 \pm 0.01)$ μm while we estimate a dipole blockade radius for a laser linewidth of $\delta_L = 0.7$ MHz $r_b = (10.5 \pm 0.1)$ μm.

We estimate the expansion of the Rydberg atoms chain analyzing the histogram plot of the ions arrival times. In Fig.6.15 we report the histogram plots of the arrival times distribution taken for two different expansion times 130 μs (light blue) and 1000 μs (dark blue) for a detuning $\Delta/2\pi = 80$ MHz. From the gaussian fit of the distribution we obtain the standard deviation which describes the dispersion of the arrival time around the mean time of flight. We can see that for longer expansion time the distribution of the arrival time becomes broader as we can expect from an expanding cloud. Using the arrival times calibration described by equation 6.9 we can quantify the expansion of the Rydberg cluster along the direction identified by the vector $\mathbf{s} = \alpha\mathbf{x} + \beta\mathbf{z}$ (right axis of Fig. 6.16), which is orthogonal to the isochronous plane identified by

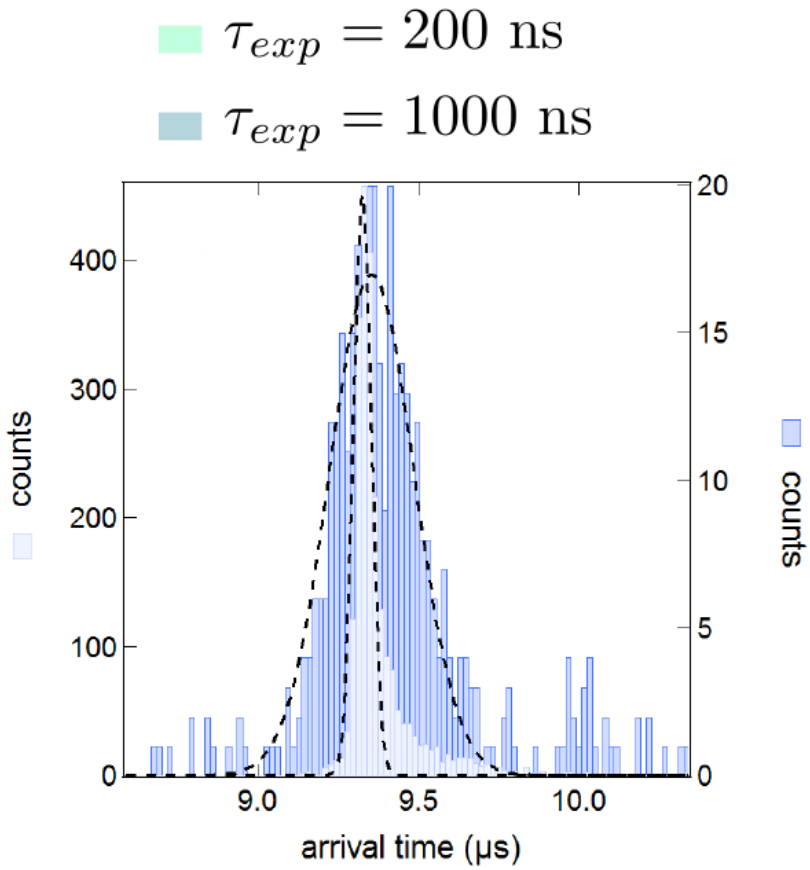

Figure 6.15: Arrival time distributions of ions at the channeltron after excitation for an expansion times equal to 130 μs (light blue) and 1000 μs (dark blue) for detuning $\Delta/2\pi = 80$ MHz. The left axis refers to the former, and the right axis to the latter. The dashed lines correspond to the respective gaussian fit. The standard deviation we obtain from the fit is then converted in a spatial expansion using the calibration of section 6.3.2. The histogram plot are the result of 400 shots.

equation 6.8 (the values of the coefficient α and β are listed in table 6.1).

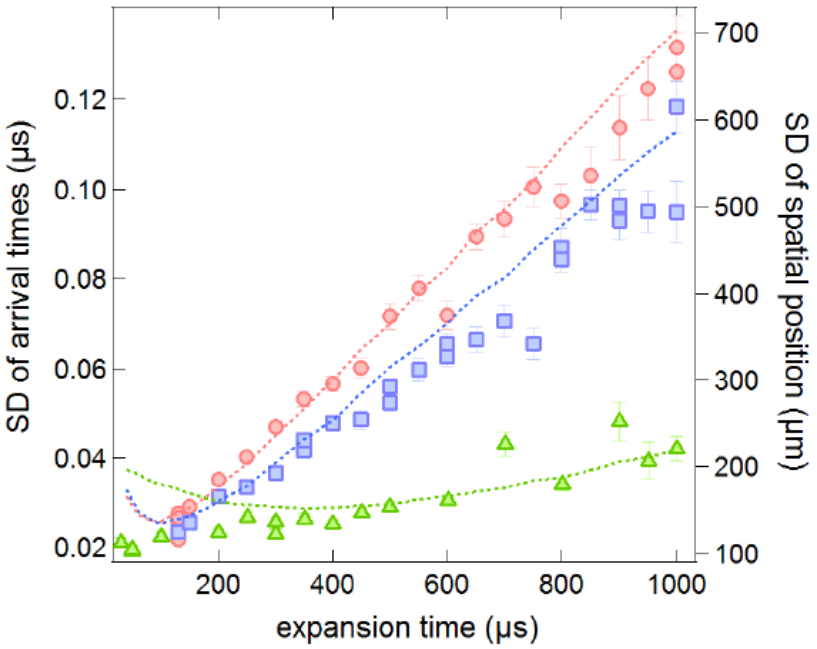

Figure 6.16: Spatial expansion along ***s*** direction is plotted varying the ionization delay. The ionization delay is measured between the end of the Rydberg excitation and the begging of the ionization. Experimental points are reported for on resonant (green diamond) and off-resonant (55 MHz blue square and 80 MHz red circle) Rydberg excitation. The green dotted, blue dashed and red dotted-dashed lines are the respective numerical simulation. The error bars are the standard deviation of the time of flight distribution fitted with a Gaussian curve.

In Fig.6.16 we plot the standard deviation of the arrival times distribution (left axes) for different expansion times ranging between 130 μs and 1000 μs. The red circles correspond to the $\Delta/2\pi = 80$ MHz, the blue squares for $\Delta/2\pi = 55$ MHz and the green triangle to the on resonant excitation. On the right axes we plot the corresponding spatial expansion.

We scan the expansion of the Rydberg cluster for a range of time much larger than the lifetime of the 70 $S_{1/2}$ Rydberg state, which is about 150 μs. For that reason we choose a high enough number of acquisition (400 shots) in order to have a sufficient statistics of the ions arrival time in order to extract a standard deviation of the arrival time distribution. We also assume that the spontaneous decay of the Rydberg excitations occurs independently from each other; in that case the arrival time distribution of the non-decayed subset of atoms reflects the one of the all initially excited atoms.
In Fig.6.16 we also plot the numerical simulation of the expansion of a cluster of Rydberg atoms for the three different experimental condition we have investigated. The numerical simulation, obtained by numerically solving the motion equation [Masella, 2015], takes into account the van der Waals repulsion, the thermal motion of the atoms and the Coulomb repulsion after field ionization, which acts during the $\approx 10\mu$s time-of-flight towards the channeltron. The creation of the clusters is simulated by placing Rydberg atoms at a distance r_{fac} with a probability weighted by the square of the Rabi frequency (since for our experimental parameters the excitation process is incoherent [Lesanovsky and Garrahan, 2013]) that varies perpendicularly to the x-direction. In Fig. 6.17 we report the sketch of a Rydberg chain of 16 atoms. The chain grows along the propagation direction of the blue laser beam. The atoms are randomly distributed along the blue beam but at a fixed distance determined by the equation 6.3. Since in the experimental case we have examined the r_{fac} is comparable to the transversal dimension of the Rydberg excitation the Rydberg aggregates grow in 1 D.

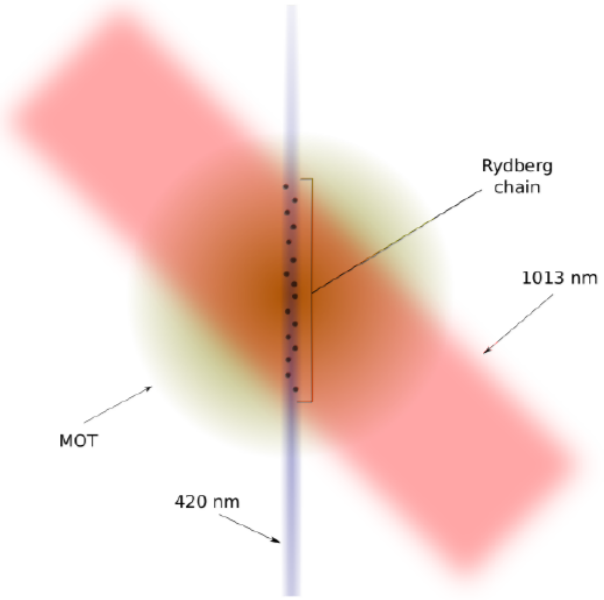

Figure 6.17: Sketch of the excitation of a Rydberg chain. The Rydeberg chain grows along the propagation direction of the blue beam which has a beam waist of 6 μm. We can thus consider a 1 D chain.

In our simulations the nuclear motion is treated classically with an adiabatic evolution of the electronic states and neglecting all the non-adiabatic couplings [Ates et al., 2008]. For long expansion times of the clusters, Fig.6.16 shows excellent agreement between the experiment and the numerical simulation without any adjustable parameters. Below 200 μs the simulation slightly overestimates the effect of the Coulomb explosion. Unfortunately the long excitation pulse (100 μs), necessary to generate the cluster, does not allow to study the expansion for evolution time smaller than 100 μs.
In Fig.6.18-6.19 we plot the calculated velocities of the Rydberg atoms projected respectively along x and z axis for 80 MHz of detuning as a function of the time. As expected from the strong r-dependence, the van der Waals force acts mainly at short interatomic distances and, therefore, the expansion of the cloud is essentially ballistic over the full temporal range as the experimental data and the simulation of Fig.6.16 confirm. In fact, the large initial acceleration, $\approx 5 \times 10^5$ m/s^2 at $\Delta/2\pi = 80$ MHz and r_{fac} , reduces to one percent at 2 r_{fac}. At that detuning the theoretically expected overall increase in velocity for two Rydberg atoms with a corresponding initial vdW energy is $\approx 600\mu$m/ms compared to the average thermal velocity of MOT atoms of $\approx 120\mu$m/ms. After a fast acceleration mostly due to the van der Waals repulsion, the atoms reach a constant velocity in $\approx 10\mu$s; that confirms the ballistic expansion observed. For the on resonance excitation we observe an expansion mostly due to the thermal velocities since the van der Waals interaction is less than 0.5 MHz that is comparable to the laser linewidth of the Rydberg excitation ($\delta_L = 0.7$ MHz).

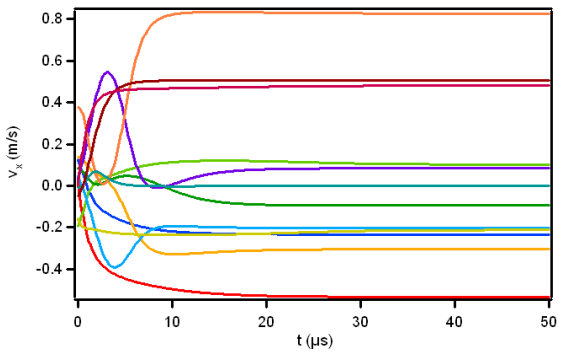

Figure 6.18: Numerical simulation of a van der Waals explosion of a cluster of 12 Rydberg atoms. The projection velocities along the x-axis are plotted as a function of the time for a detuning $\Delta/2\pi = 80$ MHz. Each line corresponds to an atom.

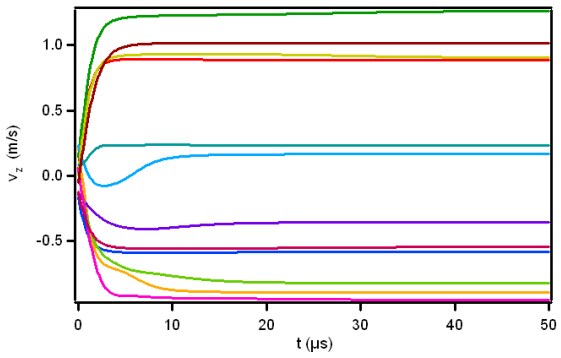

Figure 6.19: Numerical simulation of a van der Waals explosion of a cluster of 12 Rydberg atoms. The projection velocities along the z-axis are plotted as a function of the time for a detuning $\Delta/2\pi = 80$ MHz. Each line corresponds to an atom.

6.4 Conclusion

In this chapter we have observed the mechanical effect of a van der Waals interaction in a 1 D chain of Rydberg atoms. We exploit an off-resonant laser excitation which permits the excitation of Rydberg atoms at a precise distance ≈ 5 μm. At this distance the Rydberg atoms undergo strong van der Waals repulsion. The strength of the van der Waals interaction is directly related to the detuning of the off-resonant excitation. With the calibration of our experimental set up we are able to find a relation between the dispersion of the ions arrival times on the channeltron and the initial position of the ions. This calibration allows us to directly observe with a time-of flight detection the mechanical effect of the van der Waals force. The results we propose differ from the previous measurement of the van der Waals interaction which are mainly focused on the effect of the van der Waals interaction on the internal degrees of freedom [Raimond et al., 1981] as for the case of [Teixeira et al., 2015] where the effect of the van der Waals repulsion between off-resonantly excited Rydebrg atoms is monitored using a microwave spectroscopy. The mechanical effect of the van der Waals interaction has already been observed in [Amthor et al., 2007] and more recently in [Thaicharoen et al., 2015]. However in these two experiments the detuning used for the off-resonant excitation are relatively small. In our set up we investigate large values of the detuning of the Rydberg excitation and consequently larger interactions. The off-resonant excitation scheme is an interesting tool for the excitation of Rydberg aggregates where Rydberg atoms are placed at well defined distance one from the other.

This kind of excitation scheme has been proposed for the implementation of quantum gates [Jaksch et al., 2000] where the control of the distances between the atoms play an essential role. Nevertheless the experimental results we obtained demonstrates the intrinsic mechanical instability of off-resonantly excited Rydberg aggregates. An application of this excitation technique for the implementation of a quantum gate thus require a preliminary study of the stability of a Rydberg cluster. For example a smaller detuning of the off-resonant excitation can attenuate the instability of the cluster.

7 General Conclusion

In the frame of this thesis two different aspects of Rydberg-atom Rydberg-atom interaction have been studied in the two different experimental set-ups I have worked on. In the experiment at Laboratoire Aimé Cotton in Orsay we have investigated the effect on the internal degrees of freedom of Rydberg atoms due to a dipole-dipole interaction. The measure we have done was focused on the detection of a transfer ratio of population from a Rydberg state to another while in the experiment at the Physics Department of Pisa we studied the mechanical effects due to a repulsive van der Waals interaction between Rydberg atoms.

I have spent most of the time of my PhD thesis working on the experiment in Laboratoire Aimé Cotton studying the resonant dipole-dipole interaction in a frozen Rydberg gas. Here I have obtained the main result of my PhD thesis which consists in the observation of two kind of Borromean three-body FRET resonance described by the transfer equations:

$$3 \times p \leftrightarrow s + s' + p'$$
$$3 \times p' \leftrightarrow s + s' + p.$$

The energy transfer scheme for the two processes is resumed in the insets of Fig. 7.1. We have observed these two kinds of resonance in a frozen Rydberg gas of Cs atoms, but in principle these two processes can be observed in any kind of atomic species that present a Förster resonance with an initial state with a total angular momentum $j > 1/2$. This last condition is necessary because the process requires an additional state close to degeneracy with the starting state. We thus require an initial state with at least two Zeeman sub-level. We have observed three-body processes for three different principal quantum numbers ($n = 28, 32, 35$) and in principle we can generalize these processes for every value of n. However in the case of Cs we can only go up to $n = 41$, because for higher principal quantum number no Förster resonance is possible. We observed a transfer ratio up to 28 % for $n = 35$ showing the strong coupling achievable for a three-body resonance compared to the one for a two-body FRET which saturate approximately at 50 %.

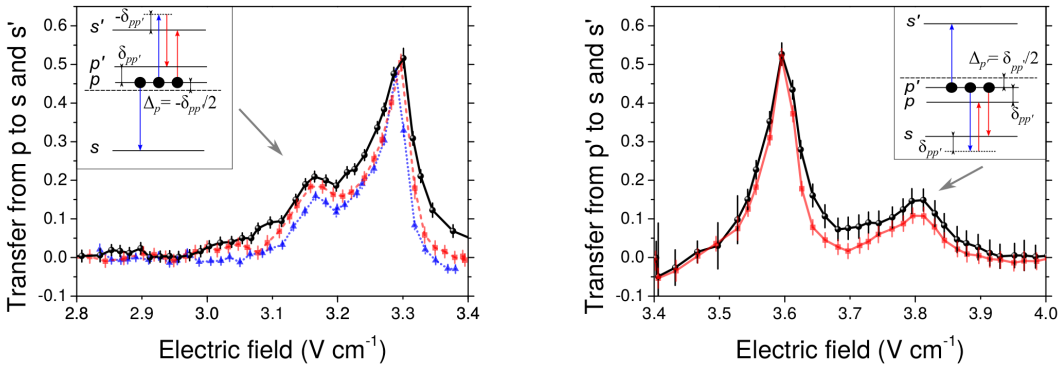

Figure 7.1: Experimental observation of two and three-body FRET for a principal quantum number $n = 35$. The two insets in the figure summarise the energy transfer scheme for the two three-body resonances we have observed.

Borromean three-body FRET can find application in quantum computing. We have proposed three different application: the realization of a full entangled three-body state; the implementation of a heralded entanglement experiment with a μ-wave assisted ionization of the "herald" atom; the exploitation of the three-body interaction for the swap two qu-bits in a Fredkin quantum gate.
The detection of this three-body interaction was possible after the careful analysis of all the transfer peaks we can observe in the proximity of a Förster resonance. These transfer peaks are due to the quasi forbidden resonances. A large number of quasi forbidden resonance has been observed. A transfer ratio up to 30 % has been observed for these resonances revealing a strong dipole-dipole coupling. We have observed the excitation of high orbital angular momentum Rydberg state up to h Rydberg states that are hard to achieve with the common Rydberg excitation techniques. So that quasi forbidden resonances could be of interest in the case of potential processes requiring tunable interactions over a broad band of electric field, like in the search for few-body interactions or to realize macro-molecules built from Rydberg atoms. They could also play a non-negligible role in dipole-quadrupole interaction.

During the six months I have spent in Pisa, I have worked on the experiment with cold Rb Rydberg atoms. We realize a study of the van der Waals expansion of a cluster of Rydberg atoms. The 1D cluster we studied, was realized using an off-resonant Rydberg excitation with a detuning up to 80 MHz. We observe the expansion of the cluster mainly due to the van der Waals repulsion between Rydberg

atoms. For estimate the spatial expansion of the cluster we realize a calibration of the arrival times of the detected ions as a function of the position at which they are excited. The result we obtained demonstrate the intrinsic mechanical instability of the off-resonantly excited Rydberg aggregates, that were first proposed for the implementation of quantum gates. Moreover the detection technique we implement has significant analogies with Coulomb explosion imaging technique largely used in molecular physics.

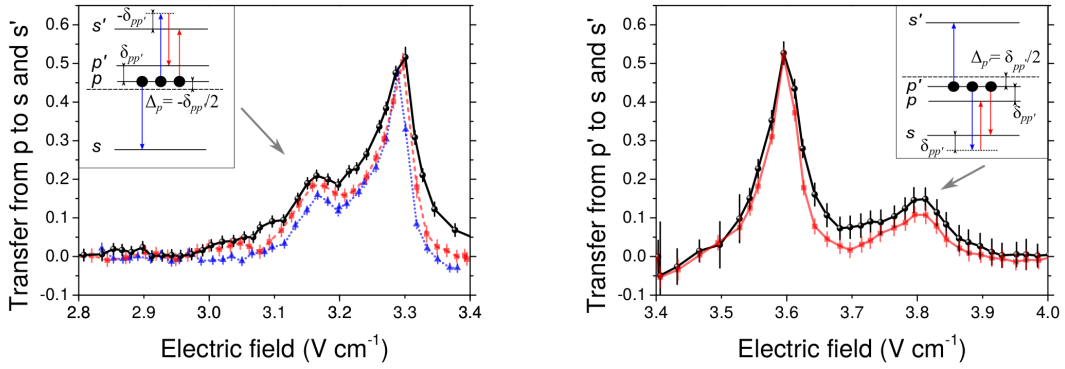

Figure 7.2: Observation expérimentale des FRET à deux et trois-corps pour un nombre quantique principal $n = 35$. Les deux encarts dans la figure (a) et (b) représentent les deux chemins d'interaction pour les deux processus à trois-corps.

L'objectif de cette thèse est l'étude des différents aspects de l'interaction à quelques corps entre des atomes de Rydberg froids. Cette thèse a été réalisée dans le cadre d'une cotutelle entre l'Université Paris-Saclay et l'Université de Pise en travaillant sur deux différents montages expérimentaux sur des atomes de Rydberg froids: respectivement sur le Cs au Laboratoire Aimé Cotton et sur le Rb au département de Physique de l'Universitè de Pise. Au Laboratoire Aimé Cotton nous avons démontré l'existence des nouvelles interactions à trois corps dans un gaz gelé des atomes de Rydberg. Ces nouvelles résonances sont la généralisation des résonances de Förster bien connues dans le domaine des atomes de Rydberg. Elles sont décrites par les équations de transfert suivantes:

$$3 \times p \leftrightarrow s + s' + p' \tag{7.1}$$

$$3 \times p' \leftrightarrow s + s' + p \tag{7.2}$$

où on a utilisé la notation suivante: les états $|ns_{1/2}\rangle$, $|(n+1)s_{1/2}\rangle$, $|np_{3/2}, |m_j| = 1/2\rangle$ et $|np_{3/2}, |m_j| = 3/2\rangle$ du Cs sont indiqués avec s, s', p, et p' respectivement.
Ces résonances agissent sur les degrés de liberté interne des atomes de Rydberg et elles ont l'effet d'un transfert résonant d'énergie et de populations entre les états de

Rydberg comme dans le cas des FRET (Fluorescence Resonance Energy Transfer). En analogies avec la résonance de Förster, les résonances FRET à trois corps sont accordées avec un champ électrique externe et peuvent être observées pour différents nombres quantiques principaux. Les effets à trois corps sont observés en absence de tout effet à deux corps et sont qualifiés de Borroméens.
Dans la figure 7.2 on montre le ratio des atomes qui on été transférés dans un état $s+s'$ à partir de l'état p (a) ou p' (b) (pour un nombre quantique principal $n = 35$) en fonction du champ électrique appliqué. On voit deux pics avec un ratio de transfert égal à 0.5, qui correspondent aux FRET à deux-corps décrites par les équations:

$$2 \times p \leftrightarrow s + s' \tag{7.3}$$

$$2 \times p' \leftrightarrow s + s' \tag{7.4}$$

Les deux pics avec un transfert $\approx\ 0.2 - 0.3$ sont dus aux interactions à trois-corps décrites par les équations 7.1-7.2. Ce taux de transfert est proche de la limite de saturation qui on s'attend vers le 0.33. On estime un couplage pour une interaction à trois-corps de l'ordre du 2-3 MHz qui est comparable avec le couplage dipole-dipole d'une résonance Förster (≈ 15 MHz).
Nous avons observé ces deux types de résonance dans un gaz gelé des atomes de Rydberg de Cs, mais en principe, ces deux processus peuvent être observées pour toutes les espèces atomiques qui présentent une résonance de Förster avec un état initial avec un moment angular total $j > 1/2$. Cette dernière condition est nécessaire parce que le processus exige un état proche de la dégénérescence de l'état de départ. Un état initial avec au moins deux sous-niveau Zeeman est donc nécessaire.

Pour mieux caractériser l'interaction à trois-corps on a étudié la dépendance du transfert en fonction de la densité initial. On a étudié les résonace à deux et trois-corps décrites par les équations 7.2-7.4. Dans la figure 7.3 on montre les nombre des atomes transférés dans un état $s + s'$ en fonction de la densité initial p'. Les points noirs correspondent à la resonance à deux-corps pour un champ électrique égal à 3.60 V cm^{-1}. On voit deux différents régimes: pour des "faibles densité" le nombre des atomes transférés augmente avec une loi quadratique, donc typique d'un processus à deux-corps; pour des "hautes densité" on voit une croissance linéaire liée à la saturation du transfert. Les points gris correspondent à la résonance à trois-corps pour un champ électrique égal à 3.80 V cm^{-1}. On voit une croissance cubique d'atomes typique d'un processus à trois-corps. Ce dernier résultat est une supplémentaire confirmation du fait qu'on assiste à un processus à trois corps.
La présence d'un champ externe, nécessaire pour accorder les résonances à deux et trois-corps, peut générer d'autres résonances entre atomes de Rydberg, qui sont interdites en absence de champ électrique. Quand on applique un champ électrique, le

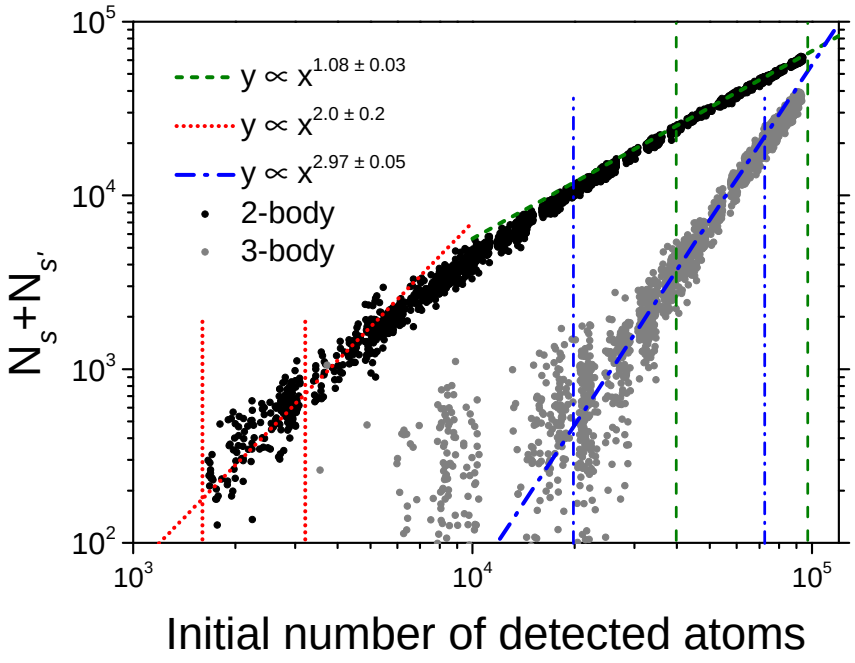

Figure 7.3: Nombre des atomes détectés dans un état s et s' en fonction de la densité initial des atomes dans l'état p' ($n = 35$) pour un champ électrique égal résonant à 3.60 V cm^{-1} pour le deux-corps (points noirs) et 3.80 V cm^{-1} pour le trois-corps (points gris). Dans le cas de résonance à deux corps, pour des faibles densité le fit est compatible avec une loi quadratique (ligne rouge), par contra pour des hautes densité le scaling est linéaire (ligne vert). Dans le cas du trois-corps oú le fit est compatible avec une loi cubique.

nombre quantique orbital l n'est plus un bon nombre quantique; le moment angulaire de l'états de Rydberg n'est pas bien défini. L' état de Rydberg "p" qui on excite peut donc être couplé, avec un couplage dipole-dipole de type Förster, avec des états de Rydberg caractérisés par des nombres quantique orbital au-delà du celui permis par les règles des séléctions. Cet effet peut donner lieu à des résonances, qu'on peut qualifier des résonances quasi-interdites. Nous avons identifié toutes ces résonances liées au couplage entre les multiplicités de différents nombres quantiques principaux. Cette classification a été nécessaire pour pouvoir discerner les pics trois-corps parmi les différents pics de transfert liés aux résonances quasi-interdites.
Les FRET Borroméens à trois-corps peuvent trouver des applications dans la computation quantique pour la mise en œuvre des portes quantique à trois-corps ou pour la réalisation des états intriqués à deux ou trois-corps.

Dans le montage expérimental à Pise on a étudié les effets mécaniques d'une répulsion van der Waals entre atomes de Rydberg. Nous avons étudié l'expansion due à l'interaction van der Waals dans une chaîne 1D des atomes de Rydberg de Rb, qui ont étés excités avec une excitation laser hors résonance. Le fait d'utiliser une excitation laser hors résonance permets d'exciter les atomes de Rydberg à une distance inférieur par rapport au rayon du blocage dipolaire. Dans ces conditions l'interaction van der Waals entre couples des atomes est égal au désaccord de l'excitation laser. On a donc comparé l'expansion d'une chaîne des atomes pour différent déssacords. Dans la figure 7.4 on tracé l'expansion spatial de la chaîne d'atomes (SD of spatial position (μm)) en fonction du delay d'ionisation des atomes de Rydberg. Les donnés experimetaux sont tracé pour 2 différents désaccords: 55 MHz (carrés blues), 80 MHz (cercles rouges) et une excitation résonant (trinagles verts). On voit bien que la taille de la chaîne augmente quand on augmente le delay d'ionisation des atomes de Rydberg et aussi que la répulsion et donc l'expansion est plus grand pour des désaccords plus grands.

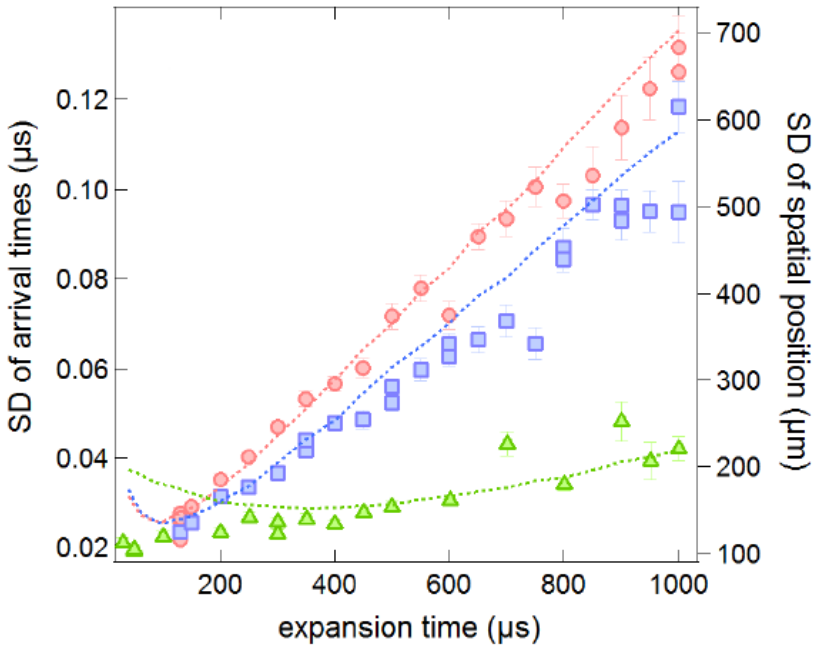

Figure 7.4: Expansion spatiale d'une chaîne 1 D d'environ 12 atomes de Rydberg pour 2 différents désaccords: 55 MHz (carrés blues) et 80 MHz (cercles rouges). L'expansion est tracé en fonction du delay d'ionisation de la chaîne. Les triangles verts sont les points expérimentaux pour une chaîne excitée avec une excitation laser résonant.

Liste des publications:

- R.Faoro, B. Pelle, A. Zuliani, P. Cheinet, E. Arimondo, P. Pillet. Borromean three-body fluorescent resonant energy transfer in frozen Rydberg gases, *Nature Communications*, **6** , 8173, (2015).

- R. Faoro, C. Simonelli, M. Archimi, G. Masella, M. M. Valado, E. Arimondo, R. Mannella, D. Ciampini, O. Morsch. Van der Waals explosion of cold Rydberg clusters, arXiv:1506.0843, (2015). (Soumis à *PRL*)

- B. Pelle, R. Faoro, J. Billy, E. Arimondo, P.Pillet, P. Cheinet. Quasi-forbidden 2-body Förster resonances in cold Cs Rydberg gas, arXiv:151005350, (2015). (Soumis à *PRA*).

Bibliography

[Ajayaghosh et al., 2007] Ajayaghosh, A., Praveen, V., and Vijayakumar, C. (2007). Organogels as scaffolds for excitation energy transfer and light harvesting. *Chem. Soc. Rev.*, 37:109.

[Amthor et al., 2007] Amthor, T., Reetz-Lamour, M., Westermann, S., Denskat, J., and Weidemüller, M. (2007). Mechanical effect of van der Waals interactions observed in real time in an ultracold Rydberg gas. *Phys. Rev. Lett.*, 98:023004.

[Anderson et al., 1998] Anderson, W. R., Veale, J. R., and Gallagher, T. F. (1998). Resonant dipole-dipole energy transfer in a nearly frozen Rydberg gas. *Phys. Rev. Lett.*, 80:249–252.

[Ates et al., 2008] Ates, C., Eisfeld, A., and J., R. (2008). Motion of rydberg atoms induced by resonant dipoledipole interactions. *New J. Phys.*, 10:045030.

[Ates et al., 2006] Ates, C., Pohl, T., Pattard, T., and M., R. J. (2006). Strong interaction effects on the atom counting statistics of ultracold rydberg gases. *Journal of Physics B: Atomic, Molecular and Optical Physics*, 39:L 233.

[Barredo et al., 2015] Barredo, D., Labuhn, H., Ravets, S., Lahaye, T., Browaeys, A., and Adams, C. S. (2015). Coherent excitation transfer in a spin chain of three Rydberg atoms. *Phys. Rev. Lett.*, 114:113002.

[Béguin et al., 2013] Béguin, L., Vernier, A., Chicireanu, R., Lahaye, T., and Browaeys, A. (2013). Direct measurement of the van der Waals interaction between two Rydberg atoms. *Phys. Rev. Lett.*, 110:263201.

[Bernien et al., 2013] Bernien, H., Hensen, B., Pfaff, W., Koolstra, G., Blok, M. S., Robledo, L., Taminiau, T. H., Markham, M., Twitchen, D. J., Childress, L., and Hanson, R. (2013). Heralded entanglement between solid-state qubits separated by three metres. *Nature*, 497:86–90.

[Beterov et al., 2009] Beterov, I. I., Ryabtsev, I. I., Tretyakov, D. B., and Entin, V. M. (2009). Quasiclassical calculations of blackbody-radiation-induced depopulation rates and effective lifetimes of rydberg ns, np, and nd alkali-metal atoms with $n \leq 80$. *Phys. Rev. A*, 79:052504.

[Bethe and Salpeter, 1957] Bethe, H. A. and Salpeter, E. (1957). *Quantum Mechanics of One and Two Electrons Atoms*. Academic Press.

[Bloch et al., 2012] Bloch, I., Dalibard, J., and S., N. (2012). Quantum simulations with ultracold quantum gases. *Nat. Phys.*, 8:267–276.

[Bocharova et al., 2008] Bocharova, I. A., Mashiko, H., Magrakvelidze, M., Ray, D., Ranitovic, P., Cocke, C. L., and Litvinyuk, I. V. (2008). Direct Coulomb-explosion imaging of coherent nuclear dynamics induced by few-cycle laser pulses in light and heavy hydrogen. *Phys. Rev. A*, 77:053407.

[Bourdel et al., 2004] Bourdel, T., Khaykovich, L., Cubizolles, J., Zhang, J., Chevy, F., Teichmann, M., Tarruel, L., Kokkelmans, S. J. J. M. F., and Salomon, C. (2004). Experimental study of the BEC-BCS crossover region in lithium 6. *Phys. Rev. Lett.*, 93:050401.

[Buluta and Nori, 2009] Buluta, I. and Nori, F. (2009). Quantum simulators. *Science*, 326:108–111.

[Casabone et al., 2013] Casabone, B., Stute, A., Friebe, K., Brandstätter, B., Schüppert, K., Blatt, R., and Northup, T. E. (2013). Heralded entanglement of two ions in an optical cavity. *Phys. Rev. Lett.*, 111:100505.

[Castellani and Cavagna, 2005] Castellani, T. and Cavagna, A. (2005). Spin-glass theory for pedestrians. *J. Stat. Mech*, 5012:52.

[Ciampini, 2003] Ciampini, D. (2003). *Realization of a ^{87}Rb Bose-Einstein condensate: Atomic Physics with Coherent Matter Waves.* PhD thesis, Scuola di Dottorato " G. Galilei", Univeritá di Pisa.

[Collini et al., 2010] Collini, E., Wong, C. Y., Wilk, K. E., Curmi, P. M. G., P., B., and Scholes, G. D. (2010). Coherently wired light-harvesting in photosynthetic marine algae at ambient temperature. *Nature*, 463:644–647.

[Comparat and Pillet, 2010] Comparat, D. and Pillet, P. (2010). Dipole blockade in a cold Rydberg atomic sample. *J. Opt. Soc. Am. B*, 27:A208–A232.

[Cooke and Gallagher, 1978] Cooke, W. E. and Gallagher, T. F. (1978). Dependence of Rydberg-state field-ionization thresholds on $|m_l|$. *Phys. Rev. A*, 17:1226–1228.

[Côté et al., 2006] Côté, R., Russell, A., Eyler, E., and Gould, P. (2006). Quantum random walk with Rydberg atoms in an optical lattice. *New Journal of Physics*, 8:156.

[Deiglmayr et al., 2014] Deiglmayr, J., Saßmannshausen, H., Pillet, P., and Merkt, F. (2014). Observation of dipole-quadrupole interaction in an ultracold gas of Rydberg atoms. *Phys. Rev. Lett.*, 113:193001.

[Drake and Swainson, 1991] Drake, G. W. F. and Swainson, R. A. (1991). Quantum defects and the 1/n dependence of Rydberg energies: Second-order polarization effects. *Phys. Rev. A*, 44(9):5448–5458.

[Fano and Rau, 1986] Fano, U. and Rau, A. (1986). *Atomic Collisions and Spectra*. Academic Press.

[Farley et al., 1977] Farley, J., Tsekeris, P., and Gupta, R. (1977). Hyperfine-structure measurements in the rydberg S and P states of rubidium and cesium. *Phys. Rev. A*, 15:1530–1536.

[Feynman and Leighton, 1964] Feynman, R. and Leighton, R. (1964). *The Feynmann Lectures on Physics*, volume 2. AddisonWesley.

[Feynman, 1982] Feynman, R. P. (1982). Simulating physics with computers. *Int. J. Theor. Phys.*, 21:467–488.

[Flannery et al., 2005] Flannery, M. R., Vrinceanu, D., and Ostrovsky, V. N. (2005). Long-range interaction between polar Rydberg atoms. *J. Phys. B: At. Mol. Opt. Phys.*, 38:S279–S293.

[Förster, 1948] Förster, T. (1948). Zwischenmolekulare energiewanderung und fluoreszenz. *Ann. Phys.*, 437:55–75.

[Fredkin and Toffoli, 1982] Fredkin, E. and Toffoli, T. (1982). Conservative logic. *International Journal of Theoretical Physics*, 21:219–253.

[Gaëtan et al., 2009] Gaëtan, A., Miroshnychenko, Y., Wilk, T., Chotia, A., Viteau, M., Comparat, D., Pillet, P., Browaeys, A., and Grangier, P. (2009). Observation of collective excitation of two individual atoms in the Rydberg blockade regime. *Nature*, 5:115–118.

[Gallagher, 1994] Gallagher, T. F. (1994). *Rydberg Atoms*. Cambridge University Press.

[Gallagher and Cooke, 1979] Gallagher, T. F. and Cooke, W. E. (1979). Interactions of blackbody radiation with atoms. *Phys. Rev. Lett.*, 42:835–839.

[Gärttner et al., 2013] Gärttner, M., Heeg, K. P., Gasenzer, T., and Evers, J. (2013). Optimal selfassembly of Rydberg excitations for quantum gate operations. *ArXiv e-prints*.

[Georgescu et al., 2014] Georgescu, I. M., Ashhab, S., and Nori, F. (2014). Quantum simulation. *Rev. Mod. Phys.*, 86:153–185.

[Goy et al., 1982] Goy, P., Raimond, J. M., Vitrant, G., and S., H. (1982). Millimeter-wave spectroscopy in cesium Rydberg states. quantum defects, fine- and hyperfine-structure measurements. *Phys. Rev. A*, 26:2733–2742.

[Greiner et al., 2002] Greiner, M., Mandel, O., Esslinger, T., Hänsch, T., and Bloch, I. (2002). Quantum phase transition from a superfluid to a Mott insulator in a gas of ultracold atoms. *Nature*, 415:39–44.

[Günter et al., 2013] Günter, G., Schempp, H., Robert-de Saint-Vincent, M., Gavryusev, V., Helmirich, S., Hofmann, C. S., Whitlock, S., and Weidemüller, M. (2013). Observing the dynamics of dipole-mediated energy transport by interaction-enhanced imaging. *Science*, 342:954–956.

[Gurian et al., 2012] Gurian, J. H., Cheinet, P., Huillery, P., Fioretti, A., Zhao, J., Gould, P. L., Comparat, D., and Pillet, P. (2012). Observation of a resonant four-body interaction in cold cesium Rydberg atoms. *Phys. Rev. Lett.*, 108:023005.

[Hamamatsu,] Hamamatsu, I. *https://www.hamamatsu.com/*.

[Hogan and Merkt, 2008] Hogan, S. D. and Merkt, F. (2008). Demonstration of three-dimensional electrostatic trapping of state-selected Rydberg atoms. *Phys. Rev. Lett.*, 100:043001.

[Hougen, 1970] Hougen, J. (1970). The calculation of rotational energy levels and rotational line intensities in diatomic molecules. Technical report, National Bureau of Standards, Washington, DC.

[Huillery, 2013] Huillery, P. (2013). *Few and Many-body Physics in cold Rydberg gases*. PhD thesis, EDOM.

[Isenhower et al., 2010] Isenhower, L., Urban, E., Zhang, X. L., Gill, A. T., Henage, T., Johnson, T. A., Walker, T. G., and Saffman, M. (2010). Demonstration of a neutral atom controlled-NOT quantum gate. *Phys. Rev. Lett*, 104:010503.

[Jackson, 1962] Jackson, J. D. (1962). *Classical Electrodynamics*. John Wiley & Sons, Inc.

[Jaksch et al., 2000] Jaksch, D., Cirac, J. I., Zoller, P., Rolston, S. L., Côté, R., and Lukin, M. D. (2000). Fast quantum gates for neutral atoms. *Phys. Rev. Lett.*, 85:2208–2211.

[Jares-Erijman and Jovin, 2003] Jares-Erijman, E. and Jovin, T. (2003). FRET imaging. *Nat. Biotech.*, 21:1387–1395.

[Kachru et al., 1983] Kachru, R., Gallagher, T. F., Gounand, F., Pillet, P., and Tran, N. H. (1983). Resonant collisions of *Na nS* and *nD* Rydberg atoms. *Phys. Rev. A*, 28:2676.

[Kellert et al., 1981] Kellert, F. G., Jeys, T. H., McMillian, G. B., Smith, K. A., Dunning, F. B., and Stebbings, R. F. (1981). Study of Rydberg-atom l-changing collisions using selective field ionization. *Phys. Rev. A*, 23:1127–1133.

[Kiffner et al., 2013] Kiffner, M., Li, W., and Jaksch, D. (2013). Three-body bound states in dipole-dipole interacting Rydberg atoms. *Phys. Rev. Lett.*, 111:233003.

[Kinoshita et al., 2004] Kinoshita, T., Wenger, T., and Weiss, D. S. (2004). Observation of a one-dimensional Tonks-Girardeau gas. *Science*, 305:1125–1128.

[Konishi and Paffuti, 2009] Konishi, K. and Paffuti, G. (2009). *Quantum Mechanichs: A New Introduction*. Clarendon Press.

[Kraemer et al., 2004] Kraemer, T., Herbig, J., Mark, M., Weber, T., Chin, C., Ngerl, H.-C., and Grimm, R. (2004). Optimized production of a cesium Bose-Einstein condensate. *Applied Physics B*, 79:1013–1019.

[Kraemer et al., 2006] Kraemer, T., Mark, M., Waldburger, P., Danzl, J. G., Chin, C., Engeser, B., Lange, A. D., Pilch, K., Jaakkola, A., Nägerl, H.-C., and Grimm, R. (2006). Evidence for Efimov quantum states in an ultracold gas of caesium atoms. *Nature*, 440:315–318.

[Lesanovsky and Garrahan, 2013] Lesanovsky, I. and Garrahan, J. P. (2013). Kinetic constraints, hierarchical relaxation, and onset of glassiness in strongly interacting and dissipative Rydberg gases. *Phys. Rev. Lett.*, 111:215305.

[Lesanovsky and Garrahan, 2014] Lesanovsky, I. and Garrahan, J. P. (2014). Out-of-equilibrium structures in strongly interacting Rydberg gases with dissipation. *Phys. Rev. A*, 90:011603.

[Letokhov, 2007] Letokhov, V. S. (2007). *Laser Control of Atoms and Molecules*. Oxford University Press.

[Li et al., 2003] Li, W., Mourachko, I., Noel, M. W., and Gallagher, T. F. (2003). Millimeter-wave spectroscopy of cold Rb Rydberg atoms in a magneto-optical trap: Quantum defects of the *ns* , *np* , and *nd* series. *Phys. Rev. A*, 67:052502.

[Li et al., 2005] Li, W., Tanner, P. J., and Gallagher, T. F. (2005). Dipole-dipole excitation and ionization in an ultracold gas of Rydberg atoms. *Phys. Rev. Lett.*, 94:173001.

[Littman et al., 1978] Littman, M. G., Kash, M. M., and Kleppner, D. (1978). Field-ionization processes in excited atoms. *Phys. Rev. Lett.*, 41:103–107.

[Luc-Koenig and Bachelier, 1980] Luc-Koenig, E. and Bachelier, A. (1980). Systematic theoretical study of the stark spectrum of atomic hydrogen. ii. density of oscillator strengths. comparison with experimental absorption spectra in solid-state and atomic physics. *Journal of Physics B: Atomic and Molecular Physics*, 13(9):1769.

[Mack et al., 2011] Mack, M., Karlewski, F., Hattermann, H., Höckh, S., Jessen, F., Cano, D., and Fortágh, J. (2011). Measurement of absolute transition frequencies of ^{87}Rb to *nS* and *nD* rydberg states by means of electromagnetically induced transparency. *Phys. Rev. A*, 83:052515.

[Malossi et al., 2014] Malossi, N., Valado, M. M., Scotto, S., Huillery, P., Pillet, P., Ciampini, D., Arimondo, E., and Morsch, O. (2014). Full counting statistics and phase diagram of a dissipative Rydberg gas. *Phys. Rev. Lett.*, 113:023006.

[Mandel, 1979] Mandel, L. (1979). Sub-poissonian photon statistics in resonance fluorescence. *Optics Letters*, 4.

[Masella, 2015] Masella, G. (2015). Many-body physics of strongly interacting Rydberg atoms. Master's thesis, Università di Pisa - Dipartimento di Fisica.

[Messiah, 1961a] Messiah, A. (1961a). *Quantum Mechanics, Volume I*. North-Holland Publishing Company.

[Messiah, 1961b] Messiah, A. (1961b). *Quantum Mechanics, Volume II*. North-Holland Publishing Company.

[Metcalf and van der Straten, 1999] Metcalf, H. J. and van der Straten, P. (1999). *Laser Cooling and Trapping*. Springer.

[Monroe, 2002] Monroe, C. (2002). Quantum information processing with atoms and photons. *Nature*, 416:238–246.

[Mourachko et al., 1998] Mourachko, I., Comparat, D., de Tomasi, F., Fioretti, A., Nosbaum, P., Akulin, V. M., and Pillet, P. (1998). Many-body effects in a frozen Rydberg gas. *Phys. Rev. Lett.*, 80:253–256.

[Mourachko et al., 2004] Mourachko, I., Li, W., and Gallagher, T. F. (2004). Controlled many-body interactions in a frozen Rydberg gas. *Phys. Rev. A*, 70:031401.

[Mülken et al., 2007] Mülken, O., Blumen, A., Amthor, T., Giese, C., Reetz-Lamour, M., and Weidemüller, M. (2007). Survival probabilities in coherent exciton transfer with trapping. *Phys. Rev. Lett.*, 99:090601.

[Numerov, 1924] Numerov, B. (1924). A method of extrapolation of perturbations. *MNRAS*, 84:592.

[Oar et al., 2006] Oar, M. A., Dichtel, W. R., Serin, J. M., Frèchet, J. M. J., Rogers, J. E., Slagle, J. E., Fleitz, P. A., Loon-Seng, T., Ohulchanskyy, T. Y., and Prasad, P. N. (2006). Light-harvesting chromophores with metalated porphyrin cores for tuned photosensitization of singlet oxygen via two-photon excited FRET. *Chem. Mater.*, 18:3682–3692.

[Paredes et al., 2004] Paredes, B., Widera, A., Murg, V., Mandel, O., Fölling, S., Cirac, I., Shlyapnikov, G. V., Hänsch, T., and Bloch, I. (2004). Tonks-Girardeau gas of ultracold atoms in an optical lattice. *Nature*, 429:277–281.

[Perrin, 1932] Perrin, F. (1932). Théorie quantique des transferts d'activation entre molécules de même espéce. cas des solutions fluorescentes. *Ann. Phys.*, 17:283.

[Pitzer et al., 2013] Pitzer, M., Kunitski, M., Jonhson, A. S., Jahnke, T., H., S., Sturm, F., Schmidt, L. P. H., Schmidt-Böcking, H., Dörner, R., Stohner, J.,

Kiedrowski, J., Reggelin, M., Marquardt, S., Schießer, S., Berger, R., and Schöffler, M. S. (2013). Direct determination of absolute molecular stereochemistry in gas phase by Coulomb explosion imaging. *Science*, 341:1096.

[Pohl et al., 2010] Pohl, R., Antognini, A., Nez, F., Amaro, F. D., Biraben, F., Cardoso, J. M. R., and et al. (2010). The size of proton. *Nature*, 466:7303.

[Pollack et al., 2009] Pollack, S. E., Dries, D., and Hulet, R. G. (2009). Universality in three-and four-body bound states of ultracold atoms. *Scince*, 326:1683–1685.

[Preston, 1996] Preston, D. W. (1996). Doppler-free saturated absorption: Laser spectroscopy. *Am. J. of Phys.*, 64:1432–1436.

[Radogostowicz, 2010] Radogostowicz, J. (2010). *Investigation of dipole blockade in ultracold atomic ensembles.* PhD thesis, Scuola di Dottorato " G. Galilei", Univeritá di Pisa.

[Raimond et al., 1981] Raimond, J. M., Vitrant, G., and Haroche, S. (1981). Spectral line broadening due to the interaction between very excited atoms: 'the dense Rydberg gas'. *J.Phys. B: At. Mol. Phys.*, 14:L655.

[Ravets et al., 2014] Ravets, S., Labuhn, H., Barredo, D., Béguin, L., Lahaye, T., and Browaeys, A. (2014). Coherent dipole-dipole coupling between two single Rydberg atoms at an electrically-tuned Förster resonance. *Nat. Phys.*, 10:914917.

[Renn et al., 1994] Renn, M. J., Anderson, W. R., and Gallagher, T. F. (1994). Resonant collisions of K Rydberg atoms. *Phys. Rev. A*, 58:1324.

[Rizzo et al., 2004] Rizzo, M., Springer, G., Granada, B., and Piston, D. (2004). An improved cyan fluorescent protein variant useful for FRET. *Nat. Biotech.*, 22:445.

[Ryabtsev et al., 2010] Ryabtsev, I. I., Tretyakov, D. B., Beterov, I. I., and Entin, V. M. (2010). Observation of the Stark-Tuned Förster resonance between two Rydberg atoms. *Phys. Rev. Lett.*, 104:073003.

[Saffman et al., 2010] Saffman, M., Walker, T. G., and Mölmer, K. (2010). Quantum information with Rydberg atoms. *Rev. Mod. Phys.*, 82:2313–2363.

[Safinya et al., 1981] Safinya, K. A., Delpech, J. F., Gounand, F., Sandner, W., and Gallagher, T. F. (1981). Resonant Rydberg-atom-Rydberg-atom collisions. *Phys. Rev. Lett.*, 47:405–408.

[Saßmannshausen et al., 2013] Saßmannshausen, H., Merkt, F., and Deiglmayr, J. (2013). High-resolution spectroscopy of Rydberg states in an ultracold Cesium gas. *Phys. Rev. A*, 87:032519.

[Schauß et al., 2015] Schauß, P., Zeiher, J., Fukuhara, T., Hild, S., Cheneau, M., Macrí, T., Pohl, T., Bloch, I., and Gross, C. (2015). Crystallization in Ising quantum magnets. *Science*, 347:1455–1458.

[Schempp et al., 2014] Schempp, H., Günter, G., Robert-de Saint-Vincent, M., Hofmann, C. S., Breyel, D., Komnik, A., Schönleber, D. W., Gärttner, M., Evers, J., Whitlock, S., and Weidemüller, M. (2014). Full counting statistics of laser excited Rydberg aggregates in a one-dimensional geometry. *Phys. Rev. Lett.*, 112:013002.

[Scholes, 2003] Scholes, G. D. (2003). Long-range resonance energy transfer in molecular systems. *Annu. Rev. Phys. Chem.*, 54:57–87.

[Schwettmann et al., 2006] Schwettmann, A., Crawford, J., Overstreet, K. R., and Shaffer, J. P. (2006). Cold Cs Rydberg-gas interactions. *Phys. Rev. A*, 74:020701.

[Shore, 1990] Shore, B. W. (1990). *The Theory of Coherent Atomic Excitation*. New York: Wiley.

[Stanojevic et al., 2008] Stanojevic, J., Côté, R., Tong, D., Eyler, E. E., and Gould, P. L. (2008). Long-range potentials and $(n-1)d+ns$ molecular resonances in an ultracold Rydberg gas. *Phys. Rev. A*, 78:052709.

[Steck, 2003] Steck, D. A. (2003). Cesium D line data. *http://steck.us/alkalidata.*

[Teixeira et al., 2015] Teixeira, R. C., Hermann-Avigliano, C., Nguyen, T. L., Cantat-Moltrecht, T., Raimond, J. M., Haroche, S., Gleyzes, S., and Brune, M. (2015). Microwaves probe dipole blockade and van der Waals forces in a cold Rydberg gas. *Phys. Rev. Lett.*, 115:013001.

[Thaicharoen et al., 2015] Thaicharoen, N., Schwarzkopf, A., and Raithel, G. (2015). Measurement of van-der-Waals interaction by atom trajectory imaging. *arXiv:1506.02705.*

[Tokihiro et al., 1995] Tokihiro, T., Manabe, Y., and Hanamura, E. (1995). Superradiance of Frenkel excitons with any degree of excitation prepared by a short-pulse laser. *Phys. Rev. B*, 51:7655–7668.

[Torosov and Vitanov, 2012] Torosov, B. T. and Vitanov, N. V. (2012). Adiabatic elimination of a nearly resonant quantum state. *Journal of Physics B: Atomic, Molecular and Optical Physics*, 45:135502.

[Urban et al., 2009] Urban, E. Johnson, T. A., Henage, T., Isenhower, L., Yavuz, D. D., Walker, T. G., and Saffman, M. (2009). Observation of Rydberg blockade between two atoms. *Nat; Phys.*, 5:110–114.

[Vager et al., 1989] Vager, Z., Naaman, R., and Kanter, E. P. (1989). Coulomb explosion imaging of small molecules. *Science*, 244:426.

[Valado, 2015] Valado, M. M. (2015). *Exploring strongly correlated Rydberg excitations in cold gases using full counting statistics*. PhD thesis, Scuola di Dottorato " G. Galilei", Univeritá di Pisa.

[Valado et al., 2013] Valado, M. M., Malossi, N., Scotto, S., Ciampini, D., Arimondo, E., and Morsch, O. (2013). Rydberg tomography of an ultra-cold atomic cloud. *Phys. Rev. A*, 88:045401.

[van Ditzhuijzen, 2009] van Ditzhuijzen, C. S. E. (2009). *Dipole - dipole interaction between cold Rydberg atoms*. PhD thesis, van der Waals-Zeeman Institute.

[Varshalovich et al., 1988] Varshalovich, D. A., Moskalev, A. N., and Khersonskii, V. K. (1988). *Quantum Theory of Angular Momentum*. World Scientific Publishing Co.

[Viteau, 2008] Viteau, M. (2008). *Pompage optique et refroidissement laser de la vibration de molécules froides*. PhD thesis, EDOM.

[Viteau et al., 2008] Viteau, M., Chotia, A., Comparat, D., Tate, D. A., Gallagher, T. F., and Pillet, P. (2008). Melting a frozen Rydberg gas with an attractive potential. *Phys. Rev. A*, 78:040704.

[Viteau et al., 2010] Viteau, M., Radogostowicz, J., Chotia, A., Bason, M. G., Malossi, N., Fuso, F., Ciampini, D., Morsch, O., Ryabtsev, I. I., and Arimondo, E. (2010). Ion detection in the photoionization of a Rb Bose Einstein condensate. *J. Phys. B: At. Mol. Opt. Phys.*, 43:155301.

[Vogt, 2006] Vogt, T. (2006). *Blocage dipolaire de l' excitation d' atomes froids vers des états de Rydberg: Contrôle par champ électrique et résonance de Förster*. PhD thesis, EDOM.

[Vogt et al., 2006] Vogt, T., Viteau, M., Zhao, J., Chotia, A., Comparat, D., and Pillet, P. (2006). Dipole blockade at Förster resonances in high resolution laser excitation of Rydberg states of Cesium atoms. *Phys. Rev. Lett.*, 97:083003.

[Walker and Saffman, 2005] Walker, T. G. and Saffman, M. (2005). Zeros of Rydberg Rydberg Föster interactions. *Journal of Physics B Atomic Molecular Physics*, 38:309.

[Walker and Saffman, 2008] Walker, T. G. and Saffman, M. (2008). Consequences of Zeeman degeneracy for the van der Waals blockade between Rydberg atoms. *Phys. Rev. A*, 77:032723.

[Weber and Sansonetti, 1987] Weber, K. H. and Sansonetti, C. J. (1987). Accurate energies of nS , nP , nD , nF , and nG levels of neutral cesium. *Phys. Rev. A*, 35:4650–4660.

[Weimer et al., 2010] Weimer, H., Müller, M., lesanovsky, I., Zoller, P., and Büchler, H. P. (2010). A Rydberg quantum simulator. *Nat. Phys.*, 6:382–388.

[Weiss, 1999] Weiss, S. (1999). Fluorescence spectroscopy of single biomolecules. *Scienec*, 283:1676.

[Wilk et al., 2010] Wilk, T., Gaëtan, A., Evellin, C., Wolters, J., Miroshnychenko, Y., Grangier, P., and Browaeys, A. (2010). Entanglement of two individual neutral atoms using rydberg blockade. *Phys. Rev. Lett.*, 104:010502.

[Yamashita et al., 2010] Yamashita, M. T., Fedorov, D. V., and Jensen, A. S. (2010). Universality of Brunnian (N-body borromean) four- and five-body systems. *Phys. Rev. A*, 81:063607.

[Zimmerman et al., 1979] Zimmerman, M. L., Littman, M. G., Kash, M. M., and Kleppner, D. (1979). Stark structure of the Rydberg states of alkali-metal atoms. *Phys. Rev. A*, 20:2251–2275.